UNIVERSITAT DE BARCELONA

Nucleation and cavitation in liquid helium

Montserrat Guilleumas Morell

ADVERTIMENT. La consulta d’aquesta tesi queda condicionada a l’acceptació de les següents condicions d'ús: La difusió d’aquesta tesi per mitjà del servei TDX (**www.tdx.cat**) i a través del Dipòsit Digital de la UB (**diposit.ub.edu**) ha estat autoritzada pels titulars dels drets de propietat intel·lectual únicament per a usos privats emmarcats en activitats d’investigació i docència. No s’autoritza la seva reproducció amb finalitats de lucre ni la seva difusió i posada a disposició des d’un lloc aliè al servei TDX ni al Dipòsit Digital de la UB. No s’autoritza la presentació del seu contingut en una finestra o marc aliè a TDX o al Dipòsit Digital de la UB (framing). Aquesta reserva de drets afecta tant al resum de presentació de la tesi com als seus continguts. En la utilització o cita de parts de la tesi és obligat indicar el nom de la persona autora.

ADVERTENCIA. La consulta de esta tesis queda condicionada a la aceptación de las siguientes condiciones de uso: La difusión de esta tesis por medio del servicio TDR (**www.tdx.cat**) y a través del Repositorio Digital de la UB (**diposit.ub.edu**) ha sido autorizada por los titulares de los derechos de propiedad intelectual únicamente para usos privados enmarcados en actividades de investigación y docencia. No se autoriza su reproducción con finalidades de lucro ni su difusión y puesta a disposición desde un sitio ajeno al servicio TDR o al Repositorio Digital de la UB. No se autoriza la presentación de su contenido en una ventana o marco ajeno a TDR o al Repositorio Digital de la UB (framing). Esta reserva de derechos afecta tanto al resumen de presentación de la tesis como a sus contenidos. En la utilización o cita de partes de la tesis es obligado indicar el nombre de la persona autora.

WARNING. On having consulted this thesis you’re accepting the following use conditions: Spreading this thesis by the TDX (**www.tdx.cat**) service and by the UB Digital Repository (**diposit.ub.edu**) has been authorized by the titular of the intellectual property rights only for private uses placed in investigation and teaching activities. Reproduction with lucrative aims is not authorized nor its spreading and availability from a site foreign to the TDX service or to the UB Digital Repository. Introducing its content in a window or frame foreign to the TDX service or to the UB Digital Repository is not authorized (framing). Those rights affect to the presentation summary of the thesis as well as to its contents. In the using or citation of parts of the thesis it’s obliged to indicate the name of the author.

Nucleation and Cavitation in Liquid Helium

Montserrat Guilleumas Morell

DEPARTAMENT D'ESTRUCTURA I CONSTITUENTS DE LA MATÈRIA
UNIVERSITAT DE BARCELONA

Juny de 1995

Nucleation and Cavitation in Liquid Helium

Nucleació i Cavitació en Heli Líquid

Memòria de la Tesi presentada
per na Montserrat Guilleumas Morell
per a optar al grau de
Doctor en Ciències Físiques

DEPARTAMENT D'ESTRUCTURA I CONSTITUENTS DE LA MATÈRIA
UNIVERSITAT DE BARCELONA
Juny de 1995

Manuel Barranco Gómez, Catedràtic d'Universitat de Física Atòmica, Molecular i Nuclear de la Universitat de Barcelona

i

Martí Pi Pericay, Professor Titular d'Universitat de Física Atòmica, Molecular i Nuclear de la Universitat de Barcelona

Certifiquen: que la present memòria titulada "Nucleation and cavitation in liquid helium" presentada per na Montserrat Guilleumas i Morell, ha estat realitzada sota la nostra direcció, en el Departament d'Estructura i Constituents de la Matèria de la Facultat de Física de la Universitat de Barcelona i constitueix la seva tesi per a optar al grau de Doctor en Física.

Barcelona, 26 de juny de 1995

Manuel Barranco

Martí Pi

Als meus pares.
A tota la familia.
I molt especialment a tu, Quim.

Agraïments

Vull agrair a Manuel Barranco i a Martí Pi l'haver-me introduït en el món de la recerca i la seva direcció durant aquests quatre anys de treball, que ha fet possible aquesta tesi. Vull reconèixer també la seva cordialitat, que ha fet moltes vegades més planera tota la feina.

A Dora Jezek li agraeixo la seva contribució que ha estat essencial i de gran ajuda per configurar aquesta tesi, així com les moltes discussions que m'han servit per clarificar o defensar idees. També vull reconèixer l'amistat i les bones estones compartides.

A Jesús Navarro li agraeixo la col.laboració en diferents etapes d'aquest treball.

A Francesca Garcias la col.laboració en altres treballs tot i que no han quedat recollits en aquesta tesi i la seva acollida durant una estada a Palma.

A Franco Dalfovo i Sandro Stringari per la seva franca hospitalitat durant les meves estades a Trento, les moltes discussions i l'haver-me introduït en un tema tan fascinant per mi, fins aleshores desconegut.

Als companys i amics del departament i més concretament de l'àrea, Assum, Ferran i Jordi, per contribuir a crear un ambient agradable de treball i col.laboració.

Contents

Resum

L'heli amb els seus dos isòtops (^{3}He i ^{4}He) són els únics líquids quàntics *reals* que es troben a la natura. Presenten una sèrie de propietats molt peculiars que tenen a veure amb els fonaments de la Mecànica Quàntica i amb implicacions importants en l'estudi d'altres sistemes quàntics de fermions i bosons. És per aquest motiu que l'heli líquid ha esdevingut, ja des de fa temps, un camp de recerca molt actiu.

De totes les substàncies conegudes, els dos isòtops d'heli són les que tenen els punts d'ebullició més baixos, 4.21 K per l'^{4}He i 3.19 K per l'^{3}He. Quan la temperatura es redueix més, estant sota la pressió de saturació de vapor, ambdós esdevenen líquids. En absència de pressió aplicada romanen líquids fins al zero de temperatura. L'heli es pot preparar lliure d'impureses gràcies a que en el rang de temperatures en el qual està en estat líquid totes les substàncies són sòlides i que és superfluid a temperatures inferiors a 2.17 K per ^{4}He i 3 mK per ^{3}He. Així, es poden eliminar pràcticament totes les impureses sòlides per filtració.

Les transicions de fase que tenen lloc en condicions d'equilibri, dins del règim de coexistència, com per exemple el punt d'ebullició d'un líquid o el punt de solidificació, estan ben determinades experimentalment. Ara bé, no totes les transicions de fase esdevenen sota condicions d'equilibri. A mesura que la nova fase estable es va formant l'energia lliure del sistema va disminuint. A prop del punt de transició d'equilibri on la fase original i la que s'està formant coexisteixen, la fase inicial es pot mantenir en

un estat metastable: líquids sobre-escalfats o vapors sobre-refredats són exemples de sistemes metastables. Malgrat ser internament estables, existeix en cada cas una altra configuració que té un potencial termodinàmic menor (vapor en front del líquid sobre-escalfat, líquid en front del vapor sobre-refredat) i per tant el sistema tendirà a aquesta nova configuració energèticament més favorable. La transició, però, no és espontània. Això és degut a l'existència d'una barrera termodinàmica que separa l'estat metastable de l'estable i que per tant bloqueja la formació de la nova fase. Aquesta barrera pot ser superada gràcies a fluctuacions estadístiques en la densitat o en la concentració que tenen com a resultat la formació i creixement de petits nuclis (*clusters*) de la nova fase estable en l'estat metaestable: bombolles en el líquid (cavitació), gotes en el vapor (nucleació).

Per tant, la nucleació és l'inici d'una transformació de fase, com vaporització, liqüefacció o fins i tot solidificació, a partir d'un nucli de la nova fase. La nucleació serà homogènia o heterogènia, segons que el nucli sigui consituït o no per àtoms de la mateixa fase a transformar. El fenòmen de la nucleació juga potencialment un paper en totes les transicions de fase de primer ordre. Pot ser portada a terme per activació tèrmica superant l'alçada de la barrera, o a molt baixes temperatures creuant la barrera per efectes quàntics (*quantum tunneling*). Depenent de com sigui la barrera energètica, el ritme de nucleació serà lent o molt ràpid. Quan el ritme és lent caldrà allunyar-se força de la situació d'equilibri abans no aparegui el primer nucli localitzat. Tan bon punt el sistema és conduit a un estat metastable, el procés de nucleació s'activa: es comencen a formar nuclis de la nova fase estable, si són més petits que un ser tamany que anomenem nucli crític llavors són absorbits pel mateix sistema, ara bé si les fluctuacions generen un nucli amb un tamany superior llavors aquest creixerà desencadenant la separació de fases: el nucli crític és la llavor de la transició de fase.

L'heli líquid és, doncs, un bon banc de prova per estudiar els fenòmens de cavitació homogènia tant per efectes tèrmics com pels quàntics ja que, com hem comentat anteriorment, pot ser preparat lliure d'impureses i a més, a temperatures properes al zero absolut roman en l'estat líquid.

En la teoria clàssica de nucleació es treballa amb l'aproximació de capil.laritat on es suposa que el nucli té una superfície abrupta. Aquesta aproximació macroscòpica presenta una sèrie d'inconvenients. Primer, es negligeix qualsevol efecte de compressió de la densitat central del nucli degut a la seva superfície, com per exemple la variació de l'energia deguda a les correccions de curvatura. I segon, la impossibilitat del model de tenir en compte la modificació de l'energia de superfície del nucli deguda a la presència de vapor quan la temperatura creix. Aquestes limitacions, que són importants en nuclis petits, poden ser superades utilitzant un funcional de la densitat d'energia per calcular les propietats termodinàmiques del sistema, i aquest constitueix precisament el nostre punt de partida.

L'aplicació de l'aproximació del funcional de la densitat al problema de la nucleació es pot resumir en els següents passos. Primer, partint d'un funcional que descrigui correctament el nostre sistema, és convenient considerar el diagrama de fases del sistema i així, d'aquesta manera, delimitar les zones metastables on es formaran els nuclis de la nova fase estable. Llavors:

i. Es determina el perfil de densitat del nucli crític donades unes condicions de pressió i temperatura en les quals el sistema homogeni és metaestable. Cal remarcar que no s'imposen cap mena de restriccions sobre el perfil del nucli, sinó que aquest s'obté resolent una equació d'Euler-Lagrange amb simetria esfèrica amb les condicions de contorn donades pel sistema metaestable.

ii. Un cop ja tenim el perfil del nucli crític, determinem l'alçada de la seva barrera de nucleació, és a dir l'energia necessària per formar-lo en aquelles condicions de metaestabilitat. Aquesta energia s'obté fent la diferència entre el gran potencial del nucli crític i el del sistema homogeni metaestable, tots dos expressats en termes del funcional d'energia lliure.

iii. Per estudiar la nucleació deguda a l'activació tèrmica es procedeix de la següent manera: donada una temperatura, es calcula la pressió de cavitació homogènia que és aquella a la qual el nombre de nuclis crítics formats per unitat de temps i de volum és igual a un cert nombre (normalment un nucli per segon i centímetre cúbic) que indica el començament de la separació de fases.

iv. Mentre que per l'activació tèrmica només cal conèixer l'alçada de la barrera, per estudiar la cavitació quàntica s'ha de conèixer també la seva amplada. Nosaltres hem modelat el creixement del nucli en el medi metastable desplaçant el perfil de densitat de la gota crítica suposant-lo, per tant, invariant. Així, per cada configuració corresponent a una etapa de creixement del nucli, es calcula, anàlogament a l'apartat ii., l'energia necessària per formar-la. D'aquesta manera coneixent ja la barrera energètica en funció de la variable col.lectiva del desplaçament, hem calculat l'acció i a partir d'ella, el ritme de nucleació quàntic i la pressió homogènia de cavitació.

v. La temperatura de transició entre el règim tèrmic i el quàntic és aquella on competeixen els dos efectes, i per tant s'obté igualant els dos ritmes de nucleació.

En aquesta tesi presentem un estudi detallat dels processos de nucleació i cavitació en ^{4}He pur, ^{3}He pur i en mescles de ^{3}He-^{4}He. Hem utilitzat per cada sistema un funcional de l'energia, els paràmetres del qual han estat ajustats per tal de reproduir els resultats experimentals. La flexibilitat del funcional de l'energia és especialment indicada per les mescles d'heli a baixes temperatures on la màxima solubilitat i l'existència dels estats d'Andreev fa difícil de simular els perfils del nucli crític amb qualsevol model de superfície abrupta.

En el capítol 2 hem estudiat nucleació i cavitació per activació tèrmica en ^{4}He i ^{3}He purs. A pressions positives hem vist que la teoria de nucleació homogènia és capaç de reproduir els resultats experimentals. A pressions negatives la situació encara no està ben determinada: els càlculs teòrics presenten una clara discrepància amb els resultats experimentals de l'^{4}He. Experiments recents semblen apuntar, però, que aquesta discrepància pot ser deguda a la molta dificultat i a la poca fiabilitat de les determinacions de pressió i temperatura en la mostra, o a d'altres efectes que no s'hagin tingut en compte com pot ser la nucleació en vòrtexs.

En el capítol 3 hem estudiat la nucleació i cavitació tèrmiques en mescles de ^{3}He-^{4}He. Hem vist que la pressió homogènia de nucleació varia considerablement fins i tot per petites concentracions d'^{3}He. A mesura que s'augmenta la concentració, la tensió superficial disminueix degut a l'existència dels estats superficials d'Andreev i per tant la cavitació esdevé més probable. Hem vist a la secció 3.6 que una manera d'explicar la supersaturació crítica de les mescles d'^{3}He-^{4}He, per sobre de la qual es trenca la mescla, és considerar la desestabilització de línies de vòrtexs d'^{4}He plenes d'^{3}He.

En el capítol 4 hem estudiat la nucleació quàntica en ^{3}He i ^{4}He purs. Hem vist que el funcional de la densitat proporciona un bon marc per estudiar el *quantum tunneling*, en el qual la temperatura de transició entre el règim quàntic i tèrmic pot ser calculada a partir d'una expressió senzilla.

Chapter 1

Introduction

^{3}He and ^{4}He are the only *real* quantum liquids found in nature. Many peculiar properties of those systems have to do with the foundation of Quantum Mechanics and have also significant implications in the study of other quantum systems of fermions and bosons. For this reason liquid helium has become, since a long time, a quite active field of research.

The two isotopes of helium have the lowest normal boiling points of all known substances, 4.21 K for ^{4}He and 3.19 K for ^{3}He. When the temperature is reduced further, both ^{3}He and ^{4}He become liquid under the saturated vapor pressure and in the absence of applied pressure they remain liquid down to absolute zero. The low mass of the atoms, which ensures a high value of zero-point energy, as well as the extremely weak forces between them cause the system to stay liquid even at zero temperature. Helium can be prepared free of impurities, this is because at the temperature range in which helium is in a liquid state all substances become solid. Then, taking advantage of the superfluidity of liquid helium, at temperatures T below 2.17 K for ^{4}He and 3 mK for ^{3}He, one can remove practically all solid impurities by filtration using the ability of superfluids to penetrate the smallest pores.

Low temperature physics has been a rapidly evolving experimental field which has benefit from the special properties of ^{3}He and ^{4}He to construct sophisticated cryogenic apparatus suited to lower the experimental temperatures down to the mK regime. This has allowed experimentalists to study liquid helium at low temperatures discovering a large number of phenomena whereas an underlying theory is still lacking for many of them.

The main difficulty for a theoretical study arises from the fact that liquid helium is a highly correlated many-body system. There are different theoretical methods to study liquid helium. Basically, they can be classified into two types, namely microscopical and phenomenological methods.

Microscopical methods are based on ab initio theories where the system is only characterized by its atomic mass, statistics and interaction potential. It is worth noting that there are relatively simple analytical expressions for the interatomic potential [1, 2] which describe with great accuracy helium interaction. With these basic ingredients one can construct the many-body hamiltonian of the system and then try to solve the corresponding Schrödinger equation.

There are microscopical methods that try to solve "exactly" the Schrödinger equation but with a finite number of particles, for example *Green Function Monte Carlo* and *Diffusion Monte Carlo* methods. Other microscopical approaches solve the Schrödinger equation approximately: there are variational methods (*Hypernetted-chain*, *Variational Monte Carlo*), and perturbative methods which start not from the uncorrelated system but from a basis constructed variationally that already incorporates some correlations (*Correlated Basis Function*).

Phenomenological methods are based mainly on the Density Functional Theory, which has received a renewed interest in their application to quantum liquids. It has been extensively employed in a variety of problems because it provides a rather flexible theoretical basis which is well suited to study different systems (surfaces, thin films, droplets, impurities, vortices,...).

The Density Functional Theory (DFT) is based on the Hohenberg-Kohn theorem [3]. It establishes that the particle density $\rho(\mathbf{r})$ is the physical variable that fixes all the ground state properties of the many-body system. In particular, the energy of the system can be written as a functional of the one-body density

$$E = \int \mathcal{H}[\rho(\mathbf{r})] d\mathbf{r} \,, \tag{1.1}$$

where $\mathcal{H}[\rho(\mathbf{r})]$ is the energy density functional. The particle density $\rho(\mathbf{r})$ of the system is then obtained minimizing the total energy.

The theorem establishes the existence and uniqueness of this energy functional, but it does not provide any method to determinate the exact expression. Due to the lack of a rigorous procedure different approximations have to be made. The functional is constructed for each particular system on the basis of physical arguments.

Since the proposal by Stringari of a density functional for liquid helium derived from an effective Skyrme-like interaction [4], it has been used with success in a variety of problems, becoming a reliable tool in situations where a fully microscopic approach is prohibitive, like finite systems at non-zero temperature or nucleation in liquid helium. More elaborated density functionals have also been proposed, for example using a finite range interaction and incorporating hard core effects [5, 6] or taking into account backflow effects [7]. Whereas many-body techniques appear unfeasible to deal with finite temperature and inhomogeneities in most of the problems, density functional methods are becoming more and more accurate for describing inhomogeneous phases of quantum liquids.

In this thesis we are concerned with the density functional description of homogeneous cavitation and nucleation in liquid helium at low temperatures, i.e., that occurring in the bulk of the liquid phase, free of impurities. We thus will not pay attention to the important practical subject of heterogeneous nucleation by impurities, on surfaces or on electron bubbles.

Phase transitions under equilibrium conditions are experimentally well determined as they take place in the coexistence regime, for example the normal boiling point of a liquid or the equilibrium freezing point. However, phase transitions do not always occur under equilibrium conditions. As the new phase forms, the free energy of the system is lowered. But close to the equilibrium transition point, the original phase can be held in a metastable state. Superheated liquids and supercooled vapors are examples of metastable systems. Although they are internally stable, there exists in each case another configuration having a lower thermodynamical potential. The metastable state is separated from the stable one by some thermodynamical barrier. Due to statistical fluctuations in density or concentration, that barrier can be overcome as a result of the formation and growth of small clusters of the new stable phase in the metastable state (bubbles in the liquid or droplets in the vapor; bubbles and droplets will be here generically referred to as clusters). So, nucleation is the process of first localized appearance of a new stable phase in a metastable state which will potentially play a role in the dynamics of every first-order phase transition. The nucleation process can be achieved thermally or by quantum tunneling, and depending on the energy barrier the nucleation rate will be slow or very fast. When the rate is slow, large deviations from equilibrium may be required before the first localized stable phase appears.

Within the so-called classical theory of nucleation (see for example references [8, 9, 10] and references therein), the grand potential of the growing drop is evaluated in the capillarity approximation. It consists in treating the drop as a piece of bulk liquid limited by a sharp surface. Such a macroscopic approximation has at least two obvious shortcomings. First, the neglecting of any compressional effect on the central density of the drop due to its surface. This is what one calls a finite size effect, like the change in energy of the cluster due to curvature corrections. These corrections can be incorporated as variations of the surface energy with size, leading to a kind of droplet model for homogeneous nucleation [11]. The second shortcoming is originated by the unability of the model to take into account the modification in the surface energy of the cluster due to the presence of vapor as T increases. These limitations, certainly important for small size clusters, can be overcome using a density functional to calculate the thermodynamical properties of the system [9, 12, 13, 14], and this indeed constitutes our starting point.

This thesis is organized as follows. In chapter 2 we study thermal nucleation at low temperatures in pure ^{3}He and ^{4}He at negative and positive pressures, by means of an energy density functional for each isotope which takes into account thermal effects.

Since ^{3}He has a finite solubility in ^{4}He at zero temperature and liquid helium is usually a mixture of both isotopes, we study in chapter 3 cavitation in ^{3}He-^{4}He mixtures. At negative pressures and at different ^{3}He concentrations below and above saturation, we study the dependence on ^{3}He concentration of the configuration that likely drive the nucleation process (bubble or ^{3}He-rich drop), and the homogeneous cavitation pressure. Supersaturated mixtures at positive pressures are also studied. Since the process of nucleation at positive pressures gives too large a critical concentration value as compared with the experimental one, we discuss the small degree of supersaturation found in ^{3}He-^{4}He mixtures at positive pressures by means of ^{4}He vortex destabilization in the mixture, i.e., vortices with cores rich in ^{3}He.

At sufficiently low temperatures the rate at which thermal activation over the energy barrier occurs becomes very small. Nucleation must then be dominated by quantum tunneling through the barrier. In chapter 4 we study cavitation in liquid helium due to quantum tunneling. We analyze in the whole range of allowed negative pressures, the crossover temperature for each isotope at which thermal and quantum cavitation compete. Finally, the conclusions are drawn in chapter 5.

Chapter 2

Thermal nucleation and cavitation in ^{3}He and ^{4}He

Motivated by recent experimental work on cavitation in superfluid ^{4}He [15, 16], we have undertaken the study of thermal cavitation in both helium isotopes at high densities to investigate the formation of bubbles in the liquid, while at low densities, the reverse situation, i.e., drop formation in helium vapor, is considered.

The basic tool for this study is constituted by two free energy density functionals, one for each isotope, that have been constructed to describe with accuracy the equation of state, liquid-vapor equilibrium and thermal properties of the interface [17, 18]. These functionals allow one to obtain the nucleation (cavitation) barrier within an improved version of the homogeneous nucleation theory as indicated for example by Xiong and Maris [12], and by Oxtoby [8].

Theoretical investigations of liquid helium properties at negative pressures [12, 19, 20, 21] have been prompted by recent experiments carried out by Nissen et al. [15], and Xiong and Maris [16] using ultrasonic waves. They have performed experiments on the negative pressure required to produce nucleation of bubbles in ^{4}He, with similar apparatus in which ultrasonic waves generated by a hemispherical transducer were focussed for a short time into a small volume in the interior of the liquid, not in contact with any container wall, considerably avoiding the possibility of heterogeneous nucleation. The magnitude of this negative nucleation pressure is also called tensile strength.

Although the experimental results reported in [15] for ^{4}He at temperatures T above 1.5 K seemed to be well reproduced by Classical Nucleation Theory (ClNT) [22], the experiment carried out in [16] appears to discard this possibility. A serious argument against the interpretation of the experimental findings of [15], already raised in [16] and confirmed in [21, 23], is that the spinodal pressure P_{sp} at which liquid ^{4}He becomes *macroscopically* unstable is bigger than the homogeneous cavitation pressure yielded by ClNT and by the experiment reported in [15].

Using ultrasonic waves, Xiong and Maris have found that the tensile strength for nucleation of bubbles in ^{4}He for temperatures in the 0.8 K - 2 K range, is $\sim$ 3 bar. To analyze their experimental results, they have resorted to a model that represents a considerable improvement over the ClNT. It is based on a density functional (DF) whose free parameters are fixed at $T = 0$ to yield the experimental velocity of sound propagation in the liquid as a function of the density* ρ, and includes a gradient term $\lambda(\nabla\rho)^2$ adjusted so as to reproduce the surface tension of ^{4}He at $T = 0\,$K. They have assumed that the surface energy and the equation of state are temperature independent.

Considering thermal activation they have found a tensile strength that goes from $\sim$ 9 bar at $T \sim 0\,$K, to $\sim$ 6.5 bar at $T = 2\,$K, still lying in absolute value well above their experimental data. Several may be the reasons for this disagreement. The first is the validity of their functional in the density domain corresponding to negative pressures. However, since other equations of state obtained within the density functional framework [21] (see also below), as well as within a quadratic diffusion Monte Carlo method using an improved Aziz potential [23] yield very similar values for P_{sp} (around $\sim -9\,$bar at $T = 0\,$K), we do not believe this to be the cause of the disagreement. Another reason may be the zero-temperature description of the liquid. The nucleation process is strongly influenced by the surface tension which exhibits a strong dependence upon temperature [17, 18]. However, since at low temperatures the surface tension is a very smooth function of T [17, 18], it can be approximated by the value at $T = 0$. So, we do not expect either the zero temperature DF to be the cause of the disagreement. In spite of that, a study including thermal effects is called for to

---

*They have extrapolated measurements of the sound velocity of helium at positive pressures to estimate the equation of state for negative pressures.

state which part of the discrepancy comes from other effects not taken into account in the calculation. We will see that the inclusion of thermal effects in the calculation of the barrier against nucleation, results in a sizeable decrease of the tensile strength above 1.5 K. Thus, the disagreement with the experimental data still remains. As if they claim, the ultrasonic technique used in these experiments discards the possibility of heterogeneous nucleation, nucleation on vortex lines could be a possible origin of the discrepancy.

In this chapter we want to address the effect that a non-zero temperature has on the nucleation barrier, since it has been overlooked in all previous calculations and thus, it is of relevance to put on a firmer basis which part of the disagreement between theory and experiment can be attributed to nucleation of bubbles on a vortex line in the case of ^{4}He at negative pressures or even to other undetected effects. For ^{3}He, our results constitute the first detailed study of the tensile strength using a realistic DF, and can be of some relevance in view of the planned experiments on this helium isotope [16].

We shall show that our results on cavitation at positive pressures are in agreement with the experimental data [24, 25], opposite to the situation for ^{4}He at negative pressures [13]. We are not aware of existing experimental results for nucleation in either helium isotope away from the critical point. The critical region is deliberately excluded from our calculations because of the intrinsic limitations of the density functionals we are using [17, 18], as well as the very low temperature region in which nucleation through quantum tunneling may play a significant role [26]†. Notwithstanding, the present study almost spans the whole liquid-gas equilibrium region, making quite distinct predictions in physical situations where no experimental information is available.

This chapter is organized as follows. In section 2.1 we review the density functional approach to the nucleation problem. Then we present the results for both isotopes. In section 2.2 and 2.3 we consider cavitation at negative [13] and positive [27] pressures, respectively. Finally, in section 2.4 we study formation of drops in the vapor [27].

[†] This subject will be throughoutly studied in chapter 4.

2.1 Thermal nucleation within a density functional approach

Our starting point is the following free energy functional [17, 18] for either helium isotope:

$$\begin{aligned} f(\rho,T) &= f_{ni}(\rho,T)+\frac{1}{2}b\rho^2+\frac{1}{2}c\rho^{2+\gamma}+\beta\frac{(\nabla\rho)^2}{\rho}+\xi(\nabla\rho)^2 \\ &\equiv f_v(\rho,T)+\beta\frac{(\nabla\rho)^2}{\rho}+\xi(\nabla\rho)^2\,, \end{aligned} \tag{2.1}$$

where ρ is the particle density and f_{ni} is the well-known free energy density of a noninteracting Bose or Fermi gas [28]. The b- and c-terms are the contribution due to the interatomic interaction, the β-term is the correction to the kinetic energy density (standard Weizsäcker correction for ^{3}He) and the ξ-term is the surface correction to the interaction energy. The density gradient terms vanish when the system is homogeneous, in which case $f(\rho,T)$ reduces to $f_v(\rho,T)$. The parameters b, c, γ, β and ξ have been adjusted so as to reproduce physical quantities such as the surface tension, equation of state and vapor pressure along the coexistence line.

We want to point out that the surface tension as a function of T, the isotherms and the vapor density in equilibrium with the liquid phase are well reproduced by our model up to temperatures above the ones of interest for the present study. This is of especial relevance for a quantitative study of homogeneous nucleation and cavitation in the liquid-gas transition.

2.1.1 Metastable region

Before studying cavitation and nucleation, it is convenient to consider the phase equilibrium diagram and to delimit the metastable region where clusters of the new stable phase will be formed. Figure 2.1 shows a schematic picture of the phase equilibrium diagram in the pressure–density plane, which may represent either helium isotope[‡].

For a given T, the densities of the liquid and vapor in equilibrium (ρ_L and ρ_V, respectively) are found imposing that the pressure and chemical potential of both

[‡] Strictly speaking, the $T=0$ isotherm in this figure corresponds to the ^{4}He case. For ^{3}He at low densities, one would have the pressure of the free Fermi gas, i.e., the pressure should increase even at zero temperature.

phases be the same, i.e.,

$$\begin{aligned} P(\rho_L, T) &= P(\rho_V, T) \\ \mu(\rho_L, T) &= \mu(\rho_V, T), \end{aligned} \tag{2.2}$$

with P and μ calculated from f_v. These equations have a non-trivial solution only for T below a critical value T_c. For $T < T_c$ one obtains two curves $\rho_L = \rho_L(T, P)$ and $\rho_V = \rho_V(T, P)$ which intersect at $T = T_c$, and define the two-phase equilibrium line (dashed-dotted line in Fig. 2.1). The region below this curve is the two-phase coexistence region, which splits into two domains. One is the unstable region in which the system cannot exist as an uniform phase because the stability condition

$$\left(\frac{\partial P}{\partial \rho}\right)_T > 0 \tag{2.3}$$

is not satisfied. And the other one is the metastable region, corresponding to overheated liquid and overcooled gas, where the system can remain homogeneous until a small perturbation drives it into a two-phase equilibrium state. These domains are separated by the classical spinodal curve defined as

$$\left(\frac{\partial P}{\partial \rho}\right)_T = 0. \tag{2.4}$$

The spinodal line is represented in Figure 2.1 by the solid line labeled sp, and the metastability region corresponds to the hatched zone limited by the spinodal and the two-phase coexistence curves. Both curves are tangent at the critical point (P_c, T_c). Three generic isotherms are also drawn in that figure.

We have obtained the liquid-gas coexistence line and the spinodal line, by solving Eqs. (2.2) and (2.4), where P and μ are calculated by means of the free energy functional (2.1) for an homogeneous system. These calculations involve only algebraic equations, since only $f_v(\rho, T)$ comes into play.

The liquid may be experimentally driven into a metastable state using some superheating technique in which the temperature of the liquid is raised at constant pressure (going from point 1 to point 2, see Fig. 2.1) or decreasing the pressure at constant temperature (going from point 1 to point 2'). This technique can also be used to probe the tensile strength of the liquid when the pressure is reduced to negative values.

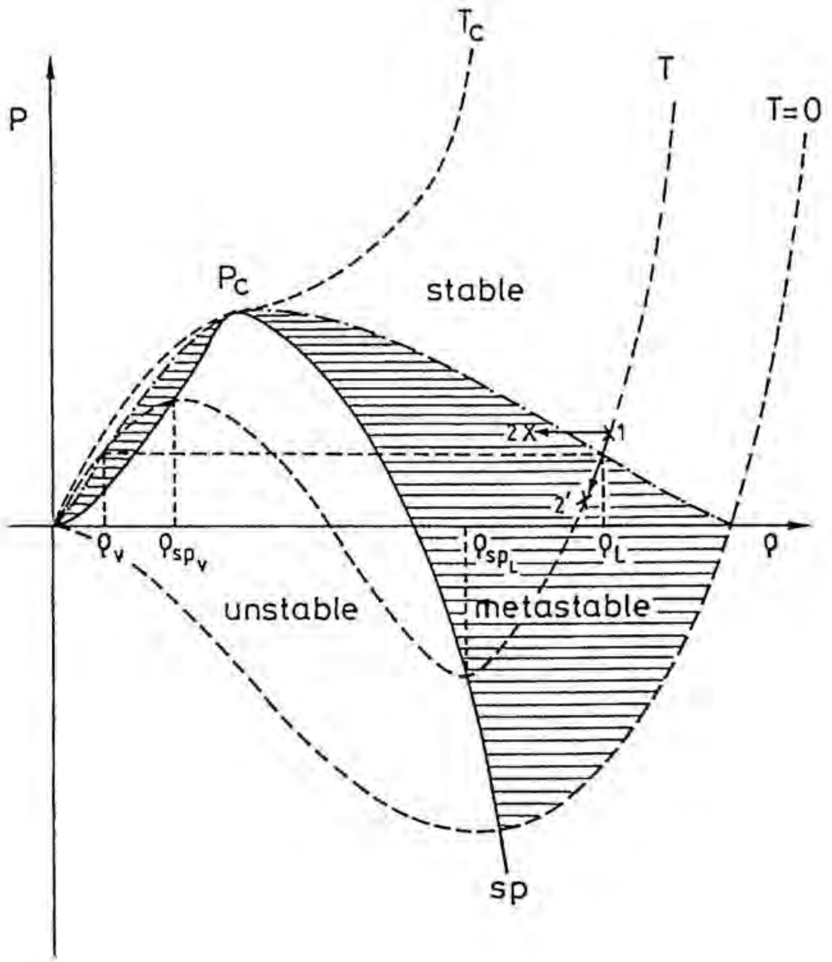

Figure 2.1. Schematic representation of the liquid-gas equilibrium. The solid line labeled sp is the spinodal line, and the dash-dotted line is the two-phase equilibrium line. The regions of stability, metastability and unstability of the one-phase system are also indicated.

2.1.2 Critical bubble and barrier height

Those processes cause the system to cross the liquid-gas equilibrium line, penetrating into the metastable zone. At this point the nucleation process is activated. The dynamics of the first-order phase transition corresponding to liquid-gas separation can be regarded as the formation of clusters of a new phase in the homogeneous metastable medium: bubbles in the metastable liquid (cavitation) or drops in the metastable vapor (nucleation); for sizes smaller than a critical one, these clusters shrink, but beyond a critical radius, they grow to trigger the phase separation. This suggests the existence of an energy barrier that prevents the metastable system from decaying into the stable phase, whose height is determined by the free energy required to form the critical nucleus. The critical cluster is then in unstable equilibrium with the metastable system.

The application of the density functional approach to the nucleation problem proceeds in two steps. First, one determines the critical cluster density profile in a given metastable state and the energy involved with its formation. And second, at a given T, the pressure at which the number of critical clusters formed per unit time and volume equals a conventional number, say one per second and cubic centimeter, to indicate the onset of phase separation.

Critical clusters are calculated at different metastability conditions (P, T) which have associated a certain uniform density $\rho_m = \rho_m(T, P)$. In fact, we have proceeded as follows: at given $T < T_c$ we pick up a density ρ_m for which the system is in the metastable region. For example, at the intermediate T shown in Fig. 2.1, ρ_m will lie between ρ_{sp_L} and ρ_L (superheated liquid: bubble formation) or between ρ_V and ρ_{sp_V} (undercooled vapor: drop formation), where ρ_{sp_L} and ρ_{sp_V} are the spinodal densities at that temperature T, corresponding to the liquid and vapor destabilization, respectively. Given (ρ_m, T), since the metastable state is homogeneous, the pressure of the system is $P(\rho_m, T) = -f_v(\rho_m, T) + \mu\rho_m$, which will be positive or negative depending on the choice of ρ_m (see Fig. 2.1).

The density profile of the critical cluster is obtained solving the Euler–Lagrange equation

$$\frac{\delta f}{\delta \rho} = \frac{\partial f}{\partial \rho} - \nabla \frac{\partial f}{\partial \nabla \rho} = \mu \ , \tag{2.5}$$

where μ is the chemical potential of the homogeneous metastable system at (ρ_m, T). We have solved Eq. (2.5) with spherical symmetry. The boundary conditions for the physical solution are $\rho'(0) = 0$ and $\rho(r \to \infty) = \rho_m$.

The nucleation barrier $\Delta\Omega$, i.e., the energy required to form the critical cluster, is finally obtained from the difference between the grand potential of the critical cluster and of the homogeneous metastable system:

$$\Delta\Omega = \int d\mathrm{r}\,[f(\rho,T) - f_v(\rho_m,T) - \mu(\rho-\rho_m)]\,. \tag{2.6}$$

Since $P = P(\rho_m, T)$, Eq. (2.6) yields $\Delta\Omega = \Delta\Omega(P,T)$. Fixed T, we calculate $\Delta\Omega$ for several pressures along the isotherm. There are two physical requirements on the nucleation barrier $\Delta\Omega$ that can serve as a check of the validity of an approach to the nucleation problem:

i. $\Delta\Omega$ must drop to zero at the corresponding spinodal pressure, since at that point the homogeneous system becomes macroscopically unstable, and

ii. $\Delta\Omega$ must diverge when P approaches the vapor pressure value (on the two-phase equilibrium line), since the homogeneous system becomes stable.

This simply indicates that, to have an appreciable probability of forming a bubble, the system has to be immersed deeply inside the two-phase equilibrium region, since the probability for any of these critical clusters to be thermally nucleated at a certain T is given by the exponential factor $\exp(-\Delta\Omega/kT)$, i.e., fixed T, the probability increases when the barrier height decreases.

It is worth it to mention [8, 10] that a weak point of the classical theory is that it yields nonvanishing barriers at the spinodal line. As we will see in the following sections[§], the limiting behaviour of $\Delta\Omega$ is well reproduced in our scheme. We thus conclude that the physical requirements of stability and unstability are satisfied by the energy barriers obtained within our density functional approach.

2.1.3 Thermal nucleation rate and homogeneous nucleation pressure

The thermal nucleation rate J_T, i.e., the number of drops or bubbles formed in the homogeneous system per unit time and volume at a given temperature T due to thermal fluctuations, is given in the original Becker–Döring [22] theory by the expression

$$J_T = J_{0T}\,exp\,(-\Delta\Omega/kT)\,, \tag{2.7}$$

[§] See Figs. 2.2, 2.5 and 2.9.

the exponential term gives the probability of forming a critical cluster by thermal activation, where $\Delta\Omega = \Delta\Omega(P, T)$ is the energy barrier height required to form the critical cluster in the metastable system, and k is the Boltzmann constant. The preexponential factor J_{0T} gives information about the number of clusters that can be formed per unit time and volume. It depends on the characteristics of the system and on the dynamics of the nucleation process [29].

At a given temperature, the rate of bubble formation rises abruptly with decreasing¶ P due to its exponential dependence on $\Delta\Omega$. In a typical experiment of cavitation, one applies a given pressure to an experimental volume V for a time τ and determines whether or not cavitation occurs. There is an appreciable probability of cluster formation when

$$J_T(P, T)\,(V\tau)_e \sim 1\,. \tag{2.8}$$

Thus at a given T, in view of (2.8), the pressure at which nucleation occurs will depend on the experimental volume and time. However, because J_T changes rapidly for small variations of P, the pressure that satisfies Eq. (2.8) depends only weakly on the values of V and τ, and one can consider that cavitation occurs at a fairly definite threshold pressure $P_h(T)$, which is called homogeneous nucleation pressure.

To make a sensible comparison with the experimental results of [16, 24], we have solved

$$J_{0T}\, exp\,(-\Delta\Omega/kT) = (V\tau)_e^{-1} \tag{2.9}$$

where the choice $(V\tau)_e = 2.5\cdot 10^{-13}$ cm^{3}sec corresponds to solving the equation for the experimental conditions of [16] and $(V\tau)_e = 1$ cm^{3}sec corresponds to the experimental conditions of [24].

To solve Eq. (2.9) for P_h, an expression for the preexponential factor has to be chosen. There are many proposals of different complexity in the literature, see for example Refs. [8, 12, 24, 25] and references therein. Following Lifshitz and Kagan [26], and Xiong and Maris [12] we have taken

$$J_{0T} \sim \frac{\nu}{V_0}\,, \tag{2.10}$$

where ν is the attempt frequency and V_0 is the volume of the critical cluster, being $1/V_0$ an upper bound of the number of virtual centers of formation of the new phase

---

¶See Fig. 2.3. The rate of drop formation rises abruptly with increasing P.

per unit volume. For simplicity, it is taken $\nu = kT/h$ and for V_0 the volume of a sphere of radius 10 Å representing the critical cluster, although as a matter of fact the radius of the critical cluster increases with temperature[||]. In spite of that, since P_h is not very sensitive to the value of $(V\tau)_e$ that multiplies J_{0T}, it will not be sensitive to small variations of the prefactor either. We have thus taken the generic value of 10 Å in the prefactor J_{0T} for all temperatures. Rewriting (2.10), the prefactor reads

$$J_{0T} = \frac{3kT}{h4\pi 10^3} \,. \tag{2.11}$$

To have an idea of the order of magnitude of this preexponential factor, for $T = 4$ K one has $J_{0T} \sim 2 \cdot 10^{31}$ cm^{-3}sec^{-1}, while for the same temperature Sinha et al. [24] have $J_{0T} \sim 2 \cdot 10^{33}$ cm^{-3}sec^{-1}. A variation of two orders of magnitude in J_{0T}, which is also obtained when the preexponential factor is calculated by means of theories developed to describe the dynamics for the formation of critical clusters [8], does not affect in any appreciable way the solution of Eq. (2.9).

2.2 Cavitation at negative pressures

We have studied bubble formation at negative pressures. First, we have obtained the critical bubbles by solving the EL equation (2.5), where in this case μ is the chemical potential corresponding to any density ρ_m such that the pressure of the homogeneous liquid $P(\rho_m, T)$ is negative, corresponding to a metastable state. Then we have calculated the nucleation barriers with Eq. (2.6). As we have commented above, our T-dependent functional approach yields $\Delta\Omega = \Delta\Omega(P,T)$. In Fig. 2.2 we plot the barriers $\Delta\Omega$ as a function of P for several temperatures in the case of ^{4}He (a) and ^{3}He (b). As expected, for a given T, $\Delta\Omega$ drops to zero at the corresponding spinodal pressure, and diverges at the saturation one. At low T the saturation pressure is ~ 0 and the spinodal one is about -9 bar for ^{4}He and -3 bar for ^{3}He [13], and the T-curves show a large kind of plateau (in a logarithmic scale). The divergences of $\Delta\Omega$-curves at saturation (P_{sat}) are not shown in Fig. 2.2 but they can be guessed.

[||] See Figs. 2.8 and 2.11.

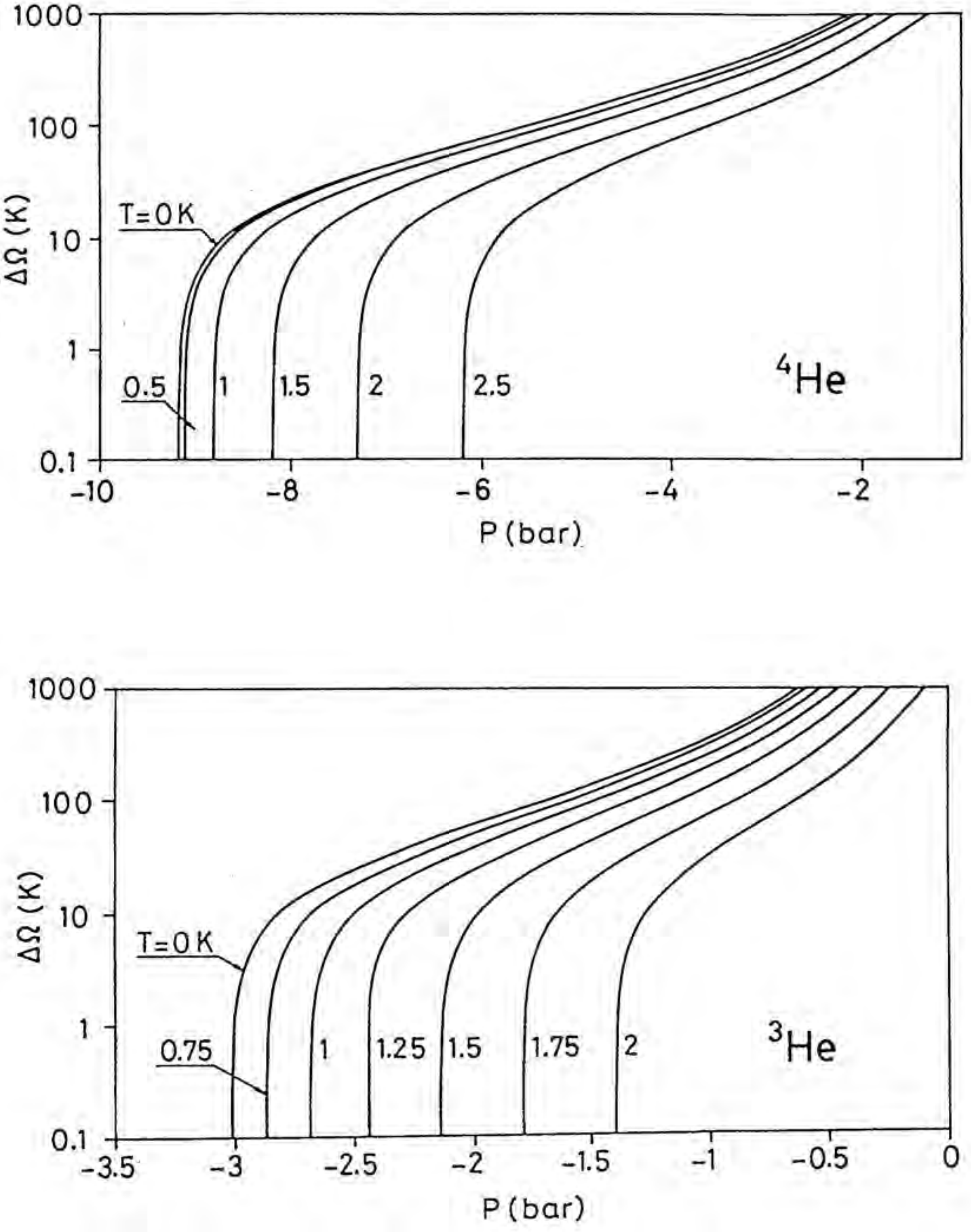

Figure 2.2. Nucleation barriers $\Delta\Omega$ for ^{4}He (a) and ^{3}He (b) as a function of pressure corresponding to bubble formation at negative pressures and several temperatures T.

The inclusion of thermal effects in the calculation (compare $\Delta\Omega(T)$ and $\Delta\Omega(T=0)$) lowers the nucleation barrier because the surface tension decreases with increasing T [17, 18]. It means that the energetical cost of forming the interface between the two phases decreases and thus, the required energy to form the critical bubble is lowered. The capillarity approximation** can provide a rough idea about the role played by the surface tension in the nucleation process, where the dependence of the energy barrier with the surface tension σ goes like $\sim \sigma^3$. Another consequence is that the density inside the bubble increases, thus making its structure more similar to the homogeneous metastable phase.

Fig. 2.3 shows J_T for ^{4}He and ^{3}He. The dashed lines correspond to nucleation rates calculated from the $\Delta\Omega(T=0)$ barrier. One can see that a better estimate of $\Delta\Omega(T)$, since its value is lowered, increases J_T more than one order of magnitude at pressures relevant for bubble nucleation. It is worth noting how rapidly J_T increases with decreasing P.

We have obtained the negative homogeneous nucleation pressure solving Eq. (2.9) with the experimental volume V and time τ taken from [16], i.e., $(V\tau)_e = 2.5 \times 10^{-13}$cm^3 sec, to allow for a sensible comparison with their results for ^{4}He.

P_h is shown in Fig. 2.4 as a function of T for ^{4}He [Fig. 2.4(a)] and ^{3}He [Fig. 2.4(b)]. The short-dashed line has been obtained from $\Delta\Omega(T=0)$, and the small difference between this curve and Xiong and Maris results (dashed-dotted line) for ^{4}He is due to the different DF used in both calculations. For comparison, we also show the critical pressure $P_{sp}(T)$ (long-dashed line) at which liquid He becomes macroscopically unstable (spinodal line). It is worth it to remark that the T-independent approach is valid at temperatures below 1 K (0.2 K) for ^{4}He (^{3}He), since at this temperature range the surface tension diminishes smoothly enough [17, 18] to take as first approximation the value $\sigma(T=0)$. At moderated temperatures the use of $\Delta\Omega(T=0)$ to obtain J_T constitutes a poor approximation, yielding a tensile strength bigger in absolute value than $|P_{sp}|$ at T ~ 1.5 K for ^{3}He and at $T \sim 2.5$ K for ^{4}He, where this approximation breaks down.

**See Sec. 3.3.1.

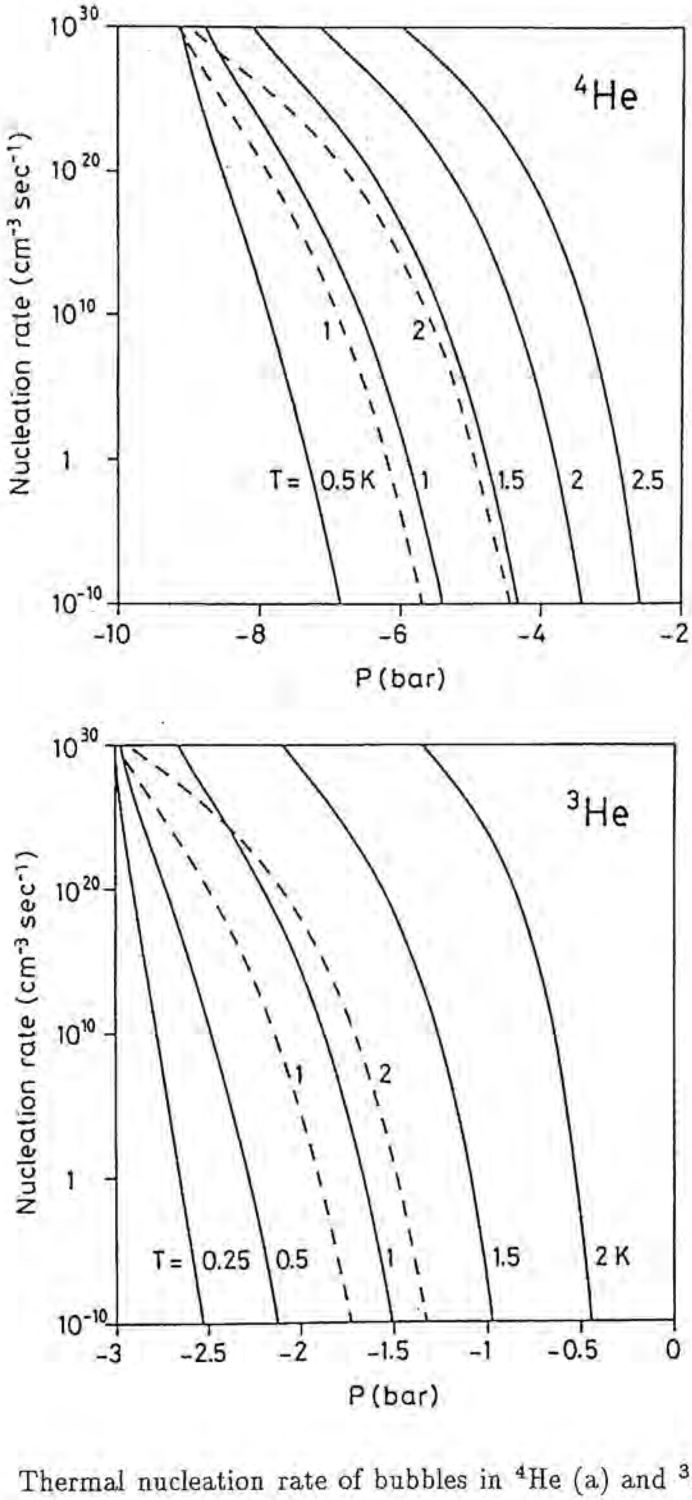

Figure 2.3. Thermal nucleation rate of bubbles in ^{4}He (a) and ^{3}He (b) as a function of pressure for several temperatures T. The dashed lines represent the nucleation rates obtained from the $\Delta\Omega(T = 0)$ barrier.

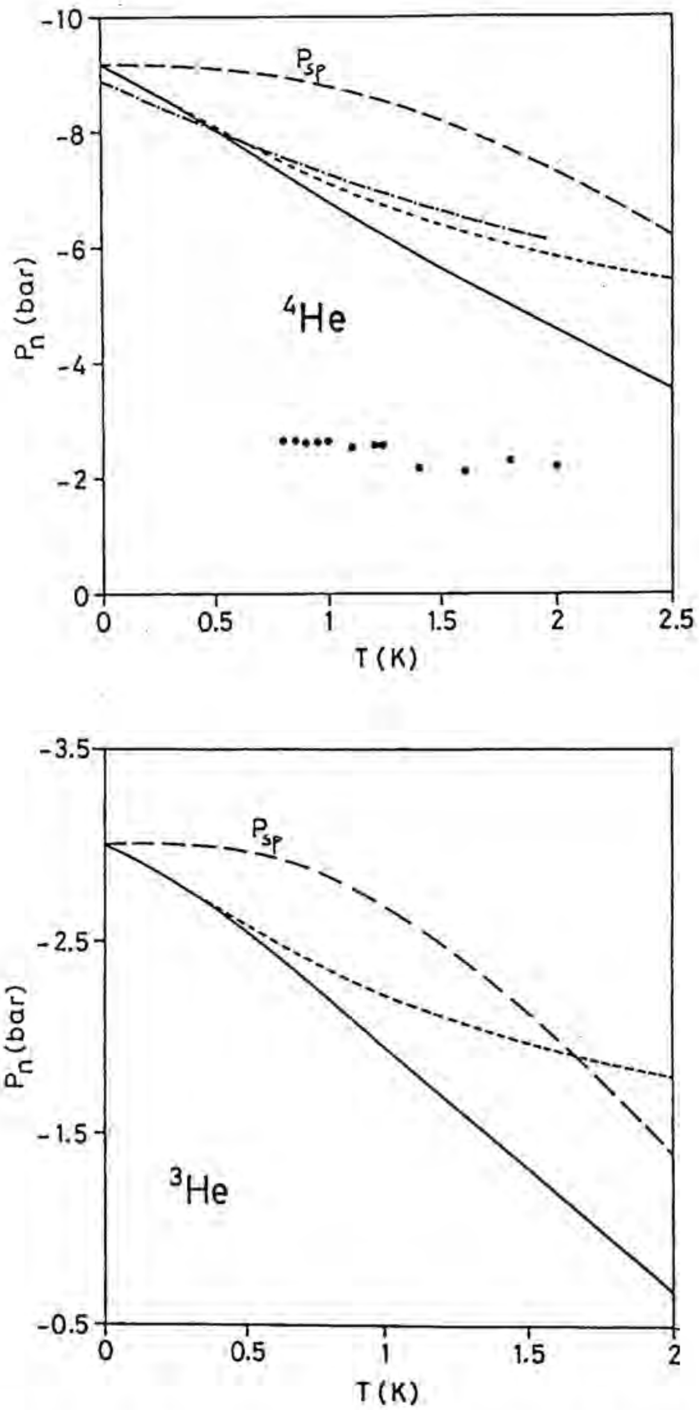

Figure 2.4. P_h needed to cause nucleation in ^{4}He (a) and in ^{3}He (b) corresponding to a product of experimental volume and time equal to 2.5×10^{-13}cm^3 sec. The dashed-dotted line and dots are the theoretical and experimental results of Ref. [16], respectively. The thick line has been obtained from the $\Delta\Omega(T)$ barrier, and the short-dashed line from the $\Delta\Omega(T = 0)$ barrier. The spinodal line $P_{sp}(T)$ is represented by a long-dashed line.

2.3 Cavitation at positive pressures

The energy barriers for bubble formation at positive pressures are plotted in Fig. 2.5. At high temperatures, the curves are almost vertical, since the spinodal ($\Delta\Omega = 0$) and the saturation ($\Delta\Omega \to \infty$) pressures are close. If classical nucleation is applied, none of these T-curves will cross the P-axis. These barriers resemble ours for large values but abruptly separate for small ones, going asymptotically to zero when $P \to -\infty$ instead of converging towards the spinodal pressure.

P_h is shown in Figure 2.6 as a function of T for ^{4}He [Fig. 2.6(a)] and ^{3}He [Fig. 2.6(b)]. The solid curves have been obtained using $(V\tau)_e = 1$ cm^3 sec, and the dashed curves with $(V\tau)_e = 2.5 \cdot 10^{-13}$ cm^3 sec. It is worth noting that the results of the calculation are rather insensitive to the precise value of $(V\tau)_e$ (compare the solid and dashed curves, whose $(V\tau)_e$ differ in 13 orders of magnitude).

In these figures we have also plotted the spinodal line P_{sp}, and the vapor saturation curve P_{sat} as a function of T. The dots are experimental points taken from [24] for ^{4}He, and from [25] for ^{3}He. One can see that the agreement between theory and experiment is very good for ^{4}He indicating that the density functional approach to homogeneous nucleation theory applies to bubble formation in ^{4}He at positive pressures. Concerning ^{3}He, the agreement is fairly good; our calculations are less than 0.1 K above the experimental results. This discrepancy could be attributed to a failure of the ^{3}He functional at such high temperatures (the ^{4}He one turns out to work much better, see [17, 18]), or to an experimental underestimation of the homogeneous nucleation temperature. This possibility is indicated, although ruled out, by Lezak et al. [25].

Comparing P_{sat} with P_h in Fig. 2.6, one can see for example, that for ^{4}He at $T = 4.2$ K, the pressure has to be reduced from its value at saturation around 0.5 bar to get cavitation, while a reduction of 0.25 bar is enough at $T \sim 4.8$ K. For ^{3}He, the reduction at $T \sim 2.5$ K is around 0.35 bar, and ~ 0.1 bar at $T \sim 2.9$ K. An alternative way to read this figure is that, at $P = 1$ bar, one needs to increase T around 0.4 K to produce cavitation in ^{4}He, whereas an increase of ~ 0.1 K is necessary at $P = 1.5$ bar.

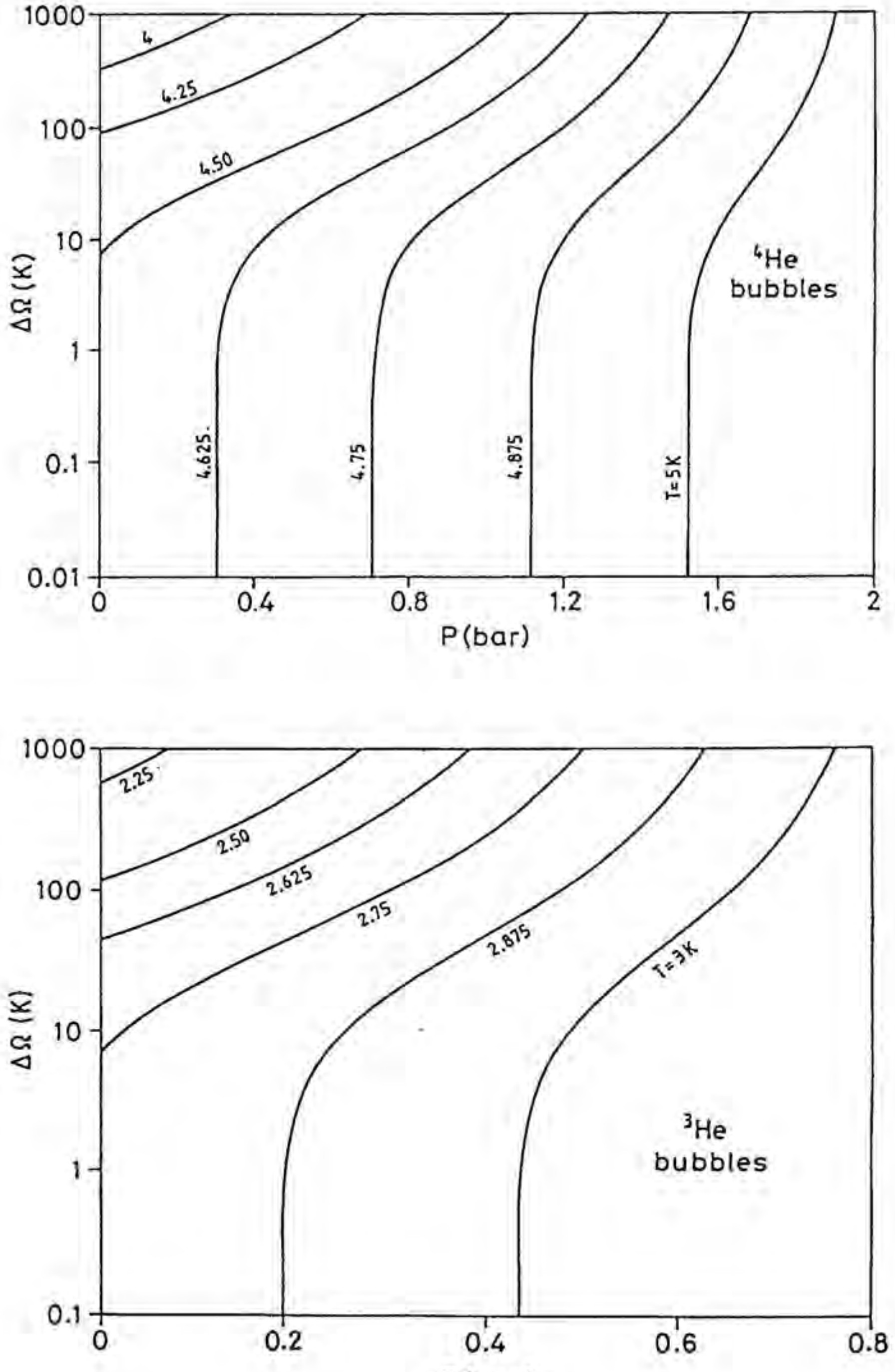

Figure 2.5. Nucleation barriers as a function of pressure for ^{4}He (a) and ^{3}He (b) corresponding to bubble formation, at positive pressures.

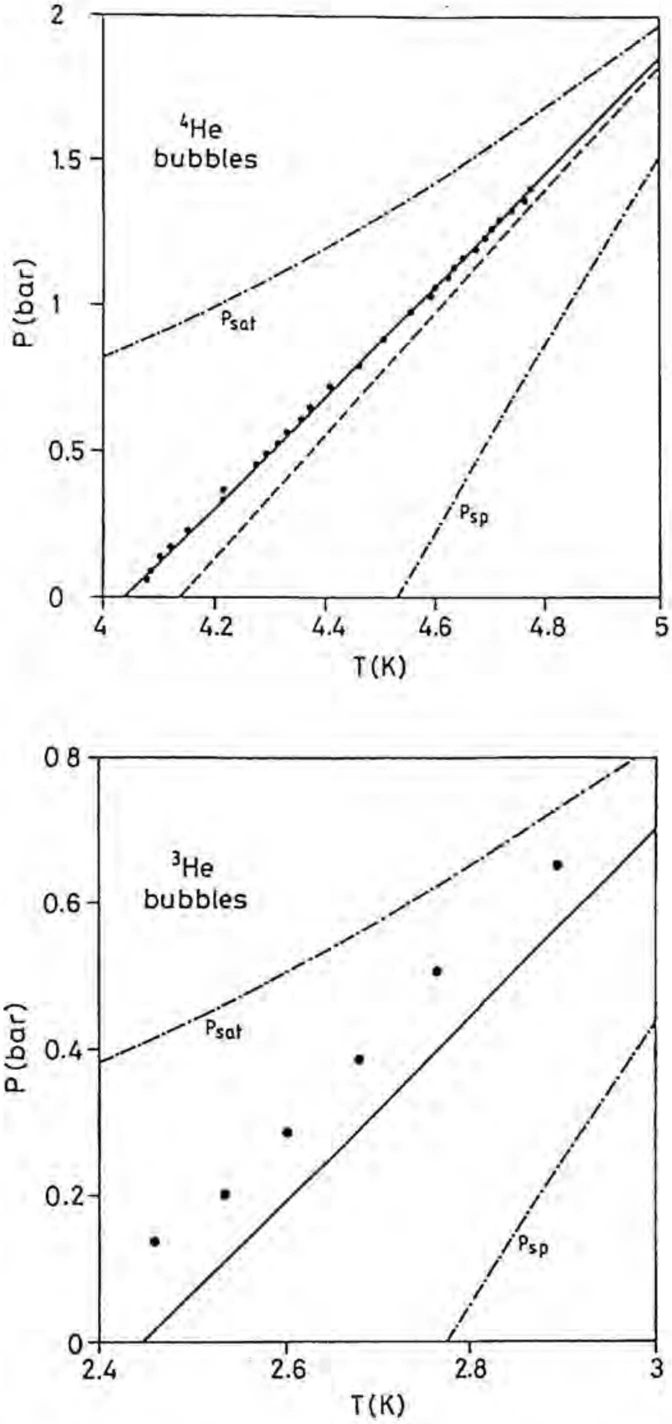

Figure 2.6. Homogeneous cavitation pressure as a function of temperature for ^{4}He (a) and ^{3}He (b) at $P > 0$. The solid curves have been obtained using $(V\tau)_e = 1$ cm^3 sec, and the dashed ones using $(V\tau)_e = 2.5 \cdot 10^{-13}$ cm^3 sec. The experimental points are from [24] (^{4}He), and from [25] (^{3}He). The saturation vapor pressure line is indicated as P_{sat}, and the spinodal line as P_{sp}.

For the sake of completeness we plot in the same figure the results we have obtained for cavitation at negative (Fig. 2.4) and positive pressures (Fig. 2.6), Fig. 2.7 shows the pressures for homogeneous bubble formation from $T = 0$ to the vicinity of the critical point, which is indicated by a cross. The results below $T \leq 0.15$ K should be considered only as indicative, since we have neglected quantum tunneling [26]. As in Fig. 2.6, the solid line represents P_h for $(V\tau)_e = 1$ cm^3 sec and the dashed line, for $(V\tau)_e = 2.5 \cdot 10^{-13}$ cm^3 sec. Both curves merge with the spinodal line P_{sp} at $T = 0$. The influence of the precise value of $(V\tau)_e$ on P_h turns out to be more sizeable for negative P_h, which happens for $T \leq 4$ K for ^{4}He, and for $T \leq 2.4$ K in the case of ^{3}He (see Fig. 2.6). The dots in Fig. 2.7(a) are the experimental points of [16]. The possible origin of the discrepancy between the calculated P_h and the experimental results has been already discussed in the previous section.

The present results show the interest of performing experiments on ^{4}He above the λ transition ($T_\lambda = 2.17$ K), but still for temperatures such that $P_h < 0$, i.e., $T \leq 4$ K. Indeed, at high temperatures the density functional approach yields results in good agreement with those obtained from the classical theory [24]. This can be easily understood if one realizes that at these temperatures the critical bubbles are large (see Fig. 2.8), so that finite size effects are less important. As T decreases, the critical bubbles get smaller and the classical theory becomes less reliable, whereas the density functional approach still applies. If this is the case, the remaining discrepancy between theory and experiment below T_λ could be attributed, on firmer grounds, to the role played by vortices in the process of cavitation in superfluid ^{4}He. Alternatively, the planned experiments on cavitation in ^{3}He [16] could help understanding if the existing discrepancy for ^{4}He is still due to shortcomings of the density functional approach.

Figure 2.8 shows the density profile of several critical bubbles we have found in ^{4}He and ^{3}He. Their size grows as T increases due to the decrease of the surface tension. It is also interesting to observe the filling of the bubble with gas as T increases, and the appreciable increase of the surface diffuseness as it happens for the liquid surface at saturation [17, 18]. The comparatively large value of asymptotic density for ^{4}He at $T = 2$ K reflects the experimental fact that the density of the liquid at saturation presents a maximum for $T \sim 2.2$ K.

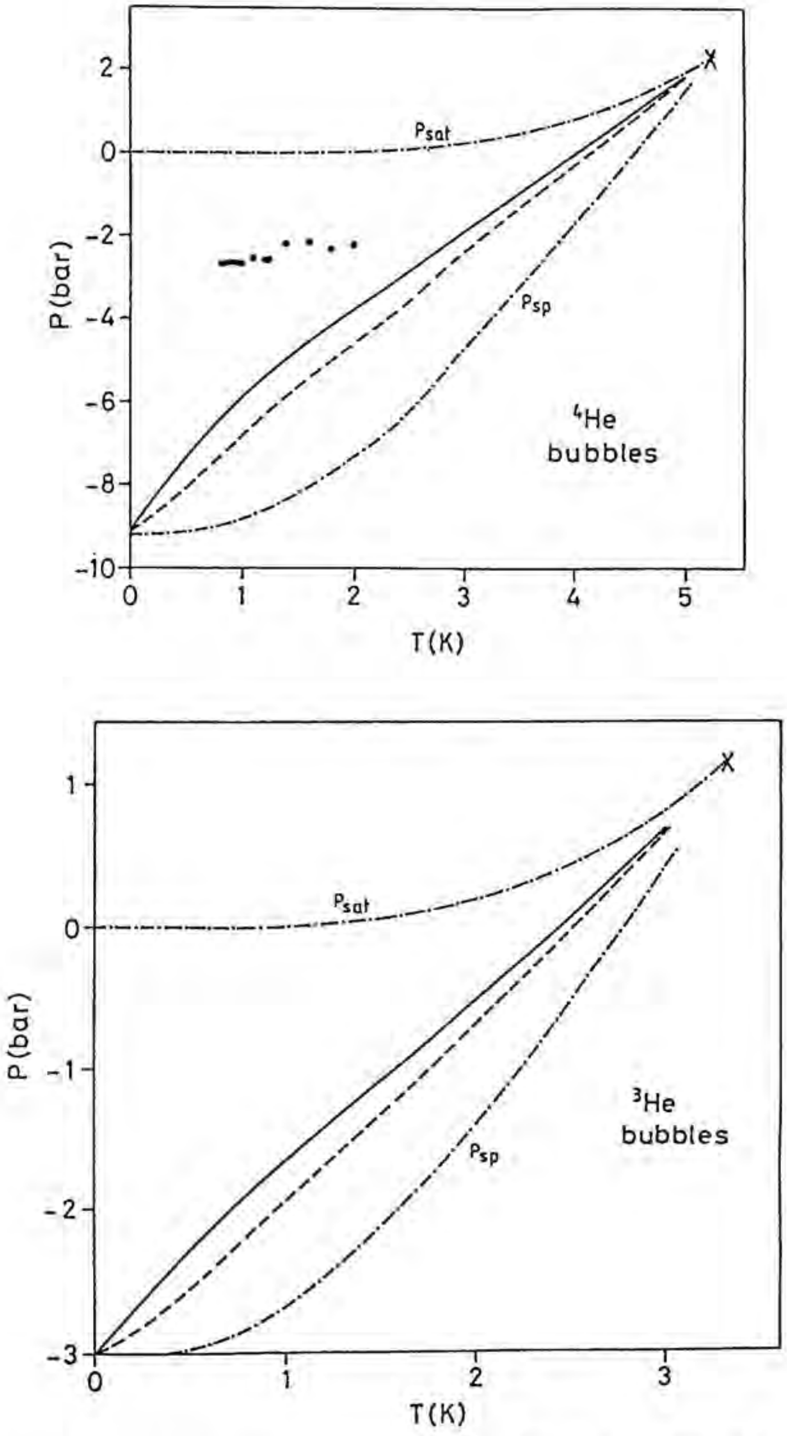

Figure 2.7. Homogeneous cavitation pressure for ^{4}He (a) and ^{3}He (b) as a function of temperature. The lines have the same meaning as in Figure 2.6. The dots in (a) are experimental points taken from [16].

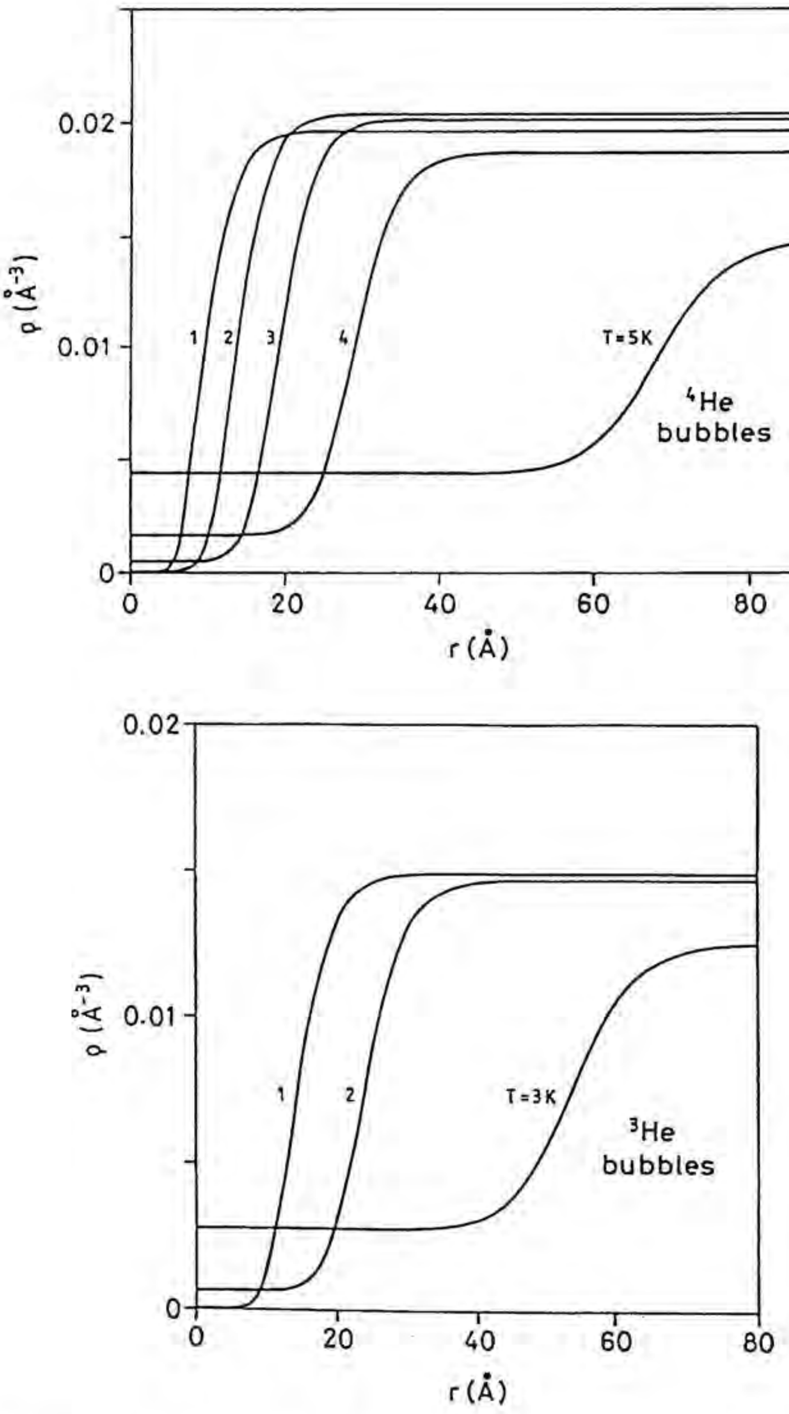

Figure 2.8. Critical bubbles for ^{4}He (a) and ^{3}He (b) at the indicated temperatures.

2.4 Nucleation

Figures 2.9 to 2.11 show the results for nucleation in both isotopes. In Fig. 2.9 we have plotted the nucleation barrier as a function of pressure calculated along different isotherms. The range of temperatures goes from zero to almost the critical temperature. Similarly to what has been previously indicated for bubble formation, one can see that $\Delta\Omega$ drops to zero at the pressure corresponding to the spinodal line, and diverges when it approaches the saturation value. Note the different behaviour of the barriers in nucleation and cavitation processes. It can be easily seen from the phase equilibrium diagram (Fig. 2.1), that in the metastability region of high densities, where cavitation occurs, $P_{sp} < P_{sat}$ and that they become closer at higher temperatures, whereas in the metastability region of low densities, where nucleation occurs, $P_{sp} > P_{sat}$ and become closer at lower temperatures. Thus at a given T, for increasing pressures in the range bounded by the corresponding saturation and spinodal pressures, in cavitation processes $\Delta\Omega$ is an increasing function and at high temperatures the curve is almost vertical, whereas in nucleation processes $\Delta\Omega$ is a decreasing function and its curve is almost vertical at low temperatures.

The pressure P_h of homogeneous droplet nucleation is shown in Fig. 2.10 as a function of T. The meaning of the curves is the same as in Fig. 2.6. Note that the difference between P_h and P_{sat} is rather small, of the order of 0.1 bar for ^{4}He above $T \sim 2$ K. and ~ 0.03 bar for ^{3}He above $T \sim 1$ K. This indicates that experiments aiming at studying homogeneous nucleation in helium will be much harder to analyze in the gas than in the liquid phase. We would also like to draw the attention on the negligible influence of the value of $(V\tau)_e$ on P_h.

Finally, in Fig. 2.11 the density profiles of the critical droplets we have found are plotted, for temperatures ranging from $T = 1$ to 5 K in ^{4}He [Fig. 2.11(a)] and for $T = 1$, 2, and 3 K in ^{3}He [Fig. 2.11(b)]. Again one can see that, due to the decrease of the surface tension, the critical droplets grow as T increases. Comparing Figs. 2.8 and 2.11, one can see that for each isotope, at given T the sizes of the critical drop and bubble are similar (see also [9]).

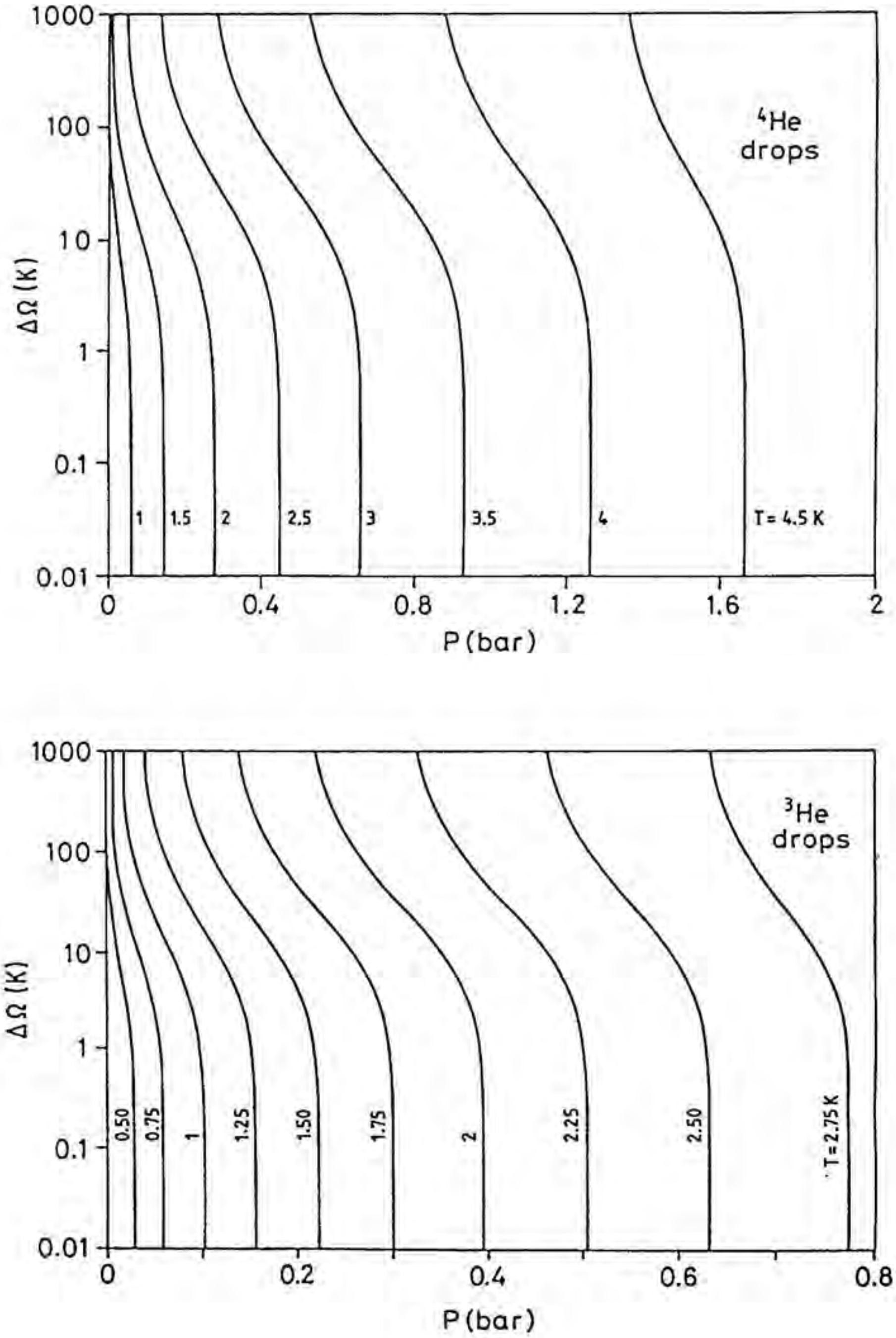

Figure 2.9. Nucleation barriers as a function of pressure for ^{4}He (a) and ^{3}He (b) corresponding to drop formation.

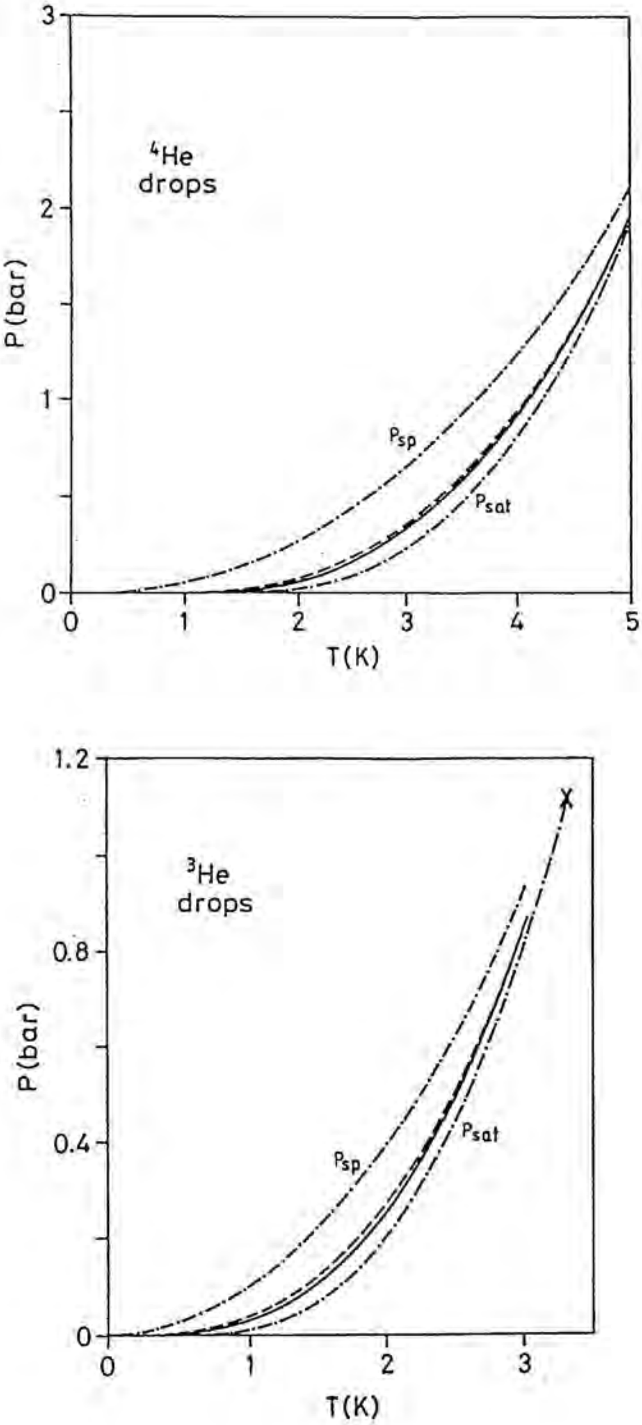

Figure 2.10. Homogeneous nucleation pressure as a function of temperature for ^{4}He (a) and ^{3}He (b). The lines have the same meaning as in Figure 2.6.

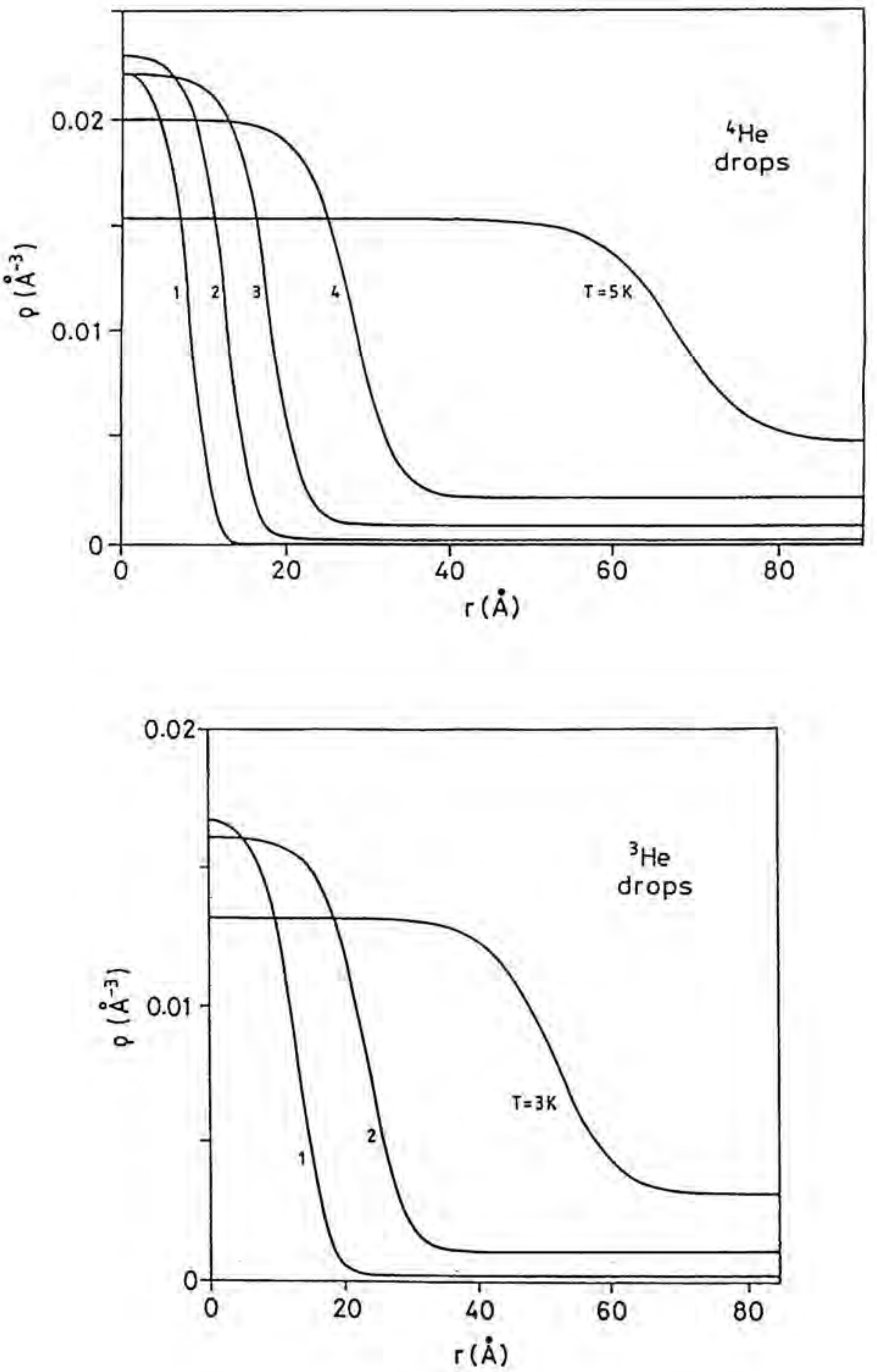

Figure 2.11. Critical drops for ^{4}He (a) and ^{3}He (b) at the indicated temperatures.

Chapter 3

Thermal nucleation and cavitation in ^{3}He-^{4}He mixtures

Thermal nucleation in binary mixtures is receiving much attention [10, 30] due to its importance in technical applications. Similar to the case of one-component systems, the frame for the theoretical understanding of this phenomenon has been provided for a long time by the classical nucleation theory. It makes use of the capillarity approximation, in which the free energy of a sharp-surface nucleus is written as the sum of a bulk and a surface term. Although this description can be safely used near the saturation line, it is certainly incorrect near the spinodal line, because here it predicts a non-vanishing nucleation barrier. The density functional approach overcomes the shortcomings inherent in the capillarity approximation; moreover, it has been shown [31] that the effects of surface enrichment and curvature are also naturally included in this approach.

Liquid helium at low temperatures has been considered as an useful tool for testing homogeneous nucleation theories [10], mainly because near the absolute zero temperature it can be prepared with a high degree of purity. However, Helium is usually a mixture of ^{3}He and ^{4}He, and the aim of the present chapter is to complete these studies considering the case of mixtures.

It is well known that at low temperature, even when small amounts of ^{3}He are present in ^{4}He, the surface tension of the liquid is considerably reduced. This is due to the presence of ^{3}He atomic levels at the free surface of liquid ^{4}He, which are referred to as Andreev states [32]. As we have already seen in the previous chapter, the cavitation barrier strongly depends on surface tension, and thus bubble formation is enhanced even at very low ^{3}He concentrations. Therefore, a sizeable change in the cavitation pressure with respect to that of the pure system should be observed in mixtures below saturation. A lower bound to the minimum pressure a solution of ^{3}He in ^{4}He can attain as a metastable system is estimated. At this pressure, the probability of forming a critical bubble is high and the system is likely to split into two phases.

A density functional for homogeneous ^{3}He-^{4}He mixtures at zero temperature has been constructed by Dalfovo and Stringari [33, 34], the parameters of which have been adjusted so as to reproduce some experimental data of pure ^{3}He and ^{4}He systems, and of the mixture. We have employed the same functional, slightly modifying the surface parameters to better fit the experimental surface tension of pure ^{4}He and that of the mixture-pure ^{3}He interface at saturation.

We have used the density functional approach to investigate thermal cavitation and nucleation in ^{3}He-^{4}He liquid mixtures at low temperatures, at different pressures (P) and ^{3}He concentrations (x) in the metastable region of the phase diagram. Due to the miscibility gap existing in ^{3}He-^{4}He mixtures, an interesting process appears. For ^{3}He concentrations above saturation, it is also possible, even at negative pressures, that phase separation originates by nucleation of ^{3}He *drops* in the mixture (hereafter referred to as drop formation). Therefore, two nucleation mechanisms are present at negative pressures: drop and bubble formation, competing somewhere in the pressure-^{3}He concentration plane. In both cases, there is a critical nucleation cluster size above which the system will undergo phase separation. The associated free energy defines the barrier height that determines which of these processes is more probable.

It is worth emphasizing that both drop and bubble profiles are naturally obtained in this approach. This is especially useful in multi-component systems, where the shape of the nucleation cluster configuration cannot be easily guessed. Using the density functional, calculations of the barrier height are performed as a function of pressure and ^{3}He concentration, which enable us to obtain the homogeneous cavitation pressure via thermal activation.

Recent experiments [35] at low temperature and low positive pressures have found metastable supersaturated ^{3}He-^{4}He solutions only up to a ^{3}He concentration around 7%. These results are in contradiction with the common belief that a supersaturated mixture at low T could be in a metastable state up to $\sim 16\%$.

We have investigated the phase separation at low positive pressures in supersaturated ^{3}He-^{4}He liquid mixtures. We have found a large discrepancy in the supersaturation value between recent experiments ($\sim 1\%$) and nucleation theory ($\sim 10\%$). We suggest that the rather small degree of supersaturation found experimentally is due to destabilization of vortices with cores rich in ^{3}He.

This chapter is structured as follows. In section 3.1 we analyze the homogeneous system to determine the boundaries between the metastable (where cavitation takes place) and the stable and unstable regions [36]. In section 3.2 we consider the inhomogeneous system, fixing the functional parameters to correctly fit the experimental surface tension of the ^{4}He liquid free surface and of the mixture at saturation [36]. We also calculate, as a function of ^{3}He concentration, the surface tension of the free surface of the mixture [36], which is relevant for bubble formation, and the surface tension of the pure ^{3}He-mixture interface along the saturation curve [37], experimentally known only at $P = 0$. In section 3.3 we consider cavitation at negative pressures in mixtures at ^{3}He concentrations below saturation [36] and in section 3.4 we study cavitation and nucleation at negative pressures in mixtures above saturation [37]. Finally, in section 3.5 we study the critical supersaturation [38].

3.1 The metastability region

The following free energy density for a mixture of ^{3}He and ^{4}He has been used [34]:

$$f = f_v + \frac{\hbar^2}{2m_4}\tau_4 + \frac{\hbar^2}{2m_3^*}\tau_{3s} + d_4(\vec{\nabla}\rho_4)^2 + d_3(\vec{\nabla}\rho_3)^2 + d_{34}(\vec{\nabla}\rho_3 \cdot \vec{\nabla}\rho_4) \tag{3.1}$$

with

$$\begin{aligned} f_v &= \frac{1}{2}b_4\rho_4^2 + \frac{1}{2}c_4\rho_4^2\rho^{\gamma_4} \\ &+ \frac{\hbar^2}{2m_3^*}\tau_{3v} + \frac{1}{2}b_3\rho_3^2 + \frac{1}{2}c_3'\rho_3^2\rho^{\gamma_3} + \frac{1}{2}c_3''\rho_3^{2+\gamma_3} \\ &+ b_{34}\rho_3\rho_4 + c_{34}\rho_3\rho_4\rho^{\gamma_{34}} , \end{aligned} \tag{3.2}$$

where ρ_i is the particle density of the ^{i}He isotope, ρ is the total density $\rho = \rho_3+\rho_4$, and τ_i and m_i are the corresponding kinetic energy densities and atomic masses, respectively. The ^{3}He effective mass is defined as

$$m_3^* = m_3\left(1 - \frac{\rho_3}{\rho_{3c}} - \frac{\rho_4}{\rho_{4c}}\right)^{-2} \tag{3.3}$$

and the kinetic energy densities are

$$\tau_4 = \frac{1}{4}\frac{(\nabla\rho_4)^2}{\rho_4} \tag{3.4}$$

and

$$\tau_3 = \tau_{3v} + \tau_{3s}\,, \tag{3.5}$$

where

$$\begin{aligned} \tau_{3v} &= \frac{3}{5}(3\pi^2)^{2/3}\rho_3^{5/3} \\ \tau_{3s} &= \frac{1}{18}\frac{(\nabla\rho_3)^2}{\rho_3} + \frac{1}{3}\Delta\rho_3 \end{aligned} \tag{3.6}$$

We have considered that ^{3}He is in the normal phase and consequently, by "zero temperature" we shall always mean a temperature around 3 mK. Let us first consider a homogeneous mixture, in which the density gradient terms vanish and f reduces to f_v. The parameters $b_4, c_4, \gamma_4, b_3, \gamma_3, \rho_{3c}$ and the sum $c_3' + c_3''$ have been adjusted [34] so as to reproduce various physical quantities at saturation for pure ^{4}He and ^{3}He homogeneous systems, such as the energy per particle, the density, the compressibility and the ^{3}He effective mass. The parameters b_{34}, c_{34} and c_3'' have been fixed in order to reproduce the maximum solubility of ^{3}He in ^{4}He at zero pressure (x_0), the ^{3}He chemical potential when $\rho_3 \to 0$ and the ratio of specific heats between ^{3}He and ^{4}He at the same limit. The parameter ρ_{4c} has been fixed to take into account the variation of m_3^* with ^{3}He concentration, and γ_{34} has been taken as an average between γ_3 and γ_4 [34].

Before studying cavitation, it is convenient to delimit the metastable region where nucleation occurs. At zero temperature, we determine its boundaries with the stable and unstable regions in the plane (P, x), where P is the pressure and x is the ^{3}He concentration ($x = \rho_3/\rho$). Necessary and sufficient stability conditions for a binary system [30, 39] are given by the following inequalities on the compressibility

$$K = \left(\frac{\partial P}{\partial \rho}\right)_x \geq 0 \tag{3.7}$$

and the chemical potentials:

$$\left(\frac{\partial\mu_4}{\partial x}\right)_P \leq 0 \text{ or } \left(\frac{\partial\mu_3}{\partial x}\right)_P \geq 0 \,. \tag{3.8}$$

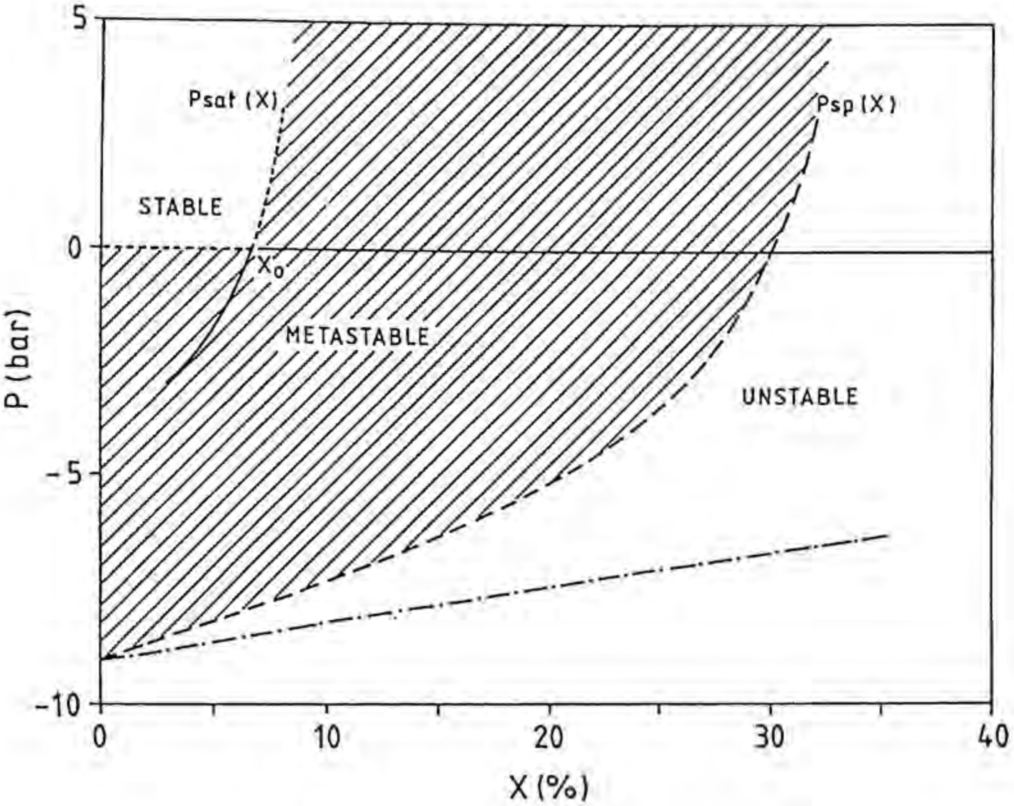

Figure 3.1. Phase diagram of the mixture at $T = 0$.

A positive compressibility guarantees mechanical stability, whereas the condition on the chemical potentials ensures diffusive stability. Taken as equalities, the above equations determine two curves on the (P, x) plane, which are shown in figure 3.1 as a dashed-dotted and a dashed line, respectively. One can see in this figure that, for the functional we are using, the diffusive stability condition is always violated first, so inequality (3.7) is in practice useless for this problem. Therefore, the spinodal line, which is the boundary between the metastable and the unstable regions, is fixed by the diffusive stability condition. This line will be denoted $P_{sp}(x)$. At $P = 0$, it cuts the x-axis at $x_{sp} \sim 30\%$.

Comparison of x_{sp} with the maximum value of x, for which the mixture has been experimentally found in a metastable homogeneous state $x_h \simeq 15\%$* [42], can be considered as being rather dubious. This would mean that one is identifying the spinodal pressure with the homogeneous nucleation pressure, which is the only one that is experimentally accessible. As a matter of fact, these pressures can be quite different [13, 16, 27]. In the present case the functional has been fixed to reproduce x_0 [34], yielding an x_{sp} value above the experimental x_h at $P = 0$. The variational calculations of Ref. [43] yield $x_0 = 1\%$ instead of the experimental value $x_0 \sim 6.5\%$ [42], and $x_{sp} = 18\%$, whereas those of Ref. [44] yield $x_{sp} \sim 10\%$.

To draw the frontier between the metastable and the stable region let us first consider the maximum concentration curve which is determined by the two-phase equilibrium equations:

$$P(\rho, x) = P(\rho_{3p}, x = 1) \tag{3.9}$$

and

$$\mu_3(\rho, x) = \mu_3(\rho_{3p}, x = 1) \tag{3.10}$$

where ρ_{3p} is the density of segregated ^{3}He. These equations determine a curve on the (P, x) plane which is denoted as $P_{sat}(x)$ in figure 3.1. It is interesting to note that eqs. (3.9) and (3.10) have solutions at negative pressures. $P_{sat}(x)$ is interrupted at the ^{3}He spinodal pressure [21], as for lower pressures the above equations are meaningless. In the phase diagram (Fig. 3.1) one can distinguish two kind of metastabilities:

- At a given pressure P, for concentrations larger than those defined by the equation $P = P_{sat}(x)$, the single-phase system is metastable because the two-phase system (pure ^{3}He and a saturated mixture) has a lower free energy, where the formation of critical ^{3}He drops is important as they are responsible for phase separation.

---

*Recent experiments [35] and [40] as quoted in [41], have actually found metastable ^{3}He-^{4}He solutions up to smaller concentrations ($x_h \sim 7\%$). We defer this discussion to Sec. 3.6.

- Another metastability arises from the application of a tensile strength. In this case, the system will develop either a free surface for low concentrations, or ^{3}He will segregate and also produce a mixture-pure ^{3}He interface. In the first case, phase separation will proceed by bubble nucleation, and in the second case by ^{3}He drop nucleation.

Finally, the boundary between the metastable and the stable regions is determined by the line $P = 0$ from $x = 0$ up to x_{sat} (which we shall call x_0), and the curve $P_{sat}(x)$ for $x > x_0$. We have indicated it by the the short-dashed line in figure 3.1. The metastable zone is the hatched region in this figure.

3.2 Inhomogeneous system: Surface tension

To analyze the properties of the inhomogeneous system, the full free energy density in Eq. (3.1) has to be considered. The parameters d_3, d_4 and d_{34} have been determined by fitting the experimental surface tensions. Our values [36] differ slightly from those of Ref. [34], since we have tried to reproduce the experimental data of [45, 46] instead of those of [47] used by Dalfovo [34].

Liquid helium mixtures at equilibrium may develop two kind of interfaces. One corresponds to the liquid free surface, and it appears at $P = 0$ when $x < x_0$. The other one appears when ^{3}He segregates for $x \geq x_0$ and $P \geq 0$, forming a pure ^{3}He-mixture interface. Different surface tensions are associated with these interfaces.

To calculate the surface tension of the liquid helium mixture interface, one has first to calculate the density profiles $\rho_3(z)$ and $\rho_4(z)$ of the equilibrium configuration. The density profiles are obtained by solving the coupled Euler-Lagrange (EL) equations:

$$\frac{\delta f}{\delta \rho_3} = \frac{\partial f}{\partial \rho_3} - \nabla \frac{\partial f}{\partial(\nabla \rho_3)} = \mu_3 \tag{3.11}$$

and

$$\frac{\delta f}{\delta \rho_4} = \frac{\partial f}{\partial \rho_4} - \nabla \frac{\partial f}{\partial(\nabla \rho_4)} = \mu_4 \tag{3.12}$$

where $f(\rho_3, \rho_4)$ is the free energy of the system and μ_3, μ_4 are the corresponding ^{3}He and ^{4}He chemical potentials.

The surface tension is calculated as

$$\sigma = \int_{-\infty}^{\infty} \Big[f(z) - \mu_3\rho_3(z) - \mu_4\rho_4(z) + P\Big] \mathrm{d}z \equiv \int_{-\infty}^{\infty} \Big(P - p(z)\Big) \mathrm{d}z \,, \tag{3.13}$$

where P is the equilibrium pressure $P = p(z \to \pm\infty)$. Dalfovo [34] has calculated the surface tension between pure ^{3}He and the saturated mixture using a family of Wood-Saxon densities by fixing the parameter d_{34} to the value of $d_3 + d_4$. In particular, for $P = 0$ a value of $\sigma = 0.026$ KÅ^{-2} was obtained, while extrapolation of the experimental values yields around 0.016 KÅ^{-2} [47].

The EL equations have been solved for $x = x_0$. The boundary conditions for $z \to \pm\infty$ are obtained by solving the two-phase equilibrium conditions (3.9) and (3.10). The value of the parameter d_{34} has been varied so as to reproduce as well as possible the experimental surface tension of the mixture-pure ^{3}He interface at $P = 0$. The best result obtained for σ is 0.018 KÅ^{-2}, and the full set of parameters defining the functional is given in Table I of Ref. [36].

3.2.1 Free surface

For $x < x_0$ at $P = 0$, the density profiles $\rho_3(z)$ and $\rho_4(z)$ are obtained by solving the coupled EL equations (3.11) and (3.12). Imposing the following boundary conditions. When $z \to -\infty$ the densities tend to zero, and when $z \to +\infty$ the densities tend to values of ρ_3 and ρ_4 such that $P(\rho_3, \rho_4) = 0$ and $x = \rho_3/(\rho_3 + \rho_4)$.

We have calculated the surface tension $\sigma(x)$ pertaining to the free surface of the mixture, which is the one relevant in classical cavitation theories. In Fig. 3.2 we show it as a function of concentration. One can see that σ decreases abruptly near $x = 0$ (for pure ^{4}He, the surface tension is 0.256 KÅ^{-2}). It is related to the presence of a finite surface density (N_s) of ^{3}He atoms at the interface. It is shown in Fig. 3.3(a), where the density profile for $x = 0.05\%$ is plotted. This fact was predicted by Andreev [32] as a sign of the existence of ^{3}He surface states with larger binding energy than those of a ^{3}He atom in the ^{4}He liquid bulk.

In a recent work, Pavloff and Treiner [48] have studied, using the original functional of Ref. [34], the properties of the two-dimensional system formed by ^{3}He atoms on the surface of liquid ^{4}He as a function of the ^{3}He coverage N_s. They find several types of surface states accessible to ^{3}He atoms and calculate the variation of the surface tension as a function of N_s. We have repeated this calculation and found similar results (remember we are using a different parameter set), which are shown in the upper right-hand corner of Fig. 3.2. The last N_s of this graph (N_s=0.095Å^{-2}) roughly corresponds to the first calculation in x ($x = 0.05\%$) in the sense that both yield very similar ^{3}He density profiles at the surface.

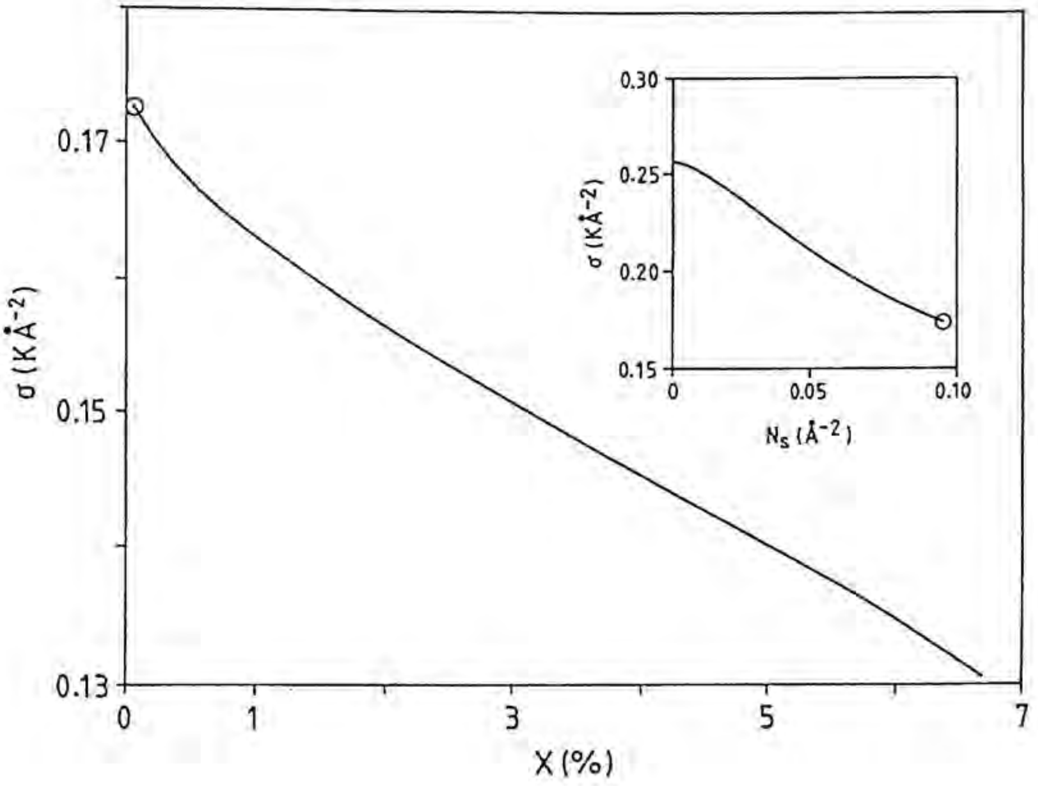

Figure 3.2. Surface tension σ plotted as a function of the ^{3}He concentration x. In the upper right-hand corner we show σ as a function of the ^{3}He surface density N_s. The configuration corresponding to the final value of $N_s(0.095\text{Å}^{-2})$ and to the first value of $x(0.05\%)$ are approximately equivalent, both yielding $\sigma = 0.172$ KÅ^{-2}.

For increasing values of x, the maximum of ρ_3 at the surface smoothly increases until it reaches its equilibrium value (see Fig. 3.3). As one would expect, when x approaches the calculated saturation value $x_0 = 6.6\%$ at $P = 0$, the so-called Antonov rule [46] holds, i.e.:

$$\sigma = \sigma_3 + \sigma_i \,, \tag{3.14}$$

where σ, σ_3, and σ_i, are the surface tensions of the free liquid mixture at saturation, of pure liquid ^{3}He and of the interface between pure liquid ^{3}He and the saturated mixture, respectively. The numerical values of these quantities for $x = 6.6\%$ are 0.131, 0.113 and 0.018KÅ^{-2}, thus perfectly fulfilling the above relation. The corresponding density profile is shown in Fig. 3.3(c).

For $x \geq x_0$, in accordance with experiment [49], no solution to Eqs. (3.11), (3.12) exists: it is impossible to observe a supersaturated mixture with a liquid free surface, since the exceeding ^{3}He segregates to the surface.

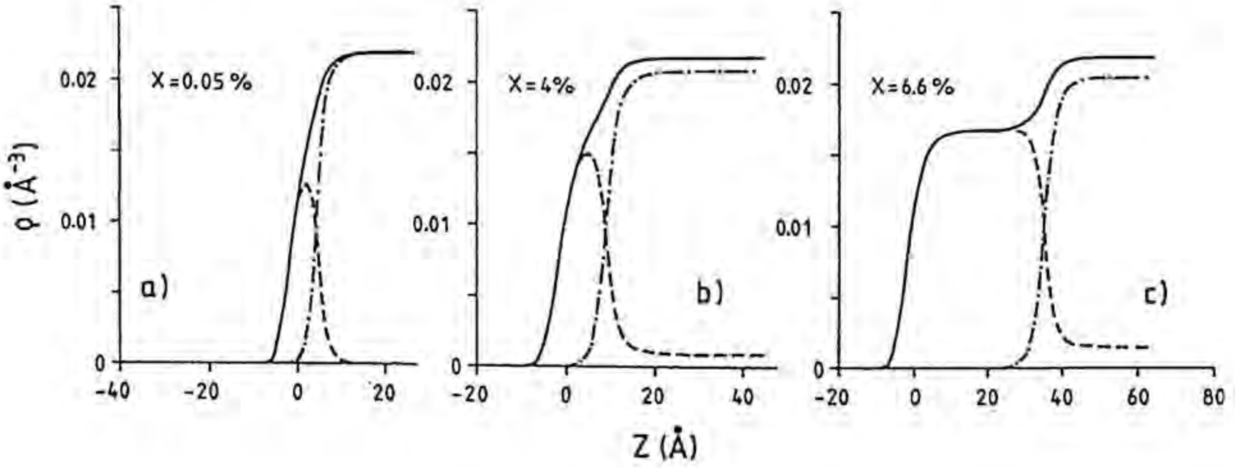

Figure 3.3. Liquid free surface density profiles as a function of z for different ^{3}He concentrations: a) $x = 0.05\%$, b) $x = 4\%$, and c) $x = 6.6\%$. Dashed lines correspond to ^{3}He, dashed-dotted lines to ^{4}He, and solid lines to the total density of the mixture ($z = 0$ is defined as the point where $\rho = \rho_{sat}/2$).

3.2.2 Pure ^{3}He-mixture interface

The surface tension of the mixture free surface has been studied in the previous subsection as a function of x. We now proceed to obtain that of the mixture-pure ^{3}He interface along the saturation curve, which is the relevant one for ^{3}He drop formation. The saturation curve $P_{sat}(x)$, i.e., the maximum solubility curve, is determined by the two-phase equilibrium conditions given by Eqs. (3.9) and (3.10).

The calculation follows a similar line as for the free surface case. Given a point (x, P) on the saturation curve the ^{3}He and ^{4}He particle density profiles $\rho_3(z)$ and $\rho_4(z)$ are obtained by solving the coupled Euler-Lagrange equations (3.11) and (3.12), imposing the following boundary conditions. When $z \to \infty$ the densities $\rho_3(z)$ and $\rho_4(z)$ tend to values ρ_3 and ρ_4 such that $x = \rho_3/(\rho_3 + \rho_4)$ and $\rho^2\, \partial f/\partial\rho|_x = P$. When $z \to -\infty$ only pure ^{3}He at pressure P is present.

The surface tension of the pure ^{3}He-mixture interface, calculated as Eq. (3.13), is displayed in Fig. 3.4 as a function of x. We have started at x =4 %, which corresponds to a pressure close to the spinodal pressure of pure ^{3}He, and have stopped the calculations at a value of x which roughly corresponds to +3 atm. Above that value, the functional does not accurately reproduce the maximum ^{3}He solubility, see [34]. Comparing the present results with those shown in Fig. 3.2, one can see that the surface tension of the mixture-pure ^{3}He interface is a factor of ten smaller than that of the mixture free surface.

3.3 Nucleation and cavitation within the DF approach

In this section we are interested in nucleation and cavitation processes in ^{3}He-^{4}He mixtures. Because of the miscibility gap existing in ^{3}He-^{4}He mixtures, and the presence of ^{3}He atomic levels at the free surface of ^{4}He, these processes will provide a large variety of critical configurations which can be more intricate than the critical clusters we have obtained in pure ^{3}He and pure ^{4}He (chapter 2). However, since the density functional approach makes no assumption on density profiles, the same procedure as in the pure case is valid to calculate the homogeneous nucleation pressure. Now all the magnitudes depend on $\rho_3(r)$ and $\rho_4(r)$ simultaneously, which are obtained minimizing

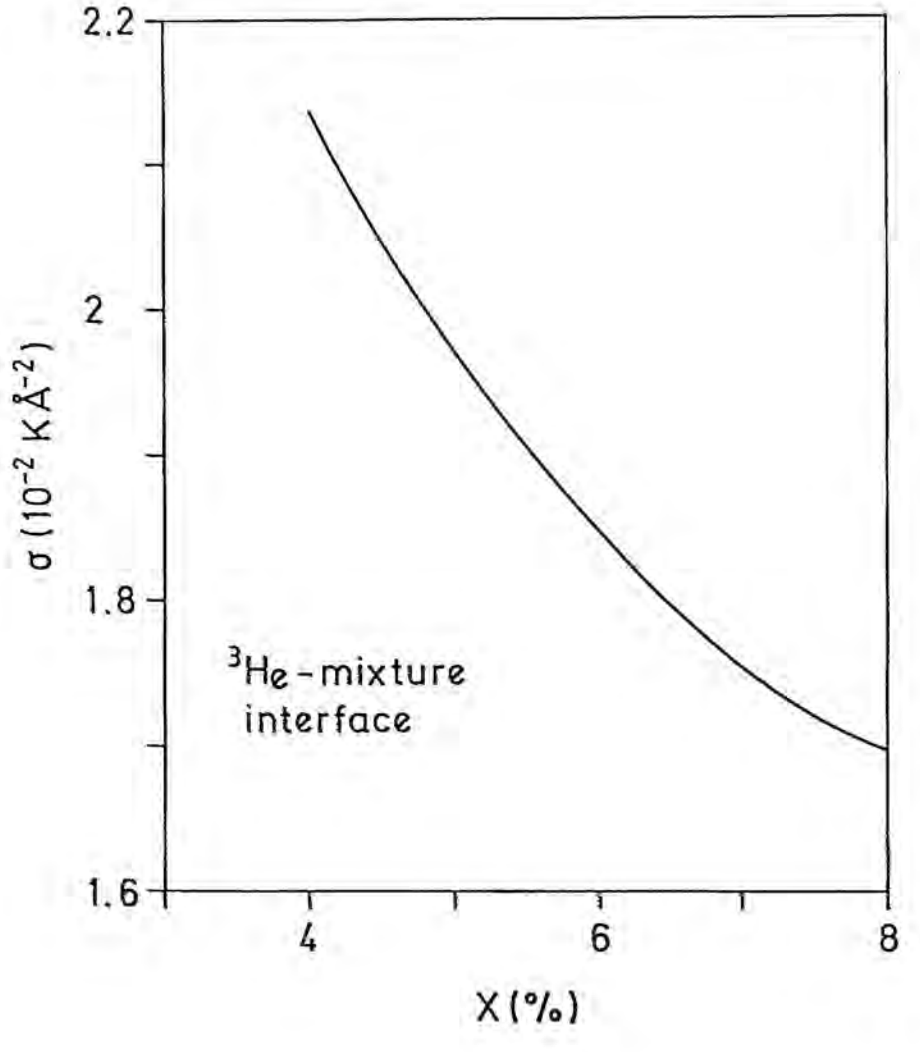

Figure 3.4. Surface tension of the mixture-pure ^{3}He interface as a function of the ^{3}He concentration along the saturation curve.

the free energy density functional $f(\rho_3, \rho_4)$ of the mixture. The density profile $\rho(r)$ of the critical cluster is then $\rho(r) = \rho_3(r) + \rho_4(r)$. Let us briefly recall the method we have already used in the previous chapter for isotopically pure helium and that we want to extent to the case of ^{3}He-^{4}He mixtures.

- The starting point is the free energy density functional $f(\rho_3, \rho_4)$, Eq. (3.1), which describes the ^{3}He-^{4}He mixture at $T = 0$.

- Given a metastability configuration (x,P) with uniform density $\rho_m = \rho_{3m} + \rho_{4m}$, we calculate the particle density profiles $\rho_3(r)$ and $\rho_4(r)$ for the critical nucleus, by solving the coupled EL equations (3.11) and (3.12) in spherical coordinates, where $\mu_{3(4)}$ are the corresponding chemical potentials in the homogeneous metastable system. The boundary conditions are that the r-derivative of $\rho_{3(4)}$ at $r = 0$ is zero and that $\rho_{3(4)}(r \to \infty)$ approaches the corresponding density of the metastable system $\rho_{3m(4m)}$.

  The density profile of the critical cluster is then $\rho(r) = \rho_3(r) + \rho_4(r)$. It is such that with any further increase in size, it may continue to grow without any external intervention and trigger the phase separation.

- The nucleation barrier height $\Delta\Omega$ is determined by the free energy of the critical nucleus. It is obtained from the difference between the grand potential of the critical cluster and that of the homogeneous metastable state:

  $$\Delta\Omega = \int d\mathbf{r}\Big(f(\rho_3, \rho_4) - f_v(\rho_{3m}, \rho_{4m}) - \mu_3(\rho_3 - \rho_{3m}) - \mu_4(\rho_4 - \rho_{4m})\Big). \quad (3.15)$$

  Remember that since the metastable system is homogeneous,

  $$P = -f_v(\rho_{3m}, \rho_{4m}) + \mu_3\rho_{3m} + \mu_4\rho_{4m}. \quad (3.16)$$

- The nucleation rate, i.e., the number of clusters formed in the homogeneous system per unit of time and of volume due to thermal fluctuations is given by

  $$J_T = J_{0T} \exp^{-\Delta\Omega/kT}, \quad (3.17)$$

  where k is Boltzmann's constant and the pre-exponential factor J_{0T} depends on the dynamics of the cavitation process (see Sec. 2.1.3). We have calculated $\Delta\Omega$ with a density functional description of the mixture at $T = 0$. Strictly speaking, one should calculate $\Delta\Omega$ as a function of T. However, for the low temperatures we are considering, no appreciable modifications in the density functional are expected to arise. It is important to recall that the solubility of ^{3}He in ^{4}He drastically increases with T, and has important consequences on $\sigma(x)$. Since the coefficients of the functional (3.1) have been adjusted at $T = 0$, from the analysis of the available experimental data [50] at low temperatures, we estimate that the present calculations are reliable up to $T \simeq 150\,\mathrm{mK}$.

- To make a quantitative estimate of the homogeneous cavitation pressure P_h. one may proceed as in the pure case, that is, consider that to observe cavitation one must have

  $$J_T \cdot (V\tau)_e \sim 1 \qquad (3.18)$$

  where $(V\tau)_e$ are the experimental volume and time, and then solve the equation

  $$\frac{\Delta\Omega}{kT} = \ln\left[J_{0T} \cdot (V\tau)_e\right]. \qquad (3.19)$$

It is worth mentioning two new aspects appearing in the case of He mixtures which are absent in the case of pure liquid He. First, in the metastable $P < 0$ region not only bubbles, but also ^{3}He droplets may be formed. Second, the P-dependence of $\Delta\Omega$ for ^{3}He drops being formed in the mixture is different from that for bubbles. At a given x, both barriers vanish at the same pressure where the homogeneous system becomes unstable, i.e., at the spinodal pressure $P_{sp}(x)$. But they diverge at different pressures, since the pressures at which the system is stable against bubble- or drop-formation are different. In the case of bubbles, at a given x the barrier $\Delta\Omega$ diverges when P goes to zero and, in the case of drops, at a given concentration $\Delta\Omega$ diverges at the negative P obtained when one solves the equilibrium conditions (3.9) and (3.10). These facts are originated by the limited solubility of ^{3}He in ^{4}He liquid at $T \sim 0\,\mathrm{K}$. In view of the two types of metastabilities we have already distinguish in the mixture phase diagram (Sec. 3.1), we shall study cavitation and nucleation at low temperatures and negative pressures first in mixtures below saturation, and next, above saturation. Finally, we shall study the critical supersaturation of ^{3}He-^{4}He mixtures at low temperatures.

As a first approximation, one can consider drop and bubble nucleation in the capillarity model. Since we have calculated the surface tension of the pure ^{3}He-mixture interface along the saturation curve (Fig. 3.4), which is a key ingredient in the capillarity model and experimentally known only at $P = 0$, for the sake of completeness let us recall the capillarity approximation to bubble and drop formation in ^{3}He-^{4}He mixtures.

3.3.1 Capillarity model

To have a rough idea on drop and bubble nucleation processes, it is convenient to start from the simplest capillarity model. In this approach clusters are assumed to have a sharp radius, thus the nucleation barrier is written as a balance between surface and volume terms [26]

$$\Delta U(R) = SR^2 - VR^3 \tag{3.20}$$

where R is the radius of the nucleation cluster. There are two possible processes, bubble and drop formation. Depending on the metastability configuration, one process will be more favorable than the other.

i. Bubble formation,

$$\begin{aligned} S &= 4\pi\sigma_B \,, \\ V &= \frac{4\pi}{3}\Delta P \,, \end{aligned} \tag{3.21}$$

where σ_B refers to the surface tension of the mixture *free* surface (Fig. 3.2), and ΔP is the pressure difference between the bubble and the bulk. It is assumed that the density inside the bubble is zero, so that $\Delta P = -P$ (remind that P is a negative quantity).

ii. Drop formation [51, 52],

$$\begin{aligned} S &= 4\pi\sigma_D \,, \\ V &= \frac{4\pi}{3}\Delta\mu_3\rho_3 \,, \end{aligned} \tag{3.22}$$

where σ_D refers to the surface tension of the mixture-*pure* ^{3}He interface (Fig. 3.4), $\Delta\mu_3$ is the difference between the chemical potential of ^{3}He in the mixture and of pure ^{3}He at the same pressure, and ρ_3 is the ^{3}He particle density in the pure phase. For ^{3}He-^{4}He mixtures, the capillarity approach cannot describe drops at pressures below the spinodal one of pure ^{3}He (about -3 atm [13, 21]).

The barrier height is determined by the maximum value of $\Delta U(R)$, which occurs at a size $R_c = 2S/3V$, and is equal to

$$\Delta U(R_c) = \frac{4}{27}\frac{S^3}{V^2} \,. \tag{3.23}$$

Substituting (3.22) and (3.23) in $\Delta U(R_c)$, we obtain the energy barrier in the capillarity approximation for bubble (B) and drop (D) formation:

$$\Delta U(R_c)_B = \frac{16\pi}{3} \frac{\sigma_B^3}{(\Delta P)^2} , \tag{3.24}$$

$$\Delta U(R_c)_D = \frac{16\pi}{3} \frac{\sigma_D^3}{(\Delta\mu_3 \rho_3)^2} . \tag{3.25}$$

The maximum heights diverge at $\Delta P = 0$ for bubbles, and at $\Delta\mu_3 = 0$ for drops, which correspond to the respective saturation curves.

Neglecting prefactors entering the nucleation rate definition (see Sec. 3.3), at a given temperature, bubble and drop configurations have the same probability of being formed when the nucleation barrier maxima become equal. This equality defines a transition pressure P_t

$$|P_t| = \Delta\mu_3 \ \rho_3 \ \left(\frac{\sigma_B}{\sigma_D}\right)^{3/2} . \tag{3.26}$$

This equation implicitly defines a curve in the (P, x) plane. On the right of this line, drops rather than bubbles are formed, and the contrary happens on the left. To make a quantitative prediction the surface tension values are needed. We recall that we have obtained these values from a density functional calculation (see Sec. 3.2), and defer the discussion to section 3.5.

3.4 Cavitation in mixtures below saturation and at negative pressures

The case we are interested in is that of a liquid mixture below saturation ($x < x_0$) submitted to a tensile strength in which bubbles are formed. The mixture will develop a free surface and, as we have seen in Sec. 3.2.1, due to the presence of Andreev states ^{3}He atoms will locate at the ^{4}He surface. Thus, even when small amounts of ^{3}He are solved in ^{4}He the bubble-like mixture configuration will have a lower surface tension than the free ^{4}He surface ($\sigma(x) < \sigma(0)$). The strong dependence of the energy barrier height on the surface tension, which is clearly shown in the capillarity model (3.24), suggests that nucleation is enhanced when ^{3}He is solved in ^{4}He due to the decrease of σ, which we have already calculated as a function of ^{3}He concentration in Sec. 3.2.

The lowering of the energy barrier will decrease the tensile strength, moving it away from the spinodal pressure.

To obtain an estimate of the relative departure between spinodal and nucleation pressures at $x = 0$ and at any other x-value, we can use the barrier height approximation near the spinodal given by Lifshitz and Kagan [26] whose dependence on P and σ through x is:

$$\Delta U(R_c) \sim \sigma^3(x)\,(P(x) - P_{sp}(x))^{3/4}\,. \tag{3.27}$$

Solving Eq. (3.19) with $\Delta U(R_c)$ instead of $\Delta\Omega$ for both concentrations at the same temperature and taking the quotient we obtain

$$\frac{P_h(x) - P_{sp}(x)}{P_h(0) - P_{sp}(0)} \simeq \left(\frac{\sigma(0)}{\sigma(x)}\right)^4 . \tag{3.28}$$

Since $\sigma(x)$ changes sizeably even at very low concentration, the cavitation pressure will differ appreciably from that of pure ^{4}He. For example, this ratio is 4.5 for $x = 10^{-4}\%$ and 6 for $x = 1\%$. This means that at the same temperature, the cavitation pressure for $x = 10^{-4}\%$ (1%) is 4.5 (6) times farther away from the spinodal pressure than for pure ^{4}He.

One estimate of the cavitation pressure near the saturation can be obtained in the capillarity approximation (Sec. 3.3.1). However, as has been already discussed by Xiong and Maris [12], the approximations for calculating the barrier height near saturation (3.24) and near the spinodal (3.27) cannot be interpolated in a natural way, and a more accurate treatment is needed to describe cavitation throughout the pressure range. We have used the density functional approach which is based on a formalism proposed earlier by Cahn and Hilliard [53, 54], and later developed by various authors [12, 27, 31]. The basic procedure has been already pointed out in the previous section.

Given an homogeneous metastable state (x, P), we find the corresponding critical density profiles and the energy required to nucleate the critical configuration. The nucleation barrier height $\Delta\Omega$ is obtained from the difference between the grand potential of the critical cluster and that of the homogeneous metastable state (3.15).

In figure 3.5 we have plotted these barriers as a function of P for several ^{3}He concentrations, which correspond to bubble formation. Their P-dependence is as expected [12, 13, 27]: $\Delta\Omega$ diverges when P goes to zero (not shown in Fig. 3.5), and drops to zero at the corresponding spinodal pressure. Actually, solving the EL equations for $x \lesssim x_0$ and $P \lesssim 0$ we have also found ^{3}He-drop configurations. As is expected, the barriers for nucleating bubbles are smaller. Thus in this metastability region bubbles are likely to be formed, but at higher concentrations their barriers are higher, being then ^{3}He drop configurations more likely formed.

Figure 3.5 clearly shows the effect on $\Delta\Omega$ of increasing the ^{3}He concentration, and thus on the nucleation rate. Due to the lowering of the surface tension with increasing ^{3}He concentration (see Fig. 3.2), the surface energy required to form the interface decreases and so does the energy barrier. Then, cavitation is more likely to occur. Note that even concentrations as small as 10^{-4} % (recall commercial helium contains about 1.4×10^{-4} % of ^{3}He) cause a sizeable effect on the barrier height and thus, as we will see, on the tensile strength.

To obtain P_h via thermal fluctuations we have solved Eq. (3.19). We are not aware of experimental results on cavitation in helium mixtures, so we have used the same estimate for the prefactor J_{0T} that the one in the pure case (2.11), and the experimental volume and time $(V\tau)_e = 1$ cm^3 sec, since as we have already pointed out in the previous chapter, the tensile strength is not very sensitive on the numerical value neither of the prefactor nor of $(V\tau)_e$.

In figure 3.6, P_h is displayed as a function of T for pure ^{4}He and for several ^{3}He concentrations. For $T = 0$ the cavitation pressure corresponds to the spinodal one (we have neglected quantum fluctuations). One can see that for the lower concentration ($x = 10^{-4}$ %), the differences with pure ^{4}He are appreciable, ranging from ~ 0.5 bar at $T = 0.05\,$K to ~ 1 bar at $T = 0.2\,$K. Moreover, the homogeneous cavitation pressure differs from the spinodal pressure a lot more in the mixture than in the pure system. These effects are due to the presence of ^{3}He surface states.

Comparing the spinodal and cavitation pressures qualitative agreement with (3.28) is seen. For example, at $T = 100\,$mK, the difference between spinodal and cavitation pressure is 0.3 bar for pure ^{4}He, and 1.3 bar for $x = 1\%$.

By simple inspection of figure 3.6 we may infer that for temperatures above the $T \simeq 0$ region where cavitation is produced via quantum tunneling, the process occurs away from the spinodal pressure, so that none of the two approximations proposed by Lifshitz and Kagan [26] (i.e., near the spinodal or near saturation) apply here.

Finally, in figure 3.7 we display a sequence of bubble profiles for $x = 4\%$ and pressures $P = -7, -5, -4$ and -2 bar. Near the saturation pressure, bubbles are large in size and empty, with a ^{3}He shell located at the surface. When the pressure

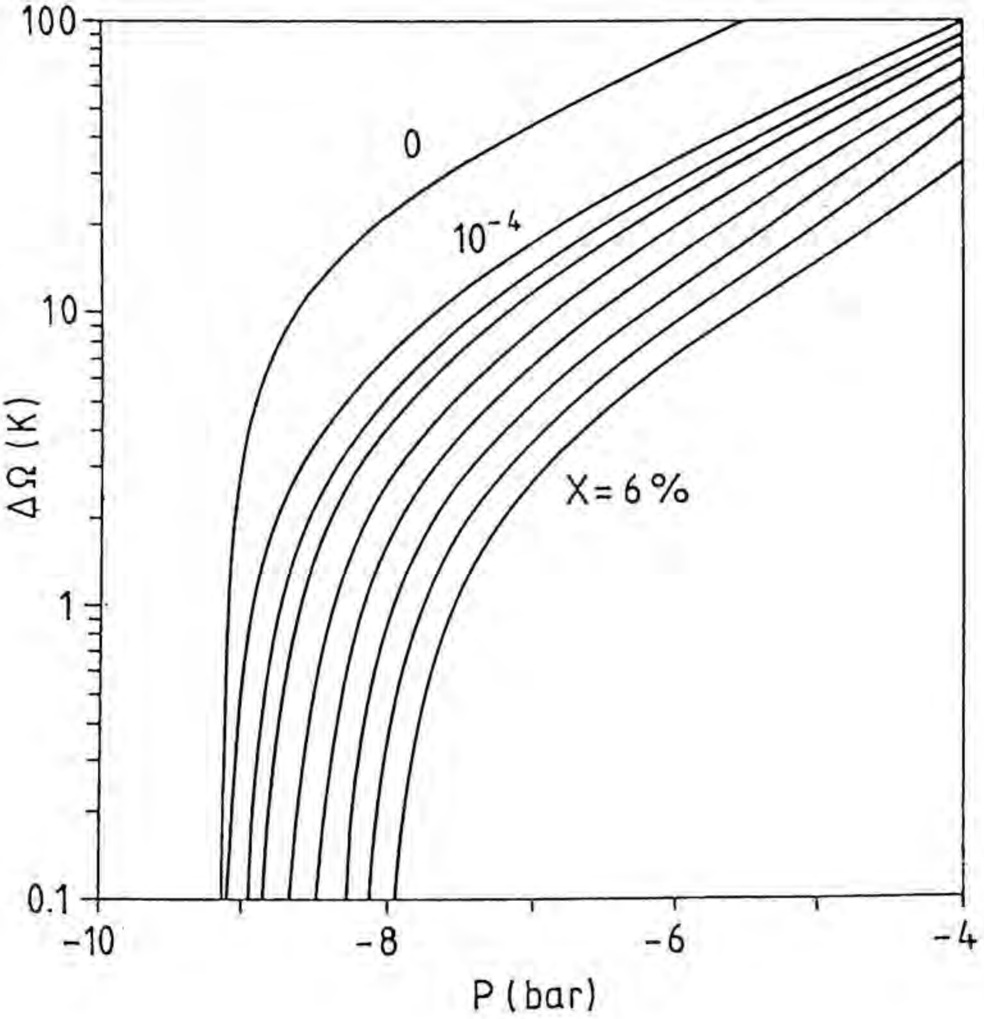

Figure 3.5. From top to bottom, cavitation barriers as a function of P for pure ^{4}He and for ^{3}He concentrations $x = 10^{-4}\%$, 0.5%, and 1 to 6%.

becomes more negative, the size of critical bubbles diminishes, and bubbles are first filled with ^{3}He before ^{4}He starts flowing in. The complicated morphology of these curves suggests that any schematic assumption about the shape of the density profiles in the study of cavitation is extremely complicated, whereas the density functional approach constitutes a reliable and affordable way of tackling this problem.

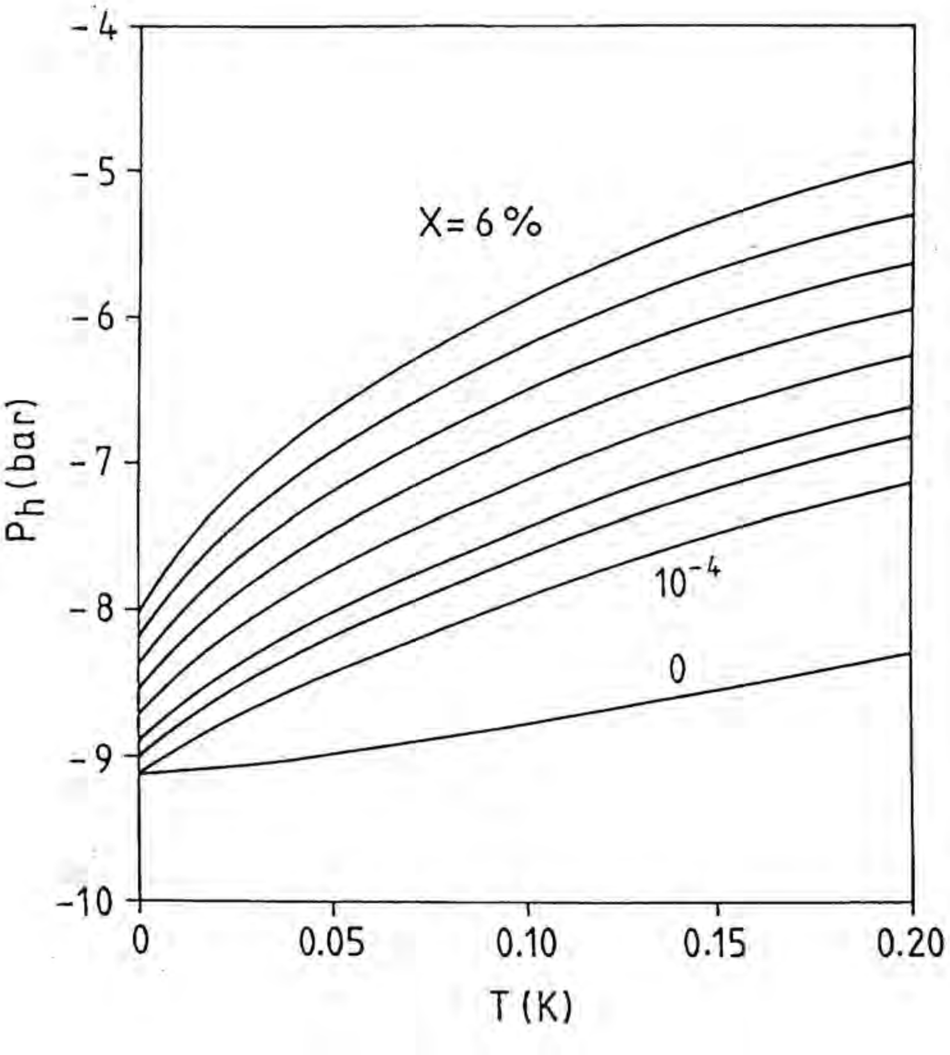

Figure 3.6. Homogeneous cavitation pressure P_h as a function of temperature for the same ^{3}He concentrations as in figure 3.5 (from bottom to top).

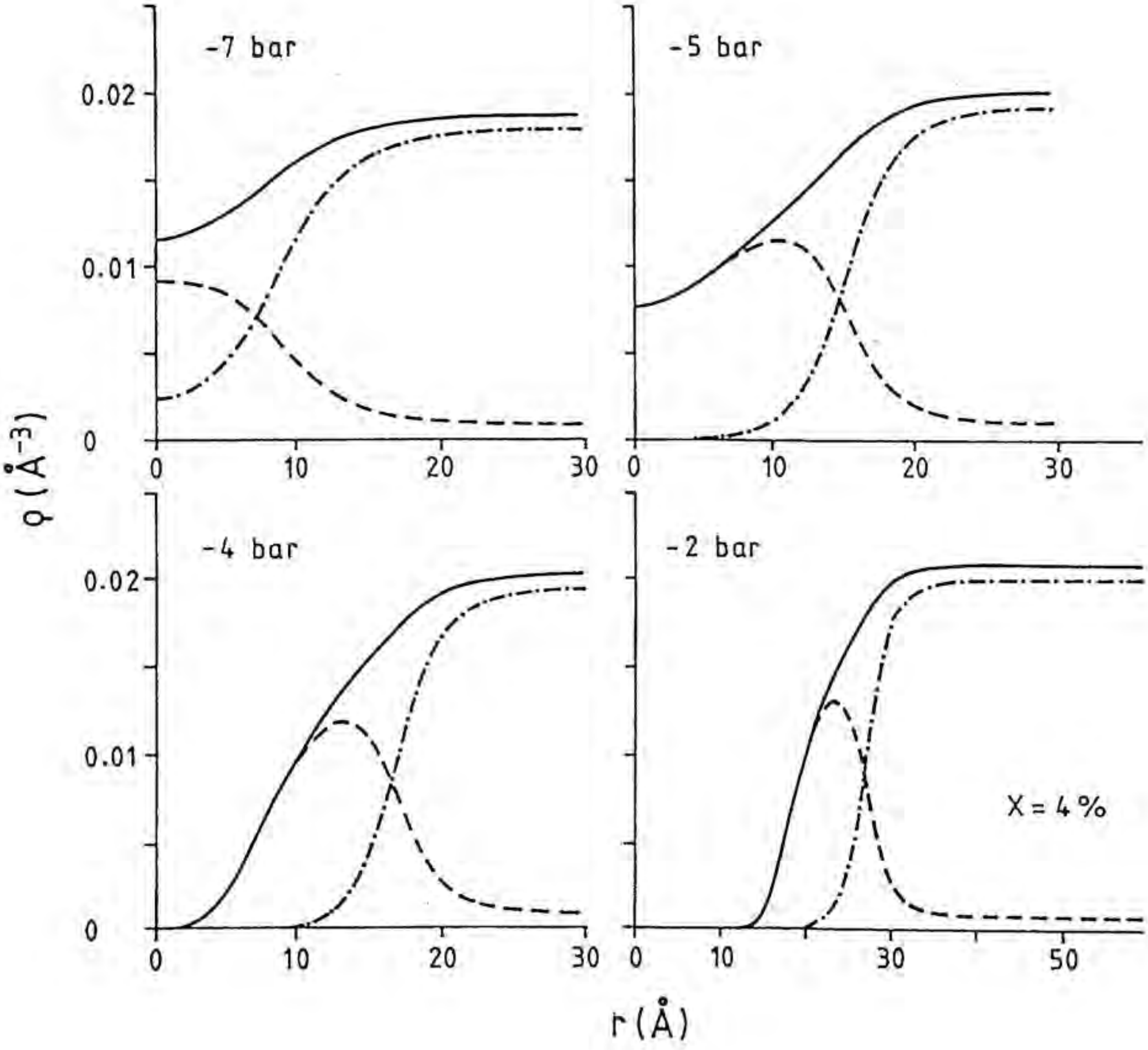

Figure 3.7. Density profiles corresponding to the critical bubbles for $P = -7, -5, -4$ and -2 bar. The ^{3}He concentration is $x = 4\%$.

3.5 Nucleation in supersaturated solutions at negative pressures

In the previous section we have already seen that for mixtures below saturation, in spite of existing both kind of configurations, the seed of phase separation is the bubble-like one, since its energy barrier is lower. Now we will complete the study at negative pressures considering mixtures above saturation. Within the density functional approach, we will determine the regions in the pressure-^{3}He-concentration plane where bubbles or drops likely drive the nucleation process, we will delimit the transition curve and compare it with the predictions of the capillarity model.

Particle density profiles $\rho_3(r)$ and $\rho_4(r)$ for the critical nucleus of total density $\rho(r) = \rho_3(r) + \rho_4(r)$, have been obtained by solving again the corresponding coupled EL equations. The boundary conditions are the same as in the previous section but now ρ_{3m} and ρ_{4m} are such that the homogeneous metastable mixture satisfies $P < 0$ and $x > x_{sat}$. It is worth emphasizing that the same boundary conditions lead in general to two different configurations: one corresponding to a bubble with a ^{3}He enrichment at the surface, and another corresponding to a ^{3}He drop, both embedded in the mixture. Different energy barriers are associated with both of these configurations.

Typical profiles of these two types of configurations are shown in Figs. 3.8 and 3.9, for a pressure of -2.3 bar and concentrations x =5.5 % and 7.5 %, respectively. For that pressure, the 5.5 % concentration point lies closer to the saturation curve than the 7.5 % point. As the *drop* nucleation barrier becomes infinite at this curve, the size of the critical cluster is larger (71 Å) in the former than in the latter (29 Å) case. Obviously, the variation in size for bubbles is not affected by crossing over the saturation line. In this example, the bubble radii are 17 and 15 Å for $x = 5.5$ % and 7.5 %, respectively. As a general trend, for given P and x, the size of the corresponding drop and bubble configuration differs most near saturation while they are similar when nearer the spinodal curve. It is worth noting that the pure ^{3}He-mixture interfacial region is rather independent of whether bubble or drop configurations are being formed (compare top and bottom panels in Figs. 3.8 and 3.9, for example).

We have calculated the nucleation barrier heights $\Delta\Omega$ of both configurations corresponding to a given metastable state (x, P). For those shown in Fig. 3.8, bubble nucleation is more favorable than drop nucleation: their barrier heights are 164 and

449 K, respectively. For the configurations shown in Fig. 3.9, the reverse situation is obtained: the barrier height for the drop is 71 K, whereas it is 123 K for the bubble. At the intermediate value $x = 6.54$ % the barrier heights become equal.

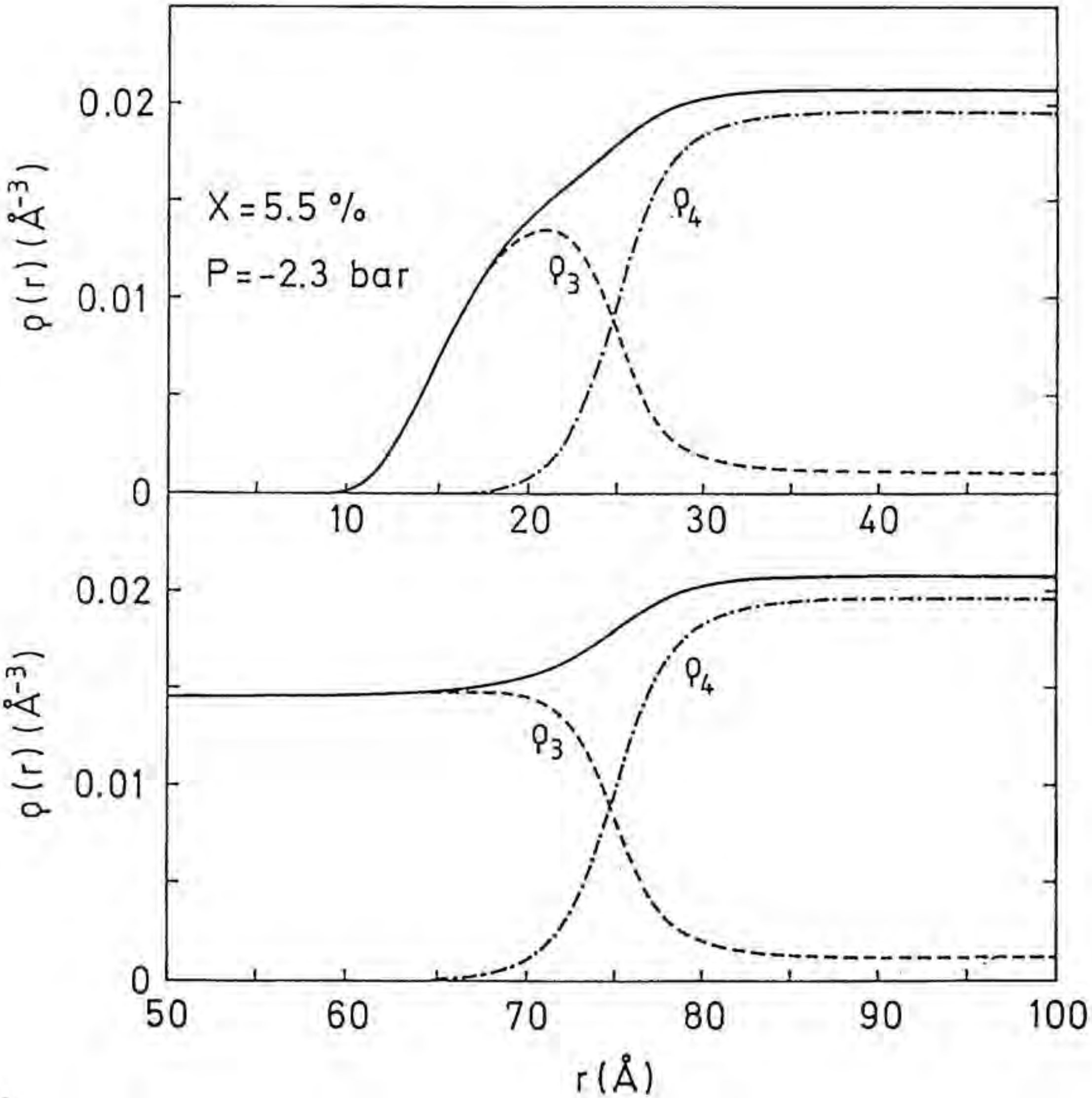

Figure 3.8. Density profiles for $x = 5.5$ % and $P = -2.3$ bar. Top panel, bubble configuration. Bottom panel, drop configuration. Dashed lines, ^{3}He densities; dashed-dotted lines, ^{4}He densities; solid lines, total densities.

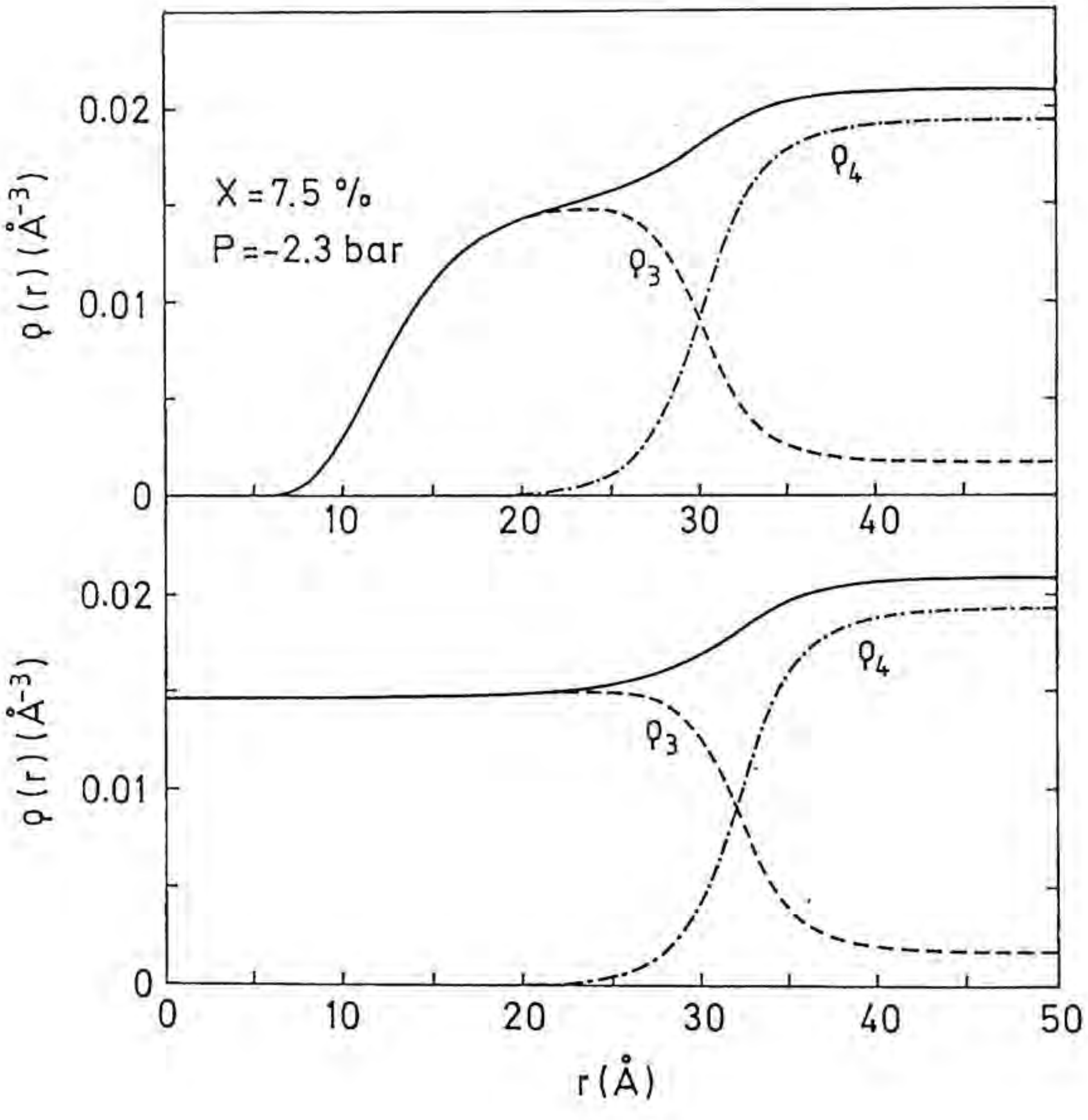

Figure 3.9. Same as Fig. 3.8 for x = 7.5 %.

In Fig. 3.10 we show the ^{3}He-drop nucleation barrier heights for different concentrations as a function of P. As expected, they diverge at saturation and vanish at spinodal values. The bubble barrier heights are displayed in Fig. 3.5. As functions of

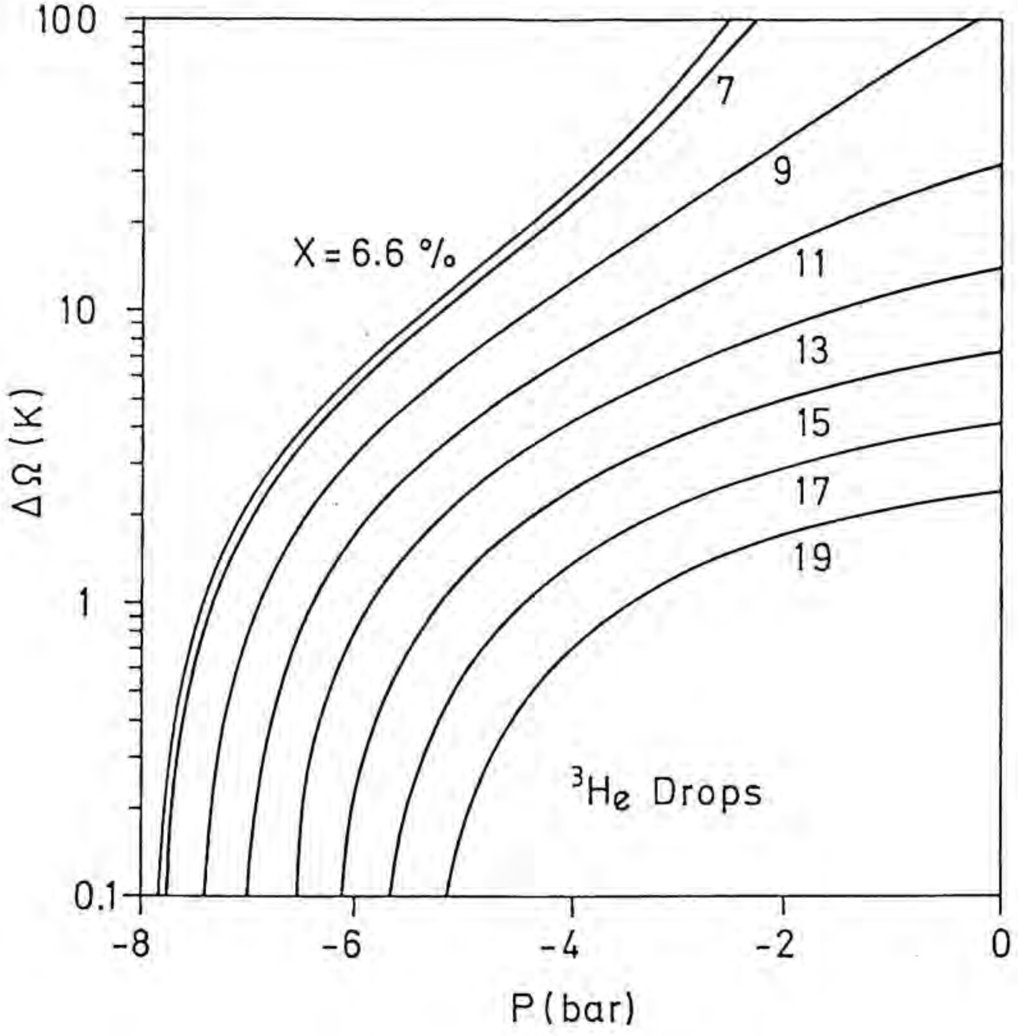

Figure 3.10. Drop barrier heights (K) as functions of pressure (bar). From top to bottom, the curves correspond to $x = 6.6$ (saturation), 7, 9, 11, 13, 15, 17 and 19 %.

P and x, the barriers $\Delta\Omega(P, x)$ define two surfaces: one corresponding to the bubble-like configuration with ^{3}He enrichment at the surface, and the other corresponding to the ^{3}He drop configuration, both embedded in the mixture. They grow from zero at the spinodal line, cross each other at the transition pressure P_t line and finally diverge at the corresponding saturation pressure, $P = 0$ for the the bubble-like configuration, and $P = P_{sat}(x)$ for the ^{3}He drop-like configuration. It is interesting to notice that, since experimentally at very low temperatures the saturation curve $x_{sat} = x(P)$ has a maximum at around $x_m = 9.5$ % [42], for $x > x_m$ the drop barrier always remains finite. This can be seen in Fig. 3.10, and indicates that the functional (3.1) is able to reproduce, at least qualitatively, this experimental fact.

The phase diagram of the mixture at $T = 0$ in the (P, x) plane is represented in Fig. 3.11 for negative pressures. The saturation curve is labeled as $P_{sat}(x)$, and the spinodal line as $P_{sp}(x)$ (see also Fig. 3.1). Also shown is the transition pressure line $P_t(x)$ where energy barriers for both configurations become equal. Phase transition will be driven by bubble nucleation on the left of that line, and by drop nucleation on the right. The configurations displayed in Figs. 3.8 and 3.9 are represented by a circle and a square, respectively. For pressures below ~ -3.8 bar, no genuine bubble configurations can be found in the mixture, and only ^{3}He-rich drops are present as nucleation clusters.

In the lower right-hand corner of Fig. 3.11 we display on a magnified scale the $P_t(x)$ curve and compare the capillarity (dashed line) with the density functional result. As expected, the capillarity approach is a good approximation only near saturation, i.e., zero pressure and concentrations close to 6.6 %. It is interesting to note that P_t exists for concentrations slightly higher than the saturation value at $P = 0$, and that it is a bivaluate function of x.

To make a quantitative estimate of the homogeneous nucleation pressure P_h, one may proceed as in the pure case, that is, consider a rate $J_T = 1\ \mathrm{cm}^{-3}\mathrm{sec}^{-1}$, or equivalently $(V\tau)_e = 1\ \mathrm{cm}^3$ sec, and solve Eq. (3.19) taking for $J_{0T} \sim 2 \cdot 10^{33}\ \mathrm{cm}^{-3}\ \mathrm{sec}^{-1}$ as in Ref. [27], and using the lower barrier height $\Delta\Omega$ that corresponds to either bubble or drop configuration. P_h is displayed in Fig. 3.11 as a function of x for 50 and 100 mK temperature. Notice that at a temperature as low as 50 mK, P_h differs appreciably from P_{sp} even at low ^{3}He concentrations. This is again a manifestation of the presence of ^{3}He surface states (Andreev states), see also Fig. 3.6.

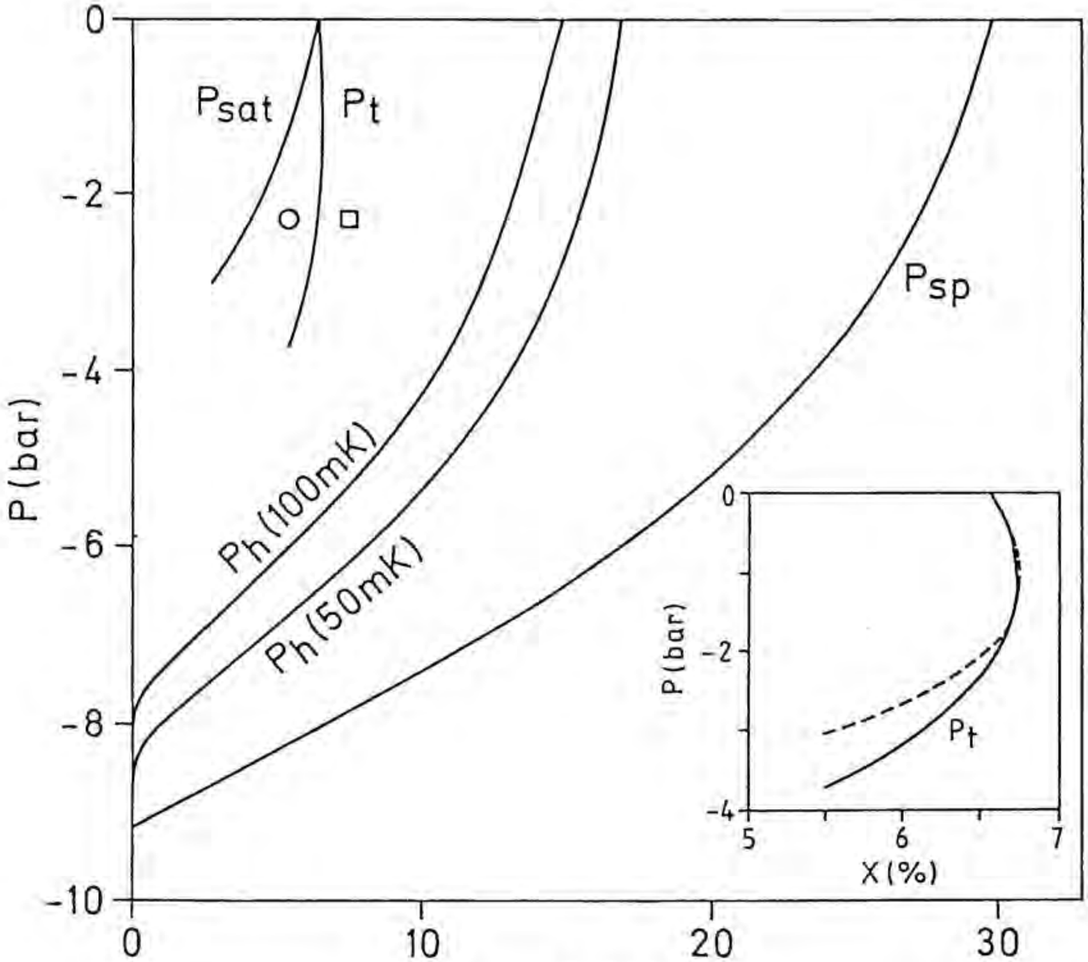

Figure 3.11. Transition pressure P_t from bubble to drop nucleation and homogeneous nucleation pressure P_h for $T = 50$ and 100 mK, as functions of ^{3}He concentration. Also shown are the saturation P_{sat} and spinodal P_{sp} curves. In the lower right-hand corner we show again P_t (solid line) and compare it with the result obtained in the capillarity approximation (dashed line).

3.6 Critical supersaturation at low temperatures and positive pressures

During the past fifteen years, there has been a common belief [43, 44] that supersaturated ^{3}He-^{4}He liquid mixtures at very low temperature could be found in a metastable state for ^{3}He concentrations well above the saturation value $x_0 \sim 6.6\%$ at pressure $P \sim 0$ [49]. That belief was motivated by an extrapolation to $T = 0$, of the measured ^{3}He chemical potential excess $\Delta\mu_3$ along the coexistence line carried out by Seligmann et al [55]. This extrapolation yields $\partial\Delta\mu_3/\partial x \geq 0$ up to $x > 16\%$, opening the possibility that the system can be in a metastable state up to or even above that concentration [36]. Lifshitz and coworkers [51] have studied nucleation in a capillarity model and have calculated the degree of supersaturation $\Delta x_{cr} \equiv x - x_0$ obtaining a value around 15 % and a crossing temperature T^* from thermal to quantum nucleation regimes of about 14 mK.

The first systematic study of phase separation from supersaturated ^{3}He-^{4}He liquid mixtures has been recently made [35], with the result that at $P \sim 3 - 5\,\text{bar}$, $\Delta x_{cr} \sim 0.2 - 0.5\%$, and $T^* \sim 20$ mK. Other experiments at lower pressures (Ref. [40] as quoted in [41]) yield $\Delta x_{cr} \sim 1\%$. It is worth to recall that the Ohio State group had actually found metastable ^{3}He-^{4}He solutions up to $\Delta x_{cr} \sim 0.3\%$ [49]. The above nucleation calculations are in sharp disagreement with these experimental results.

3.6.1 Nucleation of ^{3}He drops

Let us first review nucleation (either thermal or quantal) of ^{3}He-rich droplets in the mixture within the capillarity model and within our improved density functional approach, and show that it is hardly compatible with these experimental findings. Making use of the capillarity approximation, as we have already pointed out, the potential energy of a ^{3}He-nucleus of radius R in a metastable supersaturated mixture near saturation ($x \sim x_{sat}$, remember $x_{sat}(P = 0) = x_0$) has the form [41, 51]:

$$\Delta U(R) = 4\pi\sigma R^2 - \frac{4\pi R^3}{3}\rho_3\Delta\mu_3\,, \tag{3.29}$$

where σ is the surface tension of the ^{3}He-^{4}He interface, ρ_3 is the particle density of pure ^{3}He inside the droplet at a given pressure, and $\Delta\mu_3$ is the difference between the chemical potential of ^{3}He in the metastable, dilute phase, and in pure ^{3}He at saturation. Minimizing the right hand side of (3.29) with respect to R, the radius of the critical drop $R_c = 2\sigma/(\rho_3 \Delta\mu_3)$ and the critical barrier $\Delta U(R_c) = 4\pi {R_c}^2 \sigma/3$ are obtained.

To study thermal nucleation within this approximation, the same equations as in Sec. 3.3 can be used but with $\Delta U(R_c)$ instead of $\Delta\Omega$. This leads to the following expression that must be satisfied in order to observe nucleation

$$\Delta U(R_c) = T \, \ln \left[J_{0T} \, (V\tau)_e \right] . \tag{3.30}$$

Typical values of the logarithm are about 80 [16, 36, 41]. Taking $T \sim 100$ mK it yields $\Delta U(R_c) \sim 8$ K.

Using the experimental values $\sigma = 0.017 \pm 0.002$ K Å^{-2} [46] and $\rho_3 \sim 0.016$Å^{-3}, and approximating $\Delta\mu_3 \sim \Delta x \cdot \partial(\Delta\mu_3)/\partial x \,|_{x_{sat}} \sim 2.3\, \Delta x$ (K)†, one has

$$\Delta U(R_c) \sim 6.1 \cdot 10^{-2}/(\Delta x)^2 \ \ (\mathrm{K}) . \tag{3.31}$$

For $\Delta x \sim 0.004$, which is within the range of experimental values of [35], one gets $R_c \sim$ 230Å and $\Delta U(R_c) \sim 3800$ K, being over two orders of magnitude larger than the value at which phase separation via nucleation of ^{3}He drops mediated by thermal fluctuations would become possible. It is quite obvious that a poor evaluation of $\Delta U(R_c)$ also leads to a wrong value of T^*, since it is obtained from $\Delta U(R_c)$ and the underbarrier action S (usually determined in the WKB approximation) since $T^* = \Delta U(R_c)/(2\,S)$ [12].

One might argue about the validity of the capillarity approximation, as well as the value of $\partial(\Delta\mu_3)/\partial x \,|_{x_{sat}}$, which is crucial to obtain the barrier height. Let us first mention that the capillarity approximation is appropriate if the nucleation process takes place near the saturation curve [8], as the present case seems to be in view of the smallness of Δx_{cr} encountered [35, 40]. The reason is the large size of the critical drop, that makes curvature and compressional effects negligible.

To put our estimates of $\Delta U(R_c)$ and $\partial(\Delta\mu_3)/\partial x \,|_{x_{sat}}$ on firmer grounds, we have resorted to the density functional (3.1) to obtain these quantities following the method already pointed out in Sec. 3.3. Figure 3.12 shows $\Delta\mu_3$ as a function of x for $P = 0$ and 3 atm. The results obtained in [55], as extrapolation of experimental measurements, are

---

†We have computed $\partial(\Delta\mu_3)/\partial x \,|_{x_{sat}}$ from Fig. 4 of [55], obtaining 2.3 K instead of the value quoted in [51] (~ 0.3 K) got also from the same reference. In our opinion, this gross error invalidates the numerical calculations of Lifshitz et al. [51].

also displayed. The functional has been adjusted to reproduce the maximum solubility of ^{3}He in ^{4}He at zero pressure (x_0), i.e., $x_{sat}(P = 0) \sim 6.6\%$, and it yields $x_{sat}(P = 3\text{atm}) \sim 7.9\%$. The slopes at these values of x_{sat} are 2.34 K and 2.13 K, respectively. We can appreciate a good agreement between our calculations and those of [55].

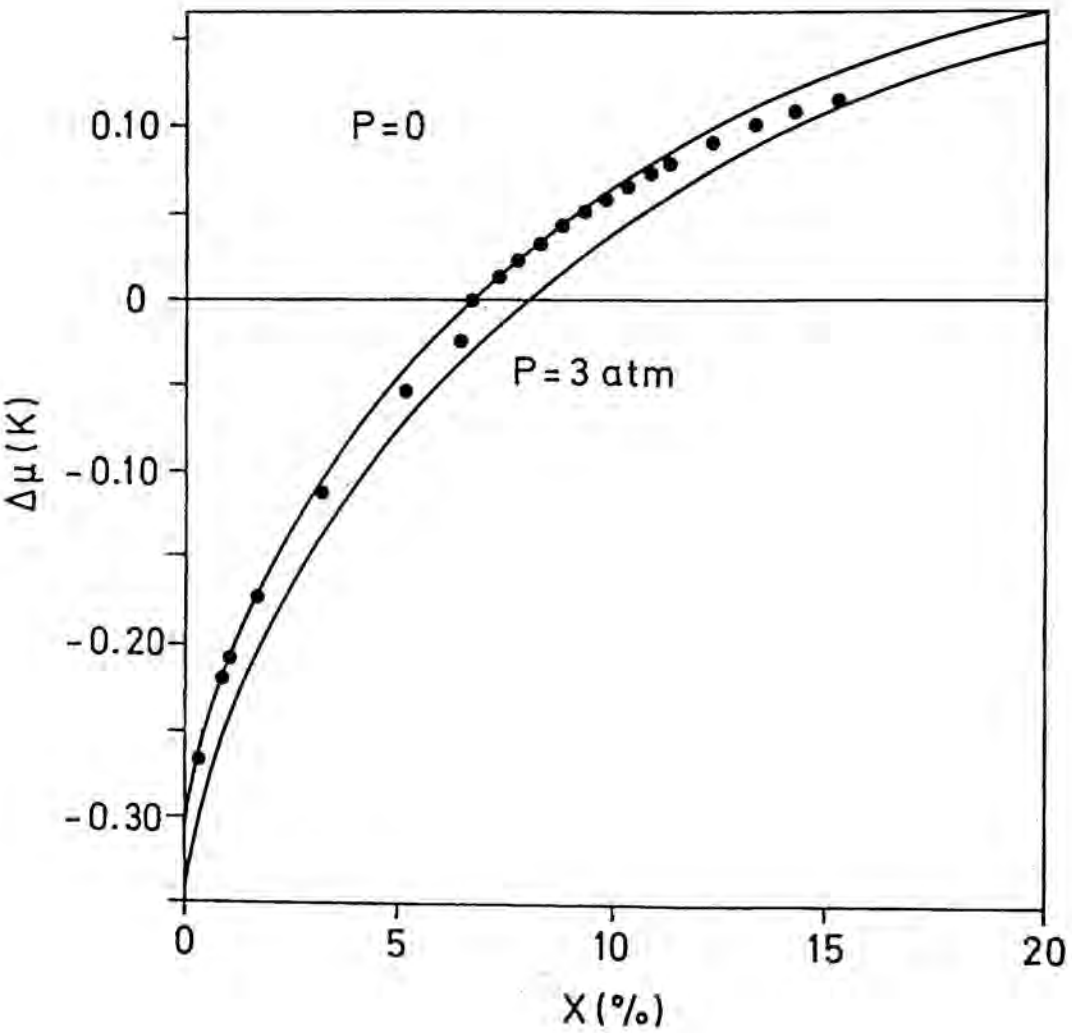

Figure 3.12. ^{3}He chemical potential excess as a function of the ^{3}He concentration for $P = 0$ and 3 atm (solid lines). The dots have been extracted from Fig. 4 in Ref. [55].

Figure 3.13 shows ΔU as a function of x for $P = 0$ and 3 atm. It is worth it to notice that $\Delta U \sim 8$ K for $x \sim 0.15$ at $P = 0$. This result is consistent with the positiveness of $\partial(\Delta\mu_3)/\partial x$ up to $x \sim 0.16$ found in [55], and up to ~ 0.3 found in [36],

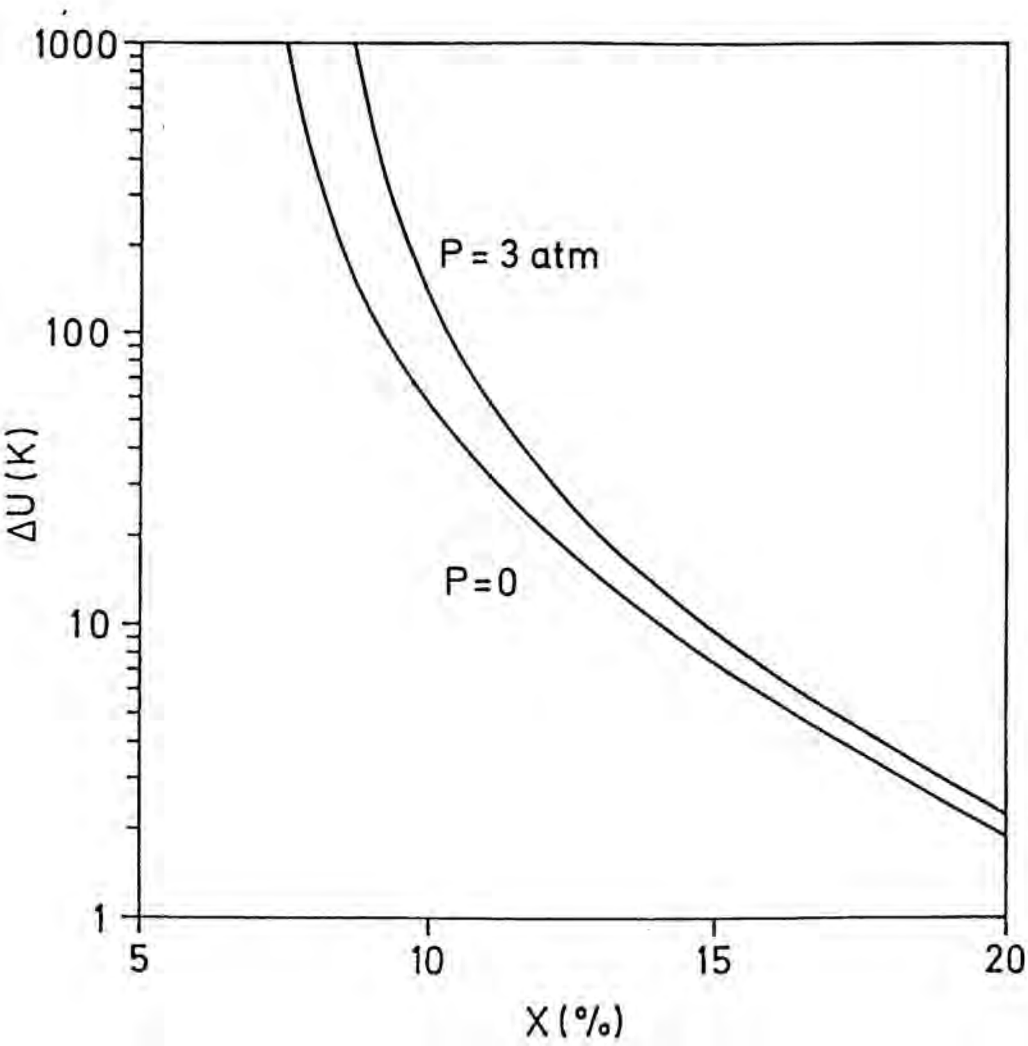

Figure 3.13. Nucleation barrier of ^{3}He-rich drops as a function of the ^{3}He concentration for $P = 0$ and 3 atm.

indicating that, if phase separation by ^{3}He drop nucleation takes place, the degree of supersaturation would be $\Delta x_{cr} \sim 9\%$. The corresponding radius of the critical nucleus is $R_c \sim 15$Å (see Fig. 3.14). However, if $\Delta x_{cr} \sim 0.4\%$, $x = x_{sat} + \Delta x_{cr} \sim 7\%$, $R_c \sim 250$Å and $\Delta U \sim 4500$ K, out of scale in Fig. 3.13. That would have be the result obtained in the capillarity approximation if we had used there the same value of σ (see [46][‡]).

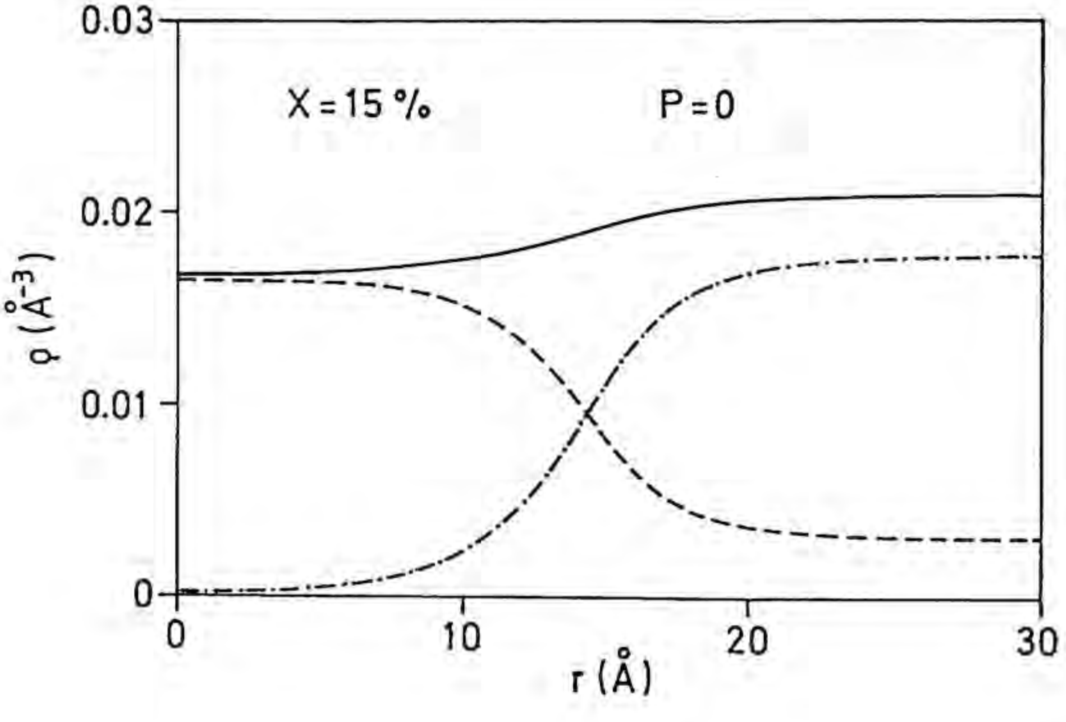

Figure 3.14. Critical-drop density profile corresponding to the situation $P = 0$, $x = 15\%$. Solid line, total density. Dashed-dotted line, ^{4}He density. Dashed line, ^{3}He density.

[‡] The value obtained using our density functional (3.1) is $\sigma \sim 0.018$ K Å^{-2} (see Sec. 3.2), well within the experimental error bars.

3.6.2 Vortex destabilization

A possible way to get rid of these difficulties is to consider the existence of vortices in the mixture [56], since ^{4}He is superfluid under the given conditions. Let us assume the hollow core model for the ^{4}He vortex, i.e., the ^{4}He density is zero within the core and equal to the bulk value ρ_4 elsewhere. As x increases, the ^{3}He atoms located at the surface of the vortex [57] migrate to the interior of the hollow core. If ρ_3 is the ^{3}He particle density inside the vortex core, then for $x \gtrsim x_{sat}$ the energy per unit length of a vortex of radius a and circulation n can be written as:

$$E_v = 2\pi\sigma a - \pi a^2 \rho_3 \, \Delta\mu_3 + \pi n^2 \frac{\hbar^2}{m_4} \rho_4 \ln\left(\frac{a_\infty}{a}\right) , \tag{3.32}$$

where m_4 is the atomic mass of ^{4}He and a_∞ is a large enough radius. Minimizing E_v with respect to a we get the radius of the stable vortex. If $a_0 \equiv n^2\hbar^2\rho_4/(2\sigma m_4)$ and $\mu_c \equiv \sigma^2 m_4/(2n^2\hbar^2\rho_3\rho_4)$, one has

$$a = 2a_0 \frac{\mu_c}{\Delta\mu_3}\left[1 \pm \sqrt{1 - \frac{\Delta\mu_3}{\mu_c}}\right] \tag{3.33}$$

The plus sign corresponds to a maximum of E_v with $a = a_>$, and the minus sign to the stable minimum with $a = a_<$. a_0 is the equilibrium radius for $\Delta\mu_3 = 0$, i. e., for $x = x_{sat}$. This simple expression shows that for $\Delta\mu_3 > \mu_c$, the vortex is no longer stable. Taking $n = 1$, $\rho_4 = 0.020\,\text{Å}^{-3}$ and $\hbar^2/m_4 \sim 12$ K Å^2 one gets $a_0 = 7.1$ Å and $\mu_c = 0.038$ K. Thus, for $\Delta\mu_3 = 0.038$ K the mixture will necessarily undergo phase separation. Using our linear approximation this corresponds to $\Delta x_{cr} \sim 1.6\%$ at $P = 0$, which is considerably smaller than the quantity obtained from ^{3}He drop nucleation.

That value constitutes an upper limit of the actual Δx_{cr}, as we have not taken into account that the stable vortex may destabilize by quantum or thermal fluctuations. The barrier to be overcome, per vortex unit length, is the difference $E_v(a_>) - E_v(a_<)$, and may be written as function of $y \equiv \Delta\mu_3/\mu_c$,

$$\Delta U(y) = \frac{4\pi a_0 \sigma}{y}\sqrt{1-y} + 2\pi a_0 \sigma \ln\left(\frac{1-\sqrt{1-y}}{1+\sqrt{1-y}}\right) . \tag{3.34}$$

Then, $\Delta U(y) = 0$ for $y = 1$ and diverges at the saturation value x_{sat}, for which $y = 0$. Let now L_v be the vortex length per unit volume in the experimental sample. The probability per unit time and unit vortex length of thermally forming a critical vortex of length L_c is $J_T = J_{0T}{}^v \exp(-L_c\,\Delta U/T)$. Consequently, to observe such a fluctuation one must have $L_c\,\Delta U = T\,\ln(L_v V \tau J_{0T}^v)$. Taking $L_c \sim 10\ a_0$ and $T = 0.1$ K, we get $\Delta x_{cr} \sim 1.3 - 1.4\%$ for values of the logarithm between 80 - 40. We are thus led to conclude that barrier crossing is not a very favorable process.

We have also considered the possible growth of a ^{3}He-rich drop on a stable vortex of radius a. The previous calculations indicate that $a << R$, in which case it is easy to check that the associated barrier ΔU for this process is the one given by (3.29) plus a corrective term ΔU_{cor}:

$$\Delta U_{cor} = \left\{ -4\pi a\sigma + 2\pi a^2 \rho_3 \Delta\mu_3 + 2\pi\, \frac{\rho_4 \hbar^2}{m_4} n^2 \left[1 - \frac{1}{2}\left(\frac{a}{R}\right)^2 + \ln\left(\frac{a}{2R}\right) \right] \right\} R \qquad (3.35)$$

this correction is negative, and for $\Delta x_{cr} \sim 0.4\%$ and $P = 0$ we get $R_c \sim 210$ Å and $\Delta U(R_c) = 2200$ K, which is still too large a value.

Chapter 4

Quantum cavitation in liquid helium

In the previous chapters, we have investigated thermal cavitation in liquid ^{3}He and ^{4}He for temperatures above a few hundred mK. For temperatures below a certain value T^* which we shall call crossover temperature, one expects that quantum tunneling cavitation becomes more favorable than thermal cavitation. It means that below T^* the tensile strength will be determined by quantum tunneling.

An elaborated description of the cavitation process was furnished by Lifshitz and Kagan [26], who used the classical capillarity model near the saturation line, and a density functional-like description near the spinodal line. More recently, the method was further elaborated by Xiong and Maris [12]. These authors conclude that there is not clear way to interpolate between these two regimes, which makes quite uncertain the range of pressures in which each of them is valid.

We have devised a simple yet reliable method to calculate T^* based on a density functional approach which overcomes the limitations inherent to previous methods. The density functional approach allows to calculate in a natural way the minimum work required to form a critical bubble without making any assumption on the shape of the density profile as the capillarity model does, thus providing well behaved barriers in all the pressure range. Moreover, as a great deal of experimental information is used to fix the parameters defining the functional, one expects that these barriers are quantitatively accurated.

This chapter is organized as follows. In Sec. 4.1 we present the method to calculate cavitation barriers within a density functional formalism. While for thermal cavitation only the barrier height is needed, for quantum cavitation one has to know the barrier shape as a function of same collective variables. In Sec. 4.2 quantum cavitation through the barrier is described. We will show that to obtain T^*, only a detailed knowledge of the barrier near the top is needed. The homogeneous cavitation pressure is obtained in Sec. 4.3.

During the completion of this work, we became aware of a paper by Maris [58] addressing the same problem with a method similar to ours in some aspects. Our results for T^* are a factor of 2–3 smaller than his for both helium isotopes. Given the uncertainties inherent to both calculations and the differences between the density functionals we are using, rather than a discrepancy we consider it as a fair agreement.

4.1 Cavitation barriers

The starting point is the zero-temperature density functionals for ^{4}He and ^{3}He described in Refs. [18] and [59], which as well as those of Refs. [12] and [60] for example, reproduce the zero temperature equation of state (EOS) of both helium isotopes, and the surface tension of liquid helium. Since we are interested in temperatures below $\sim$ 200 mK, it is legitimate to neglect any thermal dependence in the functionals. As ^{3}He is considered in the normal phase, for this isotope 'zero temperature' means $T \sim 3$ mK.

At given pressure (negative in the cavitation case but above the spinodal line), we proceed as follows. First, we determine the corresponding particle density of the metastable homogeneous liquid ρ_m inverting the EOS, and the corresponding chemical potential μ. The particle density profile of the *critical* bubble $\rho_c(r)$ is then obtained, as in chapter 2, solving the Euler-Lagrange equation

$$\frac{\delta \mathcal{E}}{\delta \rho} = \frac{\partial \mathcal{E}}{\partial \rho} - \nabla \frac{\partial \mathcal{E}}{\partial (\nabla \rho)} = \mu \, , \tag{4.1}$$

where $\mathcal{E}(\rho)$ is the energy density funcional, instead of the free energy density. We shall restrict our calculation to spherically symmetric bubbles. The boundary conditions for finding a physical solution to Eq. (4.1) are $\rho'(0) = 0$ and $\rho(r \to \infty) = \rho_m$, where the prime denotes the r-derivative. The barrier height is the difference between the grand potential of the critical bubble and that of the homogeneous liquid:

$$\Delta\Omega_{max} = \int d\mathrm{r} \left[\mathcal{E}[\rho_c(r)] - \mathcal{E}(\rho_m) - \mu[\rho_c(r) - \rho_m]\right] . \tag{4.2}$$

As we have previously indicated, to compute the quantum tunneling through the barrier we need the barrier shape as function of a set of collective variables chosen to model the growing of the critical bubble. To better understand our method, let us first consider the capillarity model, in which the critical bubble density profile is

$$\rho_c(r) = \rho_m \left[1 - \Theta(R_c - r)\right] , \tag{4.3}$$

where Θ is the step function and R_c is the critical radius that can be written in terms of the surface tension σ and the pressure P as $R_c = 2\sigma/|P|$. The cavitation barrier is

$$V(r) = 4\pi r^2\sigma - \frac{4}{3}\pi r^3 |P| \tag{4.4}$$

which intersects the r-axis at $R_M = 3R_c/2$. From $r = 0$ to R_M one can represent the dynamical evolution of the bubble by a series of density profiles such as

$$\begin{aligned} \rho_\delta(r) &= \rho_m[1 - \Theta(R_c + \delta - r)] \\ &= \rho_c(r - \delta) . \end{aligned} \tag{4.5}$$

The 'collective' variable δ represents the displacement of the bubble surface from R_c. It can be made time-dependent, and varying it from $-R_c$ to $R_c/2$ all physical configurations from the homogeneous metastable liquid to the barrierless bubble configuration are generated.

Within the density functional approach we have proceeded in the same way. After obtaining $\rho_c(r)$ at given pressure, we define a continuous set of densities by a rigid transportation of $\rho_c(r)$:

$$\rho_\delta(r) \equiv \begin{cases} \rho_c \quad (r = 0) & \text{if } r \le \delta \\ \rho_c \quad (r - \delta) & \text{if } r \ge \delta \, . \end{cases} \tag{4.6}$$

This amounts to keep frozen the surface diffuseness of the bubble. It is worth to realize that δ can be positive or negative, whereas r is always positive.

The barrier is then obtained as a function of δ:

$$\Delta\Omega(\delta) = \int \left[\mathcal{E}(\rho_\delta) - \mathcal{E}(\rho_m) - \mu(\rho_\delta - \rho_m)\right] d\mathbf{r}\,. \tag{4.7}$$

Figs. 4.1 (a) and (b) show $\Delta\Omega(\delta)$ and the particle density profile, respectively, for ^{4}He at $P = -5.39$ bar. We define a negative δ-value δ_0 imposing that $\Delta\Omega(\delta_0) = 10^{-6}$ K, and analogously a positive one δ_M, i.e., $\Delta\Omega(\delta_M) = 10^{-6}$ K. The interval $[\delta_0, \delta_M]$ constitutes the range of physical δ-values. δ_0 and δ_M depend on ρ_m or equivalently, on P.

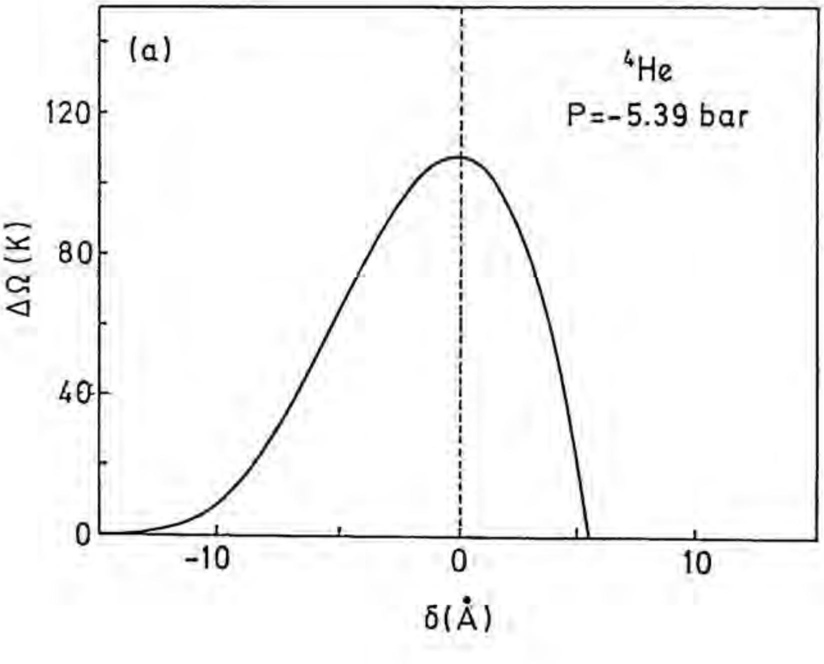

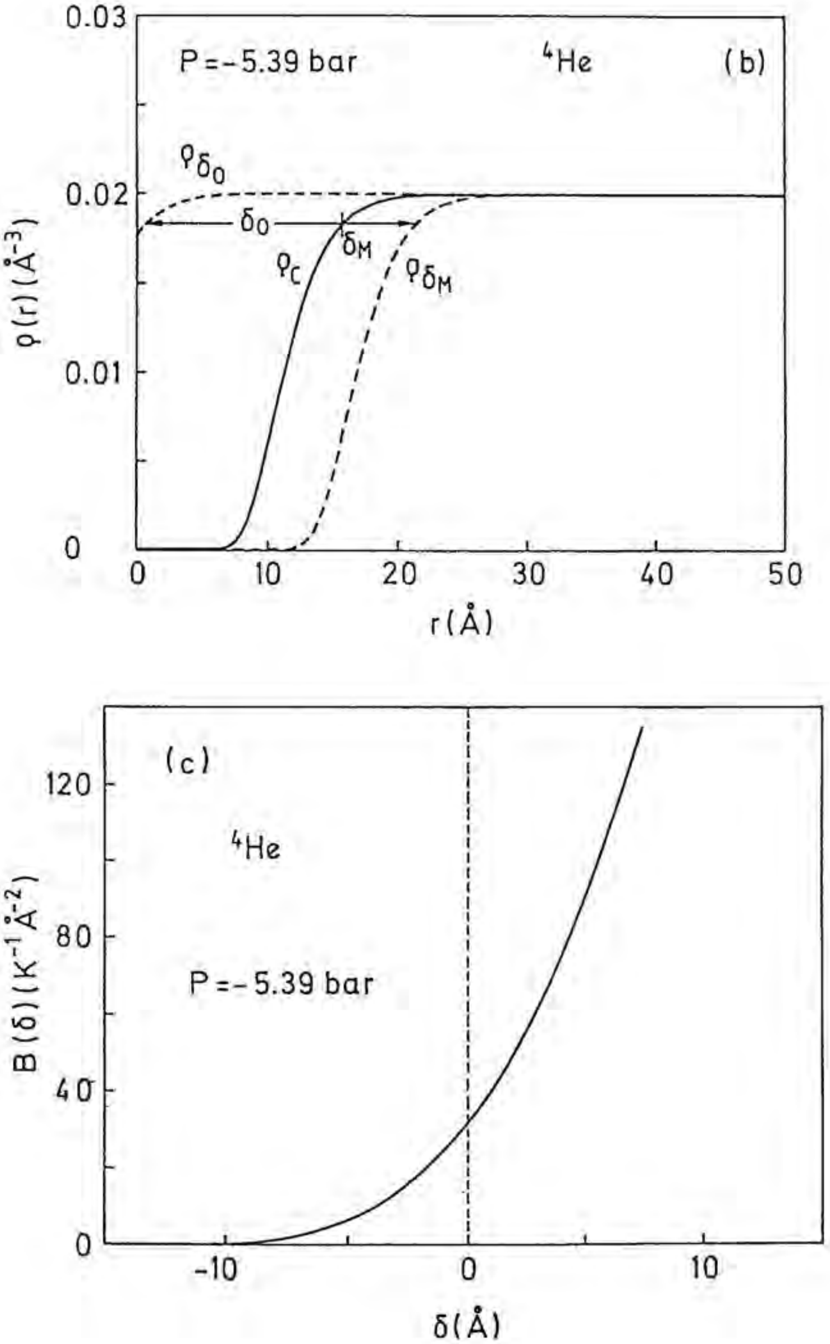

Figure 4.1. Referring to ^{4}He at $P = -5.39$ bar, we show: (a) the quantum nucleation barrier $\Delta\Omega$ (K) as a function of the displacement δ (Å); (b) the particle density profiles corresponding to the critical bubble configuration (ρ_c) and two configurations associated with displacements δ_0 and δ_M; (c) the mass parameter $B(\delta)$ (K^{-1} Å^{-2}) as a function of δ (Å).

The dynamics of the cavitation process comes in if we make δ time-dependent. Within our model, this is the only collective variable describing the bubble expansion: all the time-dependence will be in $\delta(t)$. The kinetic energy associated with the expansion is

$$E_{kin} = \frac{m}{2} \int d\mathbf{r}\, \rho(\vec{r},t)\, \vec{u}^2(\vec{r},t)\,, \tag{4.8}$$

where $\vec{u}(\vec{r},t)$ is the velocity field which can be formally obtained from the continuity equation

$$\frac{\partial \rho}{\partial t} + \vec{\nabla}(\rho\vec{u}) = 0\,. \tag{4.9}$$

It yields:

$$u(r,t) = -\frac{1}{r^2 \rho(r,t)} \int_0^r s^2\, \dot{\rho}(s,t)\, ds\,. \tag{4.10}$$

By construction,

$$\rho(r,t) = \rho_c(r - \delta(t))\,. \tag{4.11}$$

Thus,

$$\dot{\rho}(r,t) = -\rho_\delta'(r)\dot{\delta}\,. \tag{4.12}$$

The spherically symmetric velocity field then reads:

$$u(r,t) = -\frac{\dot{\delta}}{r^2 \rho_\delta(r)} \left[r^2 \rho_\delta(r) - 2 \int_0^r s\, \rho_\delta(s)\, ds \right]. \tag{4.13}$$

Defining the mass parameter $B(\delta)$ as

$$E_{kin} \equiv \frac{\hbar^2}{2}\, B(\delta)\, \dot{\delta}^2\,, \tag{4.14}$$

we get

$$B(\delta) = \frac{4\pi m}{\hbar^2} \int_0^\infty \frac{dr}{r^2 \rho_\delta(r)} \left[r^2 \rho_\delta(r) - 2 \int_0^r ds\, s\, \rho_\delta(s) \right]^2. \tag{4.15}$$

We show $B(\delta)$ in Fig. 4.1 (c) for the same conditions as in Fig. 4.1 (a) and (b). The mass parameter $B(\delta)$ is small for 'large' negative δ-values, those for which the parallel transportation of the critical density is a priori less justified. The importance of this point in the calculation of the tunneling probability will be made clear in the next section.

4.2 Quantum Cavitation

Below T^*, cavitation proceeds by quantum tunneling through the barrier. The cavitation rate, defined as the number of bubbles formed per unit time and unit volume adopts the form:

$$J_Q = J_{0Q}\,\exp(-S)\,, \tag{4.16}$$

where the prefactor J_{0Q} is of the order of the number of cavitation sites per unit volume times an attempting frequency, and $\exp(-S)$ is the tunneling probalility. For a given energy below the maximum of the barrier, the simplest way to obtain S is to make use of the WKB approximation [61]:

$$S^{WKB} = 2\int_{\delta_{left}}^{\delta_{rigth}} d\delta\,\sqrt{2\,B(\delta)\,[\Delta\Omega(\delta) - E]}\,, \tag{4.17}$$

where δ_{right} (δ_{left}) is the larger (smaller) of the two solutions of the equation $\Delta\Omega(\delta) = E$.

The WKB approximation is known to fail for energies close to the maximum of the barrier. This is a crucial point for what it follows. Lacking of a better choice, from now on we shall put $E = 0$ in S^{WKB}, defining:

$$S^{WKB} \equiv 2\int_{\delta_0}^{\delta_M} d\delta\,\sqrt{2\,B(\delta)\Delta\Omega(\delta)}\,. \tag{4.18}$$

It is obvious from the above expressions that contributions from negative δ-values to S^{WKB} are quenched as it is the product $B(\delta)\Delta\Omega(\delta)$ what really matters.

To improve on the WKB approximation, let us define the effective action [62, 63, 64]

$$S^Q = \int_{-\beta/2}^{\beta/2} d\tau\,\left[\frac{1}{2}B(\delta)\dot{\delta}^2 + \Delta\Omega(\delta)\right] \tag{4.19}$$

evaluated along the extremum trajectory. The path $\delta(\tau)$ defined in imaginary time τ has to fulfill the periodic boundary condition $\delta(-\beta/2) = \delta(\beta/2)$. Imposing the extremum condition on the action one gets the following equation of motion for $\delta(\tau)$:

$$B(\delta)\,\ddot{\delta} + \frac{1}{2}\frac{\partial B}{\partial\delta}\,\dot{\delta}^2 = \frac{\partial\Delta\Omega}{\partial\delta} \tag{4.20}$$

Notice that the effect of continuing the action to imaginary times is to invert the 'potential', i.e., $\Delta\Omega \to -\Delta\Omega$ in the equation of motion and the identification $T = 1/\beta$.

Multiplying Eq. (4.20) by $\dot{\delta}$ we have

$$\frac{d}{d\tau}\left[\frac{1}{2}B(\delta)\dot{\delta}^2 - \Delta\Omega(\delta)\right] = 0\,. \tag{4.21}$$

Thus

$$\frac{1}{2}B(\delta)\dot{\delta}^2 - \Delta\Omega(\delta) = constant = -E\,, \tag{4.22}$$

with $E > 0$. The turning points δ_1 and δ_2 are such that $\Delta\Omega(\delta_1) = \Delta\Omega(\delta_2) = E$. Integrating Eq. (4.22) we get the period β:

$$\beta(E) = 2\int_{\delta_1}^{\delta_2} d\delta \sqrt{\frac{B(\delta)}{2\,[\Delta\Omega(\delta) - E]}}\,. \tag{4.23}$$

Using that

$$d\tau = \sqrt{\frac{B(\delta)}{2\,[\Delta\Omega(\delta) - E]}}\,d\delta\,, \tag{4.24}$$

the action (4.19) becomes

$$S^Q(E) = 2\int_{\delta_1}^{\delta_2} d\delta\,[2\,\Delta\Omega(\delta) - E]\sqrt{\frac{B(\delta)}{2\,[\Delta\Omega(\delta) - E]}}\,. \tag{4.25}$$

For $E = 0$, S^Q reduces to S^{WKB}, Eq. (4.18). We can now obtain the crossover temperature. Above T^*, cavitation proceeds thermally, and the cavitation rate reads:

$$J_T = J_{0T}\,\exp\left[-\frac{\Delta\Omega_{max}}{T}\right]\,, \tag{4.26}$$

where the pre-exponential factor J_{0T} depends on the dynamics of the cavitation process. If at T^* $J_{0T} \approx J_{0Q}$, equating Eqs. (4.16) and (4.26) we get:

$$S^Q(E = \Delta\Omega_{max}) = \frac{\Delta\Omega_{max}}{T^*}\,. \tag{4.27}$$

Going back to Eq. (4.25) we can write for $E \approx \Delta\Omega_{max}$,

$$S^Q(E \approx \Delta\Omega_{max}) \approx 2\,\Delta\Omega_{max}\int_{\delta_1(E\approx\Delta\Omega_{max})}^{\delta_2(E\approx\Delta\Omega_{max})} d\delta\,\sqrt{\frac{B(\delta)}{2\;[\Delta\Omega(\delta) - E]}}\,. \tag{4.28}$$

Comparing with Eq. (4.23) we have that $T^{*-1} = \beta(E \approx \Delta\Omega_{max})$. Developing Eq. (4.23) around the maximum of $\Delta\Omega$ located at $\delta = 0$, we finally get

$$T^* = \frac{1}{2\pi}\sqrt{-\left.\frac{\partial^2\Delta\Omega}{\partial\delta^2}\Big/B(\delta)\right|_{\delta=0}}\,. \tag{4.29}$$

Eq. (4.29) shows that to obtain T^* *only small variations around $\delta = 0$ are needed*, and constitutes one of the main results of the present work. It implies that the basic uncertainty in the determination of T^* arises from how accurate is the density functional $\mathcal{E}(\rho)$ to describe the critical bubble. Any further improvement on $\mathcal{E}(\rho)$ will automatically result in an improvement on the determination of T^* from Eq. (4.29). Since the whole procedure has been carried out for a given pressure P, Eq. (4.29) gives $T^*(P)$. Crossover temperatures for ^{4}He and ^{3}He as a function of pressure are displayed as solid lines in Figs. 4.2 (a) and (b), respectively. Cavitation has to proceed thermally for temperatures above 121 mK for ^{4}He, and above 73 mK for ^{3}He, *irrespective of the value of the (negative) pressure.*

T^* goes to zero at the spinodal and saturation points. Near the saturation point, the critical bubbles are quite large, and so is B which actually diverges at saturation. Near the spinodal point, B goes to zero but $\partial^2\Delta\Omega/\partial\delta^2|_0$ goes to zero faster. The result is that T^* becomes zero at the spinodal and saturation points. Also shown in Fig. 4.2 (dashed lines) is the WKB result T^*_{WKB} obtained from

$$T^*_{WKB} \equiv \frac{\Delta\Omega_{max}}{S_{WKB}} . \tag{4.30}$$

It can be seen that the $E = 0$ WKB approximation is very good at all pressures. It means that T^* as obtained from S^Q is almost independent of the energy $E \in [0, \Delta\Omega_{max}]$ used to compute the barrier penetrability. This is quite surprising in view of the barrier shapes, which look very similar to that shown in Fig. 4.1 (a).

A way to understand this is to write Eq. (4.20) in a manner that makes clear the quasi-harmonic dependence of $\Delta\Omega$ on a collective variable related to δ. Defining [65]

$$z \equiv \int_0^\delta dy \sqrt{\frac{B(y)}{\hat{B}}} , \tag{4.31}$$

where $\hat{B}$ is a dimensional constant to render $B(y)/\hat{B}$ dimensionless, Eq. (4.20) becomes

$$\hat{B}\ddot{z} - \frac{d\Delta\Omega}{dz} = 0 . \tag{4.32}$$

Fig. 4.3 displayes $\Delta\Omega$ (K) for ^{4}He at $P = -5.39$ bar. As a function of z, $\Delta\Omega$ looks rather parabolical. This explains the weak energy dependence of S^Q, since it is a trivial matter to show that for a parabolic barrier such as*

$$\Delta\Omega = -a\delta^2 + b\delta \tag{4.33}$$

---

*We have set $B(\delta) \equiv 1$ for convenience.

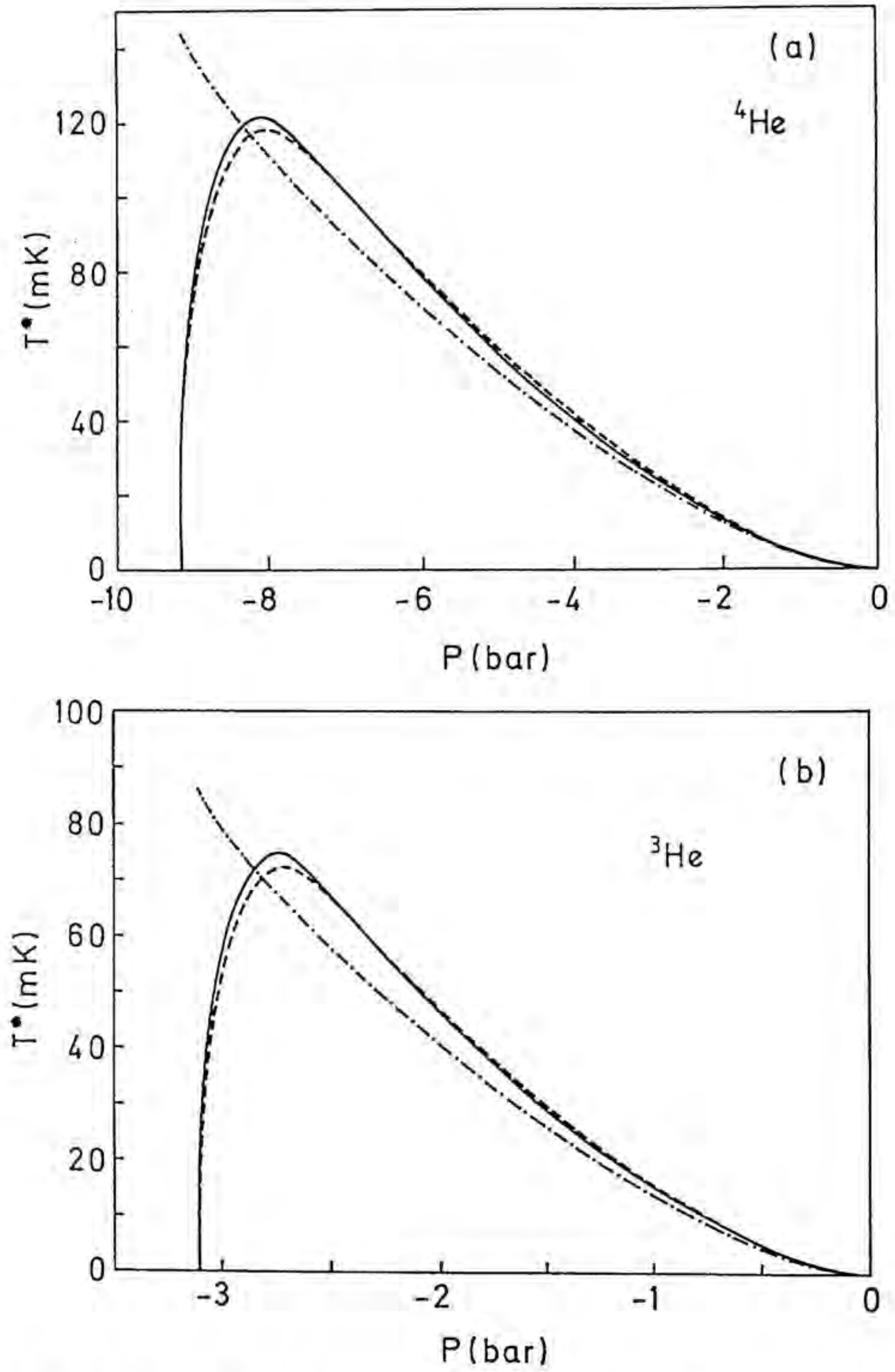

Figure 4.2. (a) T^* (mK) as a function of P (bar) for ^{4}He. (b) Same as (a) for ^{3}He. The solid lines are the results from Eq. (4.29), and the dashed lines are the WKB results (Eq. (4.30)). The dash-dotted lines correspond to the capillarity model, Eq. (4.37).

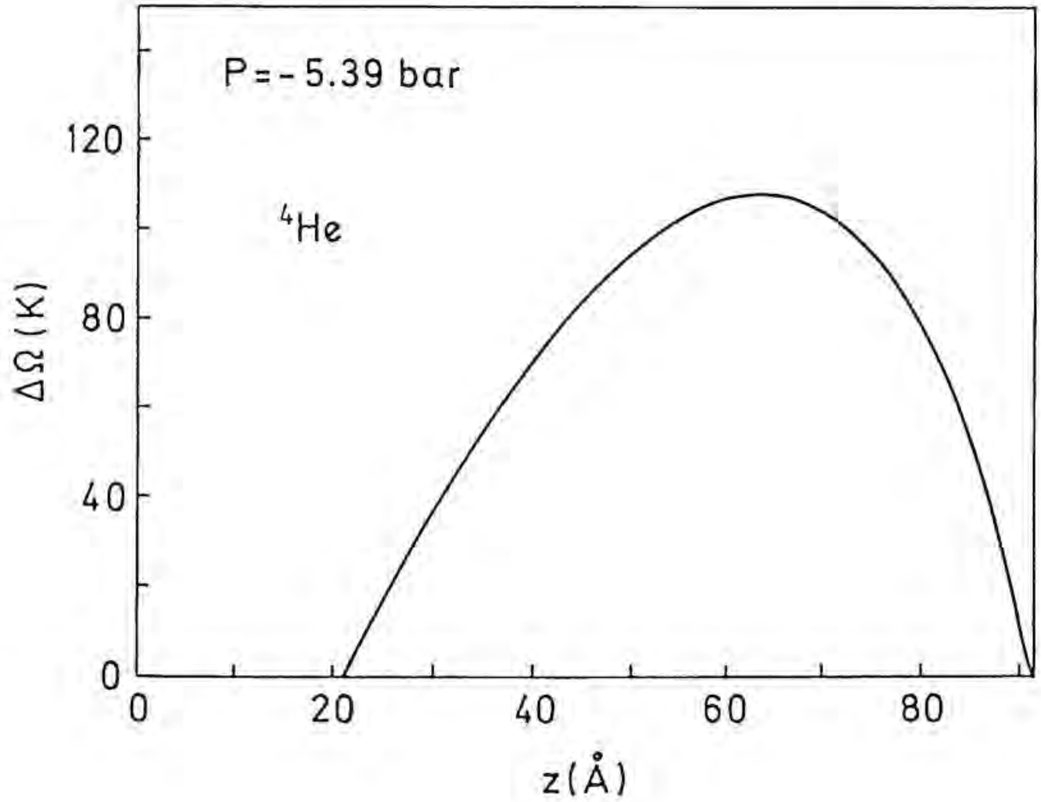

Figure 4.3. $\Delta\Omega$ (K) for ^{4}He at $P = -5.39$ bar as a function of the collective variable z (Å) defined in Eq. (4.31).

for $0 \leq E \leq \Delta\Omega_{max} = b^2/4a$, the turning points are

$$\delta_{1,2} = \frac{b}{2a} \mp \sqrt{\frac{b^2}{4a^2} + \frac{E}{a}} \tag{4.34}$$

and from Eq. (4.25), $S^Q(E) = \pi b^2/(2a)^{3/2}$, which is E-independent, and so is then T^*.

Finally, it is quite instructive to see how T^* can be obtained within the capillarity model, Eqs. (4.3) and (4.4). We have

$$\Delta\Omega(\delta) = 4\pi(R_c + \delta)^2\sigma - \frac{4}{3}\pi(R_c + \delta)^3|P| \tag{4.35}$$

and

$$B(\delta) = \frac{4\pi m}{\hbar^2}(R_c + \delta)^3 \rho_m \,. \tag{4.36}$$

Thus,

$$T^{*\,cap} = \frac{1}{4\pi\sigma}\sqrt{\frac{\hbar^2}{m}\frac{|P|^3}{\rho_m}} \,. \tag{4.37}$$

The WKB result is also analytical:

$$\begin{aligned} T^{*\,cap}_{WKB} &= \sqrt{\frac{2}{3}}\,\frac{512}{405}\,\frac{1}{4\pi\sigma}\sqrt{\frac{\hbar^2}{m}\frac{|P|^3}{\rho_m}} \\ &= 1.03\, T^{*\,cap} . \end{aligned} \tag{4.38}$$

We have represented $T^{*\,cap}$ in Figs. 4.2 (a) and (b) as a dash-dotted line. It can be seen that this model only works near the saturation point where bubbles are large and finite size effects such as curvature, surface diffuseness and partial filling-in of the bubbles, which are automatically incorporated in a density functional approach [8], are less relevant.

It is interesting to realize that S^Q weakly depends on T. This can be understood as follows. For a given $T < T^*$, reminding that $\beta(E) = 1/T(E)$, Eq. (4.23) determines the corresponding E at that T, and the associated $S^Q(E)$ from Eq. (4.25). In actual calculations, we have not proceeded this way. Simply, we have considered Eqs. (4.23) and (4.25) as parametric functions of E with $0 \le E \le \Delta\Omega_{max}$.

4.3 Homogeneous cavitation pressure

Figs. 4.2 (a) and (b) are just telling us that, if the system can be brought down to a negative pressure P, cavitation will proceed by quantum tunneling below $T^*(P)$. The following question now arises: How 'deep' in pressure can the system be dived before bubbles nucleate in an appreciable rate? The corresponding $T^*(P)$ will be in a sense, the 'true' crossover temperature. We now show that at low temperatures, homogeneous cavitation takes place near the spinodal line, where the capillarity model misses T^* by a factor of four.

The homogeneous cavitation pressure P_h, whose magnitude $|P_h|$ is called tensile strength, can be obtained as a function of T equating to unit the product of the transition rate J times the experimental volume V and time t (2.8):

$$1 = (Vt)_e \cdot J \ . \tag{4.39}$$

- For $T \geq T^*$ cavitation proceeds by thermal activation; J is J_T, Eq. (4.26), with the prefactor (2.11)

  $$J_{0T} = \frac{kT}{hV_0} \tag{4.40}$$

  and $V_0 = 4\pi {R_c}^3/3$ represents the volume of the critical bubble. As in the previous chapters, we have taken $R_c = 10$ Å. Two different values of $(Vt)_e$ have been used, 10^{24} Å^3 sec and 2.5×10^{11} Å^3 sec. They are intended to represent two rather different experimental conditions.

- For $T < T^*$ cavitation proceeds by quantum tunneling; J is J_Q, Eq. (4.16). Lacking of a better choice, we have always considered $J_{0Q} = J_{0T}(T = T^*)$.

Figs. 4.4 and 4.5 represent the graphical solution of the following equation which can be obtained from Eq. (4.39):

$$S^Q = \ln\left[J_{0Q} \cdot (Vt)_e\right] \tag{4.41}$$

corresponding to ^{4}He and ^{3}He, respectively, for the two different $(Vt)_e$ values and $T = T^*$. Clearly, the solutions are in the spinodal region where the P-dependence of T^* is steeper. This makes the precise determination of T^* more dependent on the precise value of the product J_{0Q} times $(Vt)_e$ that we would desire, given the present unability to better determine either of them. We thus satisfy ourselves with the upper limit fixed by the maxima of Figs. 4.2 (a) and (b), although values of T^* half these maxima are likely more realistic.

Figs. 4.6 and 4.7 represent P_h (bar) as a function of T (K) for ^{4}He and ^{3}He. The dashed lines correspond to the thermal cavitation regime, and the solid lines, to the quantum one. The horizontal thin lines in the quantum regime are the WKB result. For both isotopes, the upper curves correspond to $(Vt)_e = 10^{24}$ Å^3 sec and the bottom ones to 2.5×10^{11} Å^3 sec. The dots on the pressure axis represent the spinodal pressure. These figures are a 'magnifying glass' look at the spinodal region of the $P_h(T)$ curves shown in Fig. 2.7 of chapter 2. We have thus achieved a complete description of homogeous cavitation in liquid ^{3}He and ^{4}He in the whole temperature range.

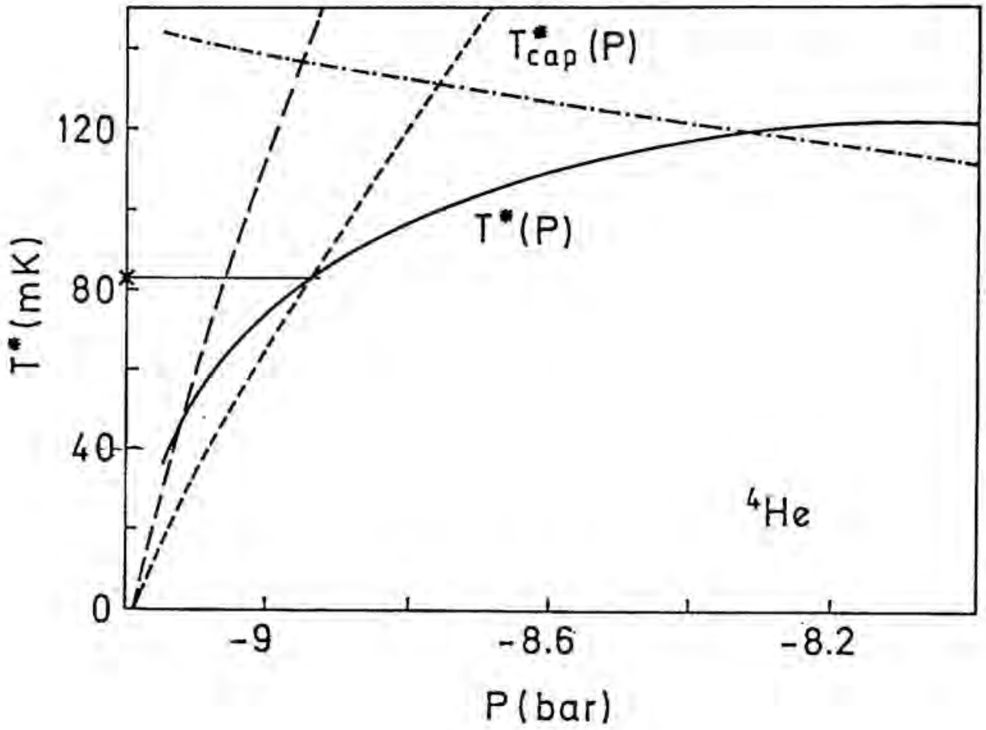

Figure 4.4. Graphical solution of Eq. (4.39) (cross on the y-axis) for ^{4}He. The long-dashed line corresponds to the value $(Vt)_e = 10^{24}$ Å^3 sec, and the short-dashed line, to 2.5×10^{11} Å^3 sec.

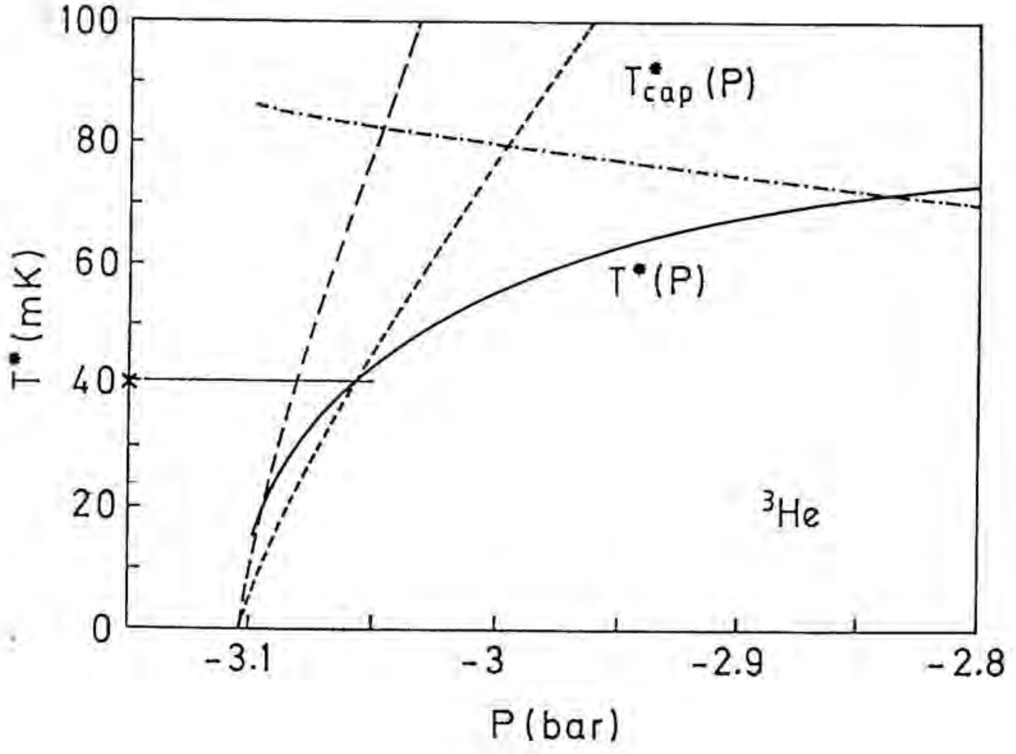

Figure 4.5. Same as Fig. 4.3 for ^{3}He.

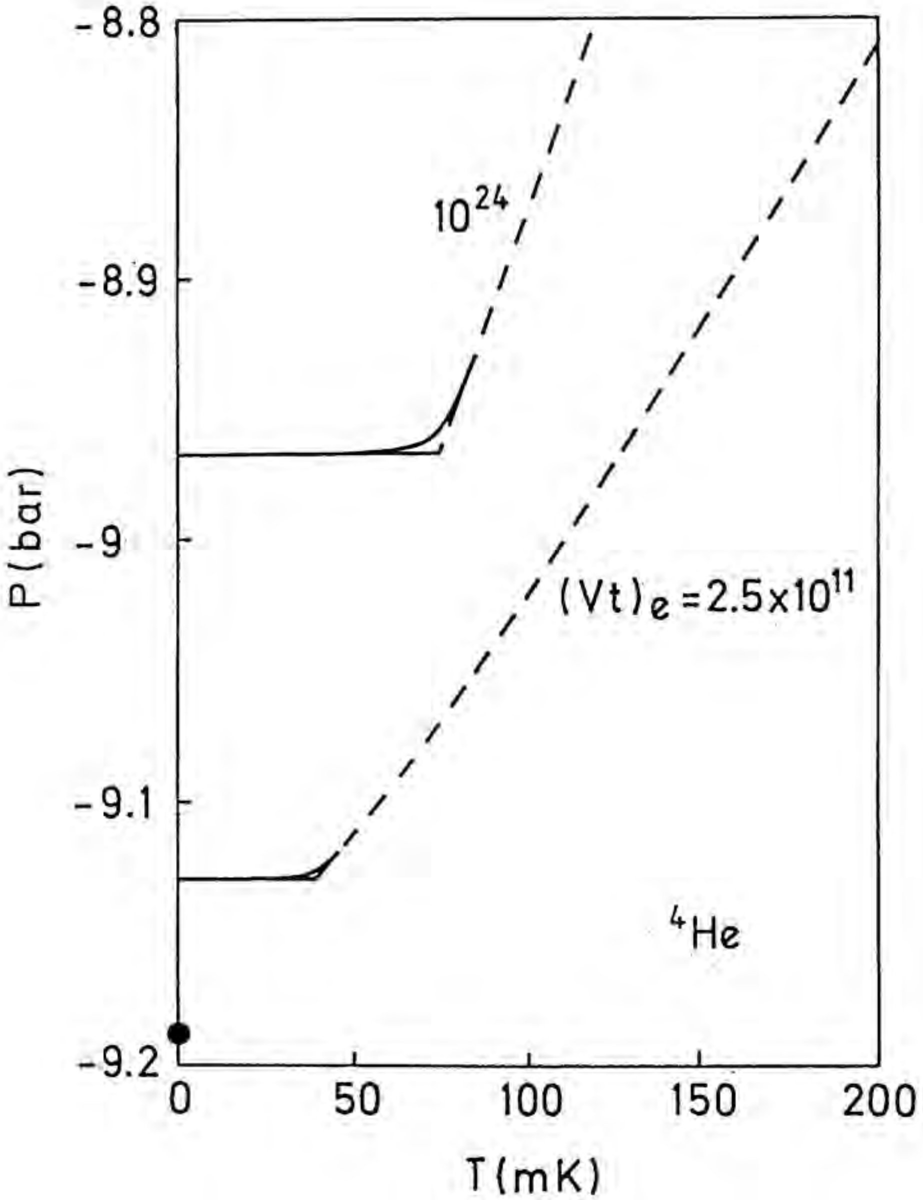

Figure 4.6. Homogeneous cavitation pressure P_h (bar) as a function of T (mK) for ^{4}He. Dashed line, thermal regime. Solid line, quantum regime. The horizontal line corresponds to the T-independent WKB result. The upper curve has been obtained using $(Vt)_e = 10^{24}$ Å^3 sec, and the lower one, 2.5×10^{11}Å^3 sec.

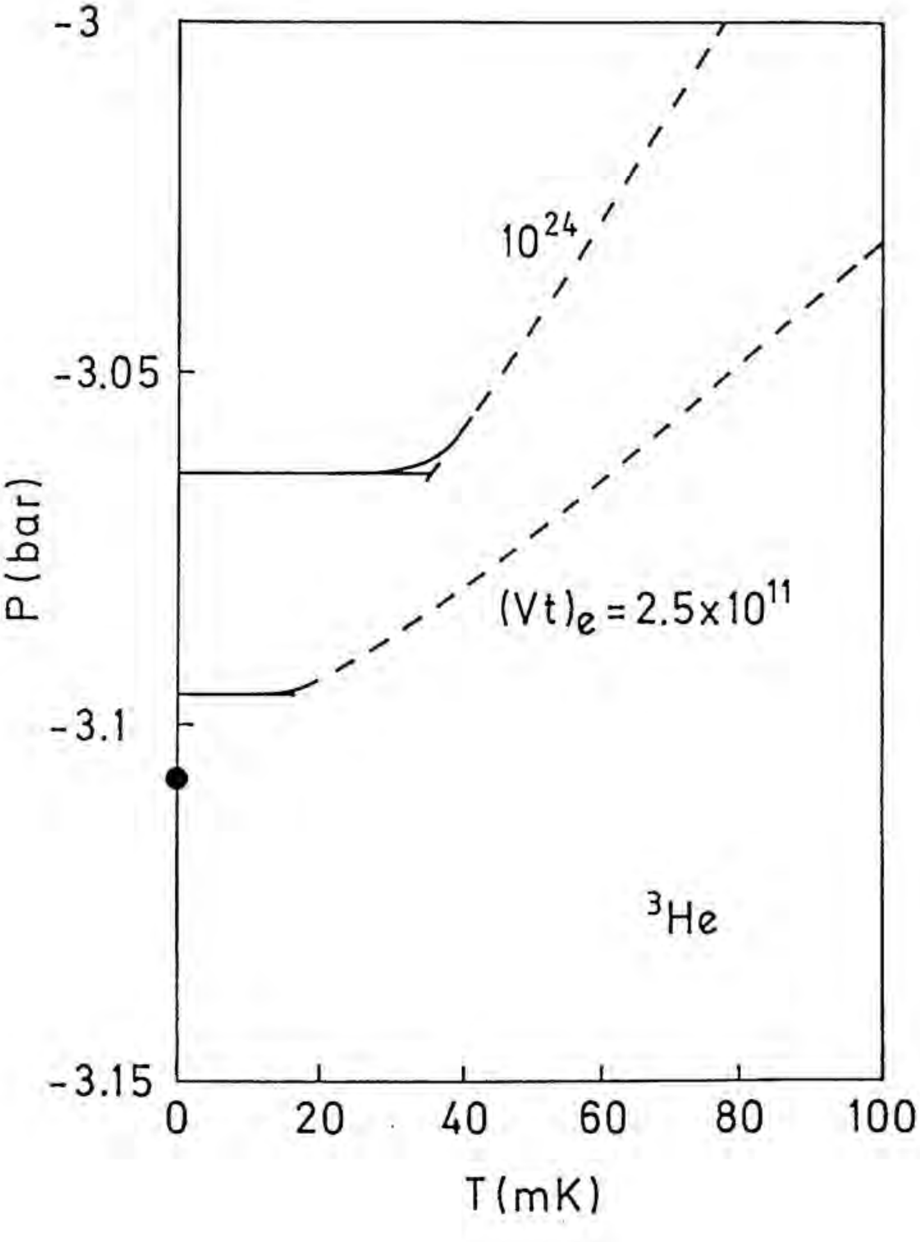

Figure 4.7. Same as Fig. 4.6 for ^{3}He.

Chapter 5

Summary and Conclusions

We have carried out a detailed study of homogeneous nucleation processes taking place in pure ^{3}He and ^{4}He fluids and in ^{3}He-^{4}He liquid mixtures. We have used a density functional approach that overcomes the shortcomings inherent to the capillarity model usually employed in classical nucleation theory. The flexibility of the density functional approach is especially indicated for Helium mixtures, where the limited miscibility of both isotopes at low temperatures and the existence of surface Andreev states make the shape of the nucleation clusters hard to guess and mimic by means of simple sharp-surface models.

We have started studying first thermal activation in pure ^{3}He and ^{4}He (chapter 2) and next in liquid mixtures (chapter 3). In chapter 4 we have completed the study of cavitation in pure isotopes considering quantum tunneling. Thus, our cavitation results for ^{3}He and ^{4}He cover the whole temperature range from the critical down to zero temperature. The results for the mixture only cover the thermal regime.

• Concerning nucleation in pure ^{3}He and ^{4}He, we have shown that at positive pressures, the homogeneous nucleation theory is able to well reproduce the experimental findings. At negative pressures the situation is unsettled, and the experimental tensile strength for ^{4}He [16] seems to be much smaller than that obtained from the theory. At negative pressures, the Classical Nucleation Theory (capillarity model) fails at low temperatures where it predicts homogeneous cavitation pressures (P_h) below the spinodal one. Since the liquid is absolutely unstable below this pressure, it is unphysical.

Using a density functional including thermal effects, we have improved the tensile strengths obtained in previous calculations [16] where the energy barrier was calculated using a temperature independent density functional scheme, and so the result for the barrier was independent of T. We have obtained a tensile strength which is about 20% lower than previous predictions [16] at T_λ, but only 5% reduced at 1.5 K, still above the experimental results.

As a possible way to get rid of these difficulties, cavitation on quantized vortices has been invoked. Even if the liquid is free of ions and solid impurities it may still contain quantized vortices. The influence of vortices on cavitation in pure ^{4}He at negative pressures has been studied in detail by Maris [66]. Althought the introduction of vortices lowers the tensile strength, the effect is much too small to explain the low tensile strengths obtained experimentally in superfluid helium. The disagreement still persists and therefore, other possibilities have to be considered, for example, heterogeneous nucleation associated with electron bubbles [67], both in the bulk and trapped on vortices.

Pettersen et al. [68] have recently performed new experiments on cavitation in liquid ^{4}He at negative pressures, using an apparatus similar to those used by Nissen et al. [15] and Xiong et al. [16]. They provide information about the cavitation process and stress the difficulty to make an accurate determination of the pressure at the focus in this kind of experiments with ultrasonic waves. Consequently, they do not present the results in terms of the focus pressure but voltage applied, making it impossible the comparison with theoretical calculations (which are in terms of P and T at the focus). In view of their experimental measurements they suggest that rather than homogeneous nucleation, heterogeneous nucleation may be occurring on quantized vortices.

• Our calculations on nucleation by quantum tunneling (QT) (chapter 4) and those of [58] rule out any possible expectation that quantum cavitation could help reconcile theory with experiment: we have found crossover temperatures T^* around $\sim$ 120 mK for ^{4}He and $\sim$ 75 mK for ^{3}He. Since thermal fluctuations dominate over quantum tunneling for temperatures larger than T^* we are led to conclude that the available experiments have been carried out in the thermal regime.

It is worth it to mention that the density functional approach has naturally lend itself to the study of quantum cavitation, as chapter 4 and Ref. [58] show. These works yield crossover temperatures that in spite of the differences arising from the use of different functionals and practical details inherent to the methods, are fairly compatible. One of the merits of our method as compared to that of [58], is that T^* is obtained by means of a simple expression that may have as basic limitations, the reliability of the density functional used to describe the system, and the ansatz of rigid transportation of the critical bubble density profile, employed to represent the dynamical evolution of the bubble. We are rather confident on both issues. On one hand, the density functionals we have used have been devised to reproduce many experimental data, in particular the equation of state and surface tension of liquid helium. Moreover, in the available ^{4}He case [23], the spinodal point compare well with that obtained from fully microscopic calculations*. On the other hand, the assumption of rigid transportation, which actually only comes in the calculations for small values of the δ parameter, is justified by the very high incompressibility of these quantum liquids.

The method also gives a quantum barrier penetrability which depends on T, allowing for a smooth connexion between thermal and quantum regimes. It is worth noting that it could be used for other systems accepting a density functional description.

- The extension of thermal cavitation in liquid ^{3}He and ^{4}He to the case of mixtures has led to a rather detailed study of their surface properties. Due to the lowering of the surface tension with increasing ^{3}He concentration, cavitation is more likely to occur, and even for a concentration as small as 10^{-4}%, which is close to that of commercial helium, the pressure of thermal homogeneous cavitation is increased by about 1 bar with respect to that of pure ^{4}He. We have also found that the homogeneous cavitation pressure differs from the spinodal pressure far more in the mixture than in the pure system. These effects are due to the presence of ^{3}He surface states, which also favour the formation of vortices in the mixture, as may be seen by analyzing the influence of surface tension on the energetics of a vortex using the simple hollow core model [69].

We have quantitatively shown the influence of even low ^{3}He concentrations on the cavitation tensile strength, and studied the bubble-to-drop nucleation transition at concentrations above saturation. The experimental knowledge of cavitation in liquid helium is rather scarce, even in the best studied case of pure ^{4}He, and as we have

---

*The density functional result for the spinodal pressure is $P = -9.08$ atm at $\rho = 0.0159$ Å^{-3} as compared with that of Ref. [23], $P = -9.30\pm$ 0.15 atm at $\rho = 0.0158 \pm 0.0001$ Å^{-3}.

commented above, it is still a subject of debate.

We have shown that a plausible way to explain the small degree of supersaturation found in ^{3}He-^{4}He liquid mixtures, is to consider the destabilization of vortex lines filled with ^{3}He. A precise evaluation of Δx_{cr} is a very demanding task, involving a detailed calculation of the structure of these vortices for $x \geq 6.6\%$ and different pressures. Moreover, it is worth to mention that in order to describe vortex structure, any density functional has to be galilean invariant, and none of the current density functionals for ^{3}He-^{4}He mixtures fulfills this requirement.

As in pure ^{3}He and ^{4}He cavitation processes, below a certain temperature T^* nucleation in ^{3}He-^{4}He mixtures proceeds via quantum tunneling. The crossover temperature T^* where thermal and quantum tunneling nucleation compete has not been reliably estimated so far. In their classic paper, Lifshitz and Kagan [26] derived two limiting formulas to study QT based on the same approximations that have led to an estimate of the barrier heights near the saturation and near the spinodal in Sect 3.4. Thus, neither of them unfortunately apply here.

Experimentally, the situation seems to be clearer for the case of ^{3}He drop formation in supersaturated mixtures, for which Satoh et al. [35] have determined that $T^* \simeq 10$mK. An experimental determination of T^* for cavitation would render our calculations complete in the whole range of temperatures from 200mK down to 3mK, since below T^* the pressure of homogeneous cavitation is nearly constant for a given $x-$value. More precise measurements of the surface tension associated with the saturated liquid ^{3}He-mixture interface at $T \sim 0$K would allow one to better estimate the value of the functional parameters.

Very recently, Burmistrov et al. [41] have developed a formalism for QT which takes into account dissipation and superfluidity, and have applied it to describe nucleation of ^{3}He drops in a supersaturated mixture to obtain the demixing curve. However, they make use of the capillarity approximation.

In this thesis we have shown that the density functional approach provides a reliable framework to study both thermal and quantum nucleation in liquid helium. It provides results which are in agreement with the experimental results, except in the case of cavitation in ^{4}He where the experimental situation is still unsettled. In the near future, we plan to address the following questions:

- To consider heterogeneous nucleation in ^{4}He at negative pressures associated with electron bubbles, both in the bulk and trapped on vortices. These processes may lower the tensile strength, hence improving the agreement with experimental data.

- To construct a galilean invariant functional for the mixture with a kinetic term accounting for the superfluid-velocity field around the vortex line. It would provide a more reliable description of vortices in the mixture, and thus one would better determine the critical ^{3}He concentration at which a ^{3}He filled vortex destabilizes.
- To study quantum tunneling cavitation in ^{3}He-^{4}He mixtures by a generalization of the method developed in chapter 4, and determine the quantum-to-thermal crossover temperature.

Bibliography

[1] R.A. Aziz, V.P.S. Nain, J.S. Carley, W.L. Taylor and G.T. McConville, J. Chem. Phys. **70**, 4330 (1979).

[2] R.A. Aziz, F.R.W. Court and C.C.K. Wong, Mol. Phys. **61**, 1487 (1987).

[3] P. Hohenberg and W. Kohn, Phys. Rev. B **136**, 864 (1964).

[4] S. Stringari, Phys. Lett. A **107**, 36 (1985).

[5] J. Dupont-Roc, M. Himbert, N. Pavloff and J. Treiner, J. Low Temp. Phys. **81**, 31 (1990).

[6] M. Barranco, D.M. Jezek, E.S. Hernández, J. Navarro and Ll. Serra, Z. Phys. D **28**, 257 (1993).

[7] F. Dalfovo, A. Lastri, L. Pricaupenko, S. Stringari and J. Treiner, Phys. Rev. B **52**, July (1995).

[8] D.W. Oxtoby, J. Phys.: Condens. Matter **4**, 7627 (1992).

[9] D.W. Oxtoby and R. Evans, J. Chem. Phys. **89**, 7521 (1988).

[10] D.W. Oxtoby, in *Fundaments of Inhomogeneous Fluids*, edited by D. Henderson (Marcel Dekker, New York, 1992), Ch. 10, page 407.

[11] A. Dillmann and G.E.A. Meier, J. Chem. Phys. **94**, 3872 (1991).

[12] Q. Xiong and H.J. Maris, J. Low Temp. Phys. **77**, 347 (1989).

[13] M. Guilleumas, M. Pi, M. Barranco, J. Navarro and M.A. Solís, Phys. Rev. B **47**, 9116 (1993).

[14] X.C. Zeng and D.W. Oxtoby, J. Chem. Phys. **94**, 4472 (1991).

[15] J.A. Nissen, E. Bodegom, L.C. Brodie and J.S. Semura, Phys. Rev. B **40**, 6617 (1989).

[16] Q. Xiong and H.J. Maris, J. Low Temp. Phys. **82**, 105 (1991).

[17] M. Barranco, M. Pi, A. Polls and X. Viñas, J. Low Temp. Phys. **80**, 77 (1990).

[18] A. Guirao, M. Centelles, M. Barranco, M. Pi, A. Polls and X. Viñas, J. Phys.: Condens. Matter **4**, 667 (1992).

[19] H.J. Maris and Q. Xiong, Phys. Rev. Lett **63**, 1078 (1989).

[20] H.J. Maris, Phys. Rev. Lett. **66**, 45 (1991).

[21] M.A. Solís and J. Navarro, Phys. Rev. **B45**, 13080 (1992).

[22] *Homogeneous nucleation theory*, Advances in Theoretical Chemistry, F.F. Abraham, Ed. by H. Eyring and D. Henderson (Academic Press, New York and London, 1974).

[23] J. Boronat, J. Casulleras and J. Navarro, Phys. Rev. **B50**, 3427 (1994).

[24] D.N. Sinha, J.S. Semura and L.C. Brodie, Phys. Rev. A **26**, 1048 (1982).

[25] D. Lezak, L.C. Brodie, J.S. Semura and E. Bodegom, Phys. Rev. B **37**, 150 (1988).

[26] I.M. Lifshitz and Yu. Kagan, Zh. Eksp. Teor. Fiz. **62**, 385 (1972) (Sov. Phys. JETP **35**, 206 (1972)).

[27] D.M. Jezek, M. Guilleumas, M. Pi, M. Barranco, and J. Navarro, Phys. Rev. B **48**, 16582 (1993).

[28] R.K. Pathria, *Statistical Mechanics* (Pergamon, Oxford, 1972).

[29] V.A. Akulichev and V.A. Bulanov, Akust. Zh. **20**, 817 (1974) (Sov. Phys. Acoust. **20**, 501 (1975)).

[30] K. Binder, in *Material Science and Technology*, Vol 5, Eds. R.W. Cahn, P. Haasen and E.J. Kramer (VCH, Weinheim, 1991).

[31] X.C. Zeng and D.W. Oxtoby, J. Chem. Phys. **95**, 5940 (1991).

[32] A.F. Andreev, Zh. Eksp. Teor. Fiz. **50**, 1415 (1966) (Sov. Phys. JETP **23**, 939 (1966)).

[33] F. Dalfovo and S. Stringari, Phys. Lett. A **112**, 171 (1985).

[34] F. Dalfovo, Ph. D. thesis, University of Trento (1989), unpublished.

[35] T. Satoh, M. Morishita, M. Ogata, and S. Katoh, Phys. Rev. Lett. **69**, 335 (1992).

[36] M. Guilleumas, D.M. Jezek, M. Pi, M. Barranco, and J. Navarro, Phys. Rev. B **51**, 1140 (1995).

[37] M. Guilleumas, M. Pi, M. Barranco, D.M. Jezek, and J. Navarro, Phys. Rev. B **52**, to appear (1995).

[38] D.M. Jezek, M. Guilleumas, M. Pi, and M. Barranco, Phys. Rev. B **51**, 11981 (1995).

[39] L. Landau and E. Lifshitz, *Física Estadística* (Ed. Reverté, Barcelona, 1969).

[40] V.A. Mikheev, E.Ya. Rudavskii, V.K. Chagove and G.A. Sheshin, Fiz. Nizk. Temp. (USSR) **17**, 444 (1991).

[41] S.N. Burmistrov, L.B. Dubovskii, and V.L. Tsymbalenko, J. Low Temp. Phys. **90**, 363 (1993).

[42] C. Ebner and D.O. Edwards, Phys. Rep. **2**, 77 (1970).

[43] E. Krotscheck and M. Saarela, Phys. Rep. **232**, 1 (1993).

[44] J. Boronat, Ph. D. thesis, University of Barcelona (1991), unpublished.

[45] M. Iino, M. Suzuki and A.J. Ikushima, J. Low Temp. Phys. **61**, 155 (1985).

[46] H.M. Guo, D.O. Edwards, R.E. Sarwinski, and J.T. Tough, Phys. Rev. Lett. **27**, 1259 (1971).

[47] D.O. Edwards and W.F. Saam, in *Progress in Low Temperature Physics*, D.F. Brewer ed. (North Holland, 1978) Vol. VII A, page 283.

[48] N. Pavloff and J. Treiner, J. Low. Temp. Phys. **83**, 15 (1991).

[49] J. Landau, J.T. Tough, N.R. Brubaker, and D.O. Edwards, Phys. Rev. Lett. **23**, 283 (1969).

[50] D.O. Edwards, S.Y. Shen, J.R. Eckardt, P.P. Fatouros, and F.M. Gasparini, Phys. Rev. B **12**, 892 (1975).

[51] I.M. Lifshitz, V.N. Polesskii, and V.I. Khokhlor, Zh. Eksp. Teor. Fiz. **74**, 268 (1978) (Sov. Phys. JETP **47**, 137 (1978)).

[52] K. Nishioka and I. Kusaka, J. Chem. Phys. **96**, 5370 (1992).

[53] J.W. Cahn and J.E. Hilliard, J. Chem. Phys. **28**, 258 (1958).

[54] J.W. Cahn and J.E. Hilliard, J. Chem. Phys. **31**, 688 (1959).

[55] P. Seligmann, D.O. Edwards, R.E. Sarwinski and J.T. Tough, Phys. Rev. **181**, 415 (1969).

[56] R.J. Donnelly, *Quantized Vortices in Helium II*, Cambridge Studies in Low Temperature Physics (Cambridge University Press, Cambridge, 1991).

[57] F. Dalfovo, Phys. Rev. B **46**, 5482 (1992).

[58] H.J. Maris, J. Low Temp. Phys. **98**, 403 (1995).

[59] M. Guilleumas, F. Garcias, M. Barranco, M. Pi and E. Suraud, Z. Phys. D**25**, 227 (1993).

[60] S. Stringari and J. Treiner, Phys. Rev. B **36**, 8369 (1987).

[61] A. Galindo and P. Pascual, *Quantum Mechanics* (Springer-Verlag, Berlin, 1990).

[62] S. Coleman, Phys. Rev. D **15**, 2929 (1977).

[63] C.G. Callan, and S. Coleman, Phys. Rev. D **16**, 1762 (1977).

[64] H. Kleinert, *Path Integrals in Quantum Mechanics Statistics and Polymer Physics* (World Scientific, Singapore, 1990).

[65] A.H. Blin, B. Hiller, H. Reinhardt, and P. Schuck. Nucl. Phys. A **484**, 295 (1988).

[66] H.J. Maris, J. Low Temp. **94**, 125 (1994).

[67] V.A. Akulichev, Ultrasonics **26**, 8 (1986).

[68] M.S. Pettersen, S. Balibar and H.J. Maris, Phys. Rev. B **49**, 12062 (1994).

[69] F. Dalfovo, G. Renversez and J. Treiner, L. Low Temp. Phys. **89**, 425 (1992).